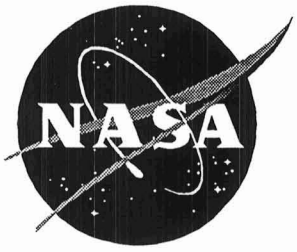

NASA Conference Publication 3306

NASA-CP-3306 19960009448

Computational Modeling of Tires

Compiled by
Ahmed K. Noor and John A. Tanner

Proceedings of a workshop sponsored by the National Aeronautics and Space Administration, Washington, D.C., and the University of Virginia Center for Computational Structures Technology, Hampton, Virginia, and held at Virginia Consortium of Engineering and Science Universities, Hampton, Virginia
October 26–27, 1994

August 1995

NASA Conference Publication 3306

Computational Modeling of Tires

Compiled by
Ahmed K. Noor
University of Virginia Center for Computational Structures Technology • Hampton, Virginia

John A. Tanner
Langley Research Center • Hampton, Virginia

Proceedings of a workshop sponsored by the National Aeronautics and Space Administration, Washington, D.C., and the University of Virginia Center for Computational Structures Technology, Hampton, Virginia, and held at Virginia Consortium of Engineering and Science Universities, Hampton, Virginia
October 26–27, 1994

National Aeronautics and Space Administration
Langley Research Center • Hampton, Virginia 23681-0001

August 1995

This publication is available from the following sources:

NASA Center for AeroSpace Information
800 Elkridge Landing Road
Linthicum Heights, MD 21090-2934
(301) 621-0390

National Technical Information Service (NTIS)
5285 Port Royal Road
Springfield, VA 22161-2171
(703) 487-4650

PREFACE

This document contains the proceedings of the Workshop on Computational Modeling of Tires held at the Peninsula Graduate Center of the Virginia Consortium of Engineering and Science Universities, October 26-27, 1994. The workshop was jointly sponsored by the University of Virginia Center for Computational Structures Technology and NASA. Workshop attendees came from government agencies, tire industry, commercial software companies, and universities. The objectives of the workshop were to assess the state-of-technology in computational modeling of tires and to provide guidelines for focused future research leading to an enhanced capability for the numerical simulation of tire response.

Certain materials and products are identified in this publication in order to specify adequately the materials and products that were investigated in the research effort. In no case does such identification imply recommendation or endorsement of products by NASA, nor does it imply that the materials and products are the only ones or the best ones available for this purpose. In many cases equivalent materials and products are available and would probably produce equivalent results.

Ahmed K. Noor
Center for Computational Structures Technology
University of Virginia
Hampton, VA

John A. Tanner
NASA Langley Research Center
Hampton, VA

CONTENTS

Attendees

Dr. Ashraf Ali
ANSYS, Inc.
P.O. Box 65
Houston, PA 15342
(412) 746-3304; Fax (412) 746-9494

Mr. Robert Benedict
Goodyear Tire and Rubber Company
Goodyear Technical Center
Akron, OH 44309-3531
(216) 796-4076; Fax (216) 796-3947

Dr. Thomas R. Branca
Daedalus Associates, Inc.
426 Boxford Road
Bradford, MA 01835
(508) 521-2100; Fax is the same no.

Dr. W. Scott Burton
Mail Stop 369
University of Virginia
NASA Langley Research Center
Hampton, VA 23681
(804) 864-1992; Fax (804) 864-7943

Dr. Mangal Chawla
U.S. Air Force
WL/FIVMA
1981 Fifth Street
WPAFB, OH 45433-7202
(513) 255-2663; Fax (513) 258-0180

Dr. Gene Chen
General Tire, Inc.
One General Street
Akron, OH 44329
(216) 798-3377; Fax (216) 798-3374

Dr. David Chestnutt
Virginia Consortium of Engineering
and Science Universities
303 Butler Farm Road
Hampton, VA 23666
(804) 766-8036; Fax (804) 865-0278

Mr. Sam K. Clark
Precision Measurement Company
P.O. Box 7676
Ann Arbor, MI 48107
(313) 995-0041; Fax is the same no.

Ms. Noreen Cmar
Mail Stop 231
NASA Langley Research Center
Hampton, VA 23681
(804) 864-8475; Fax (804) 864-4914

Dr. Thomas P. Cully
The MacNeal-Schwendler Corp.
1000 Howard Blvd., Suite 105
Mount Laurel, NJ 08054
(609) 778-3733; Fax (609) 778-9609

Dr. Kent T. Danielson
University of Virginia
Mail Stop 369
NASA Langley Research Center
Hampton, VA 23681
(804) 864-8668; (804) 864-8089

Ms. Pamela A. Davis
Mail Stop 497
NASA Langley Research Center
Hampton, VA 23681
(804) 864-1307; Fax (804) 864-8090

Mr. Fabrice De Biasi
Michelin Aircraft Tire Corporation
9700 Research Drive
Charlotte, NC 28282
(704) 548-2521; Fax (704) 548-2599

Mr. Gregory L. Felder
Director of Product Engineering
Michelin Aircraft Tire Corporation
9700 Research Drive
Charlotte, NC 28262-8511
(704) 548-2442; Fax (704) 548-2508

Mr. Danny R. Hoad
Mail Stop 266
NASA Langley Research Center
Hampton, VA 23681
(804) 864-5060; Fax (804) 864-3970

Mr. W. Edward Howell
Mail Stop 497
NASA Langley Research Center
Hampton, VA 23681
(804) 864-1299; Fax (804) 864-8090

Dr. Arthur R. Johnson
Mail Stop 240
NASA Langley Research Center
Hampton, VA 23681
(804) 864-1310

Dr. Levent Karaoglan
Mail Stop 369
University of Virginia
NASA Langley Research Center
Hampton, VA 23681
(804) 864-8518; Fax (804) 864-8089

Dr. Makarand Kulkarni
University of Virginia
Mail Stop 369
NASA Langley Research Center
Hampton, VA 23681
(804) 864-8517; Fax (804) 864-8089

Ms. Megan Lay
Dept. 354, MC-1069020
McDonnell Aircraft Company
P.O. Box 516
St. Louis, MO 63166-0516
(314) 232-8766; Fax (314) 232-4141

Dr. John G. Lightner
Bridgestone/Firestone Tire Company
1200 Firestone Parkway
Akron, OH 44317
(216) 379-6250; Fax (216) 379-3961

Dr. John R. Luchini
Cooper Tire Company
701 Lyma Avenue
Findlay, OH 45840
(419) 424-4313; Fax (419) 424-4305

Ms. Angela J. Mason
Mail Stop 497
NASA Langley Research Center
Hampton, VA 23681
(804) 864-5111; Fax (804) 864-8090

Ms. Joey Meade
Materials Directorate
Army Research Laboratory
Watertown, MA 02172-0001
(617) 923-5130; Fax (617) 923-5154

Mr. John P. Medzorian
WL/FIVMA
Wright Patterson AFB, OH 45433
(513) 255-2663; Fax (513) 258-0180

Dr. John C. Muskivitch
The MacNeal-Schwendler Corporation
120 Independence Drive
Menlo Park, CA 94025
(415) 617-9761; Fax (415) 617-9765

Dr. Ahmed K. Noor
University of Virginia
Mail Stop 369
NASA Langley Research Center
Hampton, VA 23681
(804) 864-1978; Fax (804) 864-8089

Dr. Joseph Padovan
Department of Mechanical Engineering
University of Akron
Akron, OH 44325-3903
(216) 972-7731; Fax (216) 972-6027

Dr. Gerry D. Pollock
Mail Stop 369
University of Virginia
NASA Langley Research Center
Hampton, VA 23681
(804) 864-2888; Fax (804) 864-8089

Ms. Claudia J. Quigley
Materials Directorate
Army Research Laboratory
Watertown, MA 02172-0001
(617) 923-5152; Fax (617) 923-5154

Dr. Raouf Ridha
Goodyear Technical Center
P.O. Box 3531
Akron, OH 44309-3531
(216) 796-2566; Fax (216) 796-8752

Dr. Peter Szewczyk
Mail Stop 369
University of Virginia
NASA Langley Research Center
Hampton, VA 23681
(804) 864-1991; Fax (804) 864-8089

Dr. John A. Tanner
Mail Stop 497
NASA Langley Research Center
Hampton, VA 23681
(804) 864-1305; Fax (804) 864-8090

Dr. John T. Tielking
Mechanics and Materials Center
Civil Engineering Department
Texas A&M University
College Station, TX 77843-3136
(409) 845-2467; Fax (409) 845-6156

Mr. Michael Trinko
Goodyear Tire and Rubber Company
Technical Center, Dept. 431A
P.O. Box 3531
Akron, OH 44309-3531
(216) 796-1722; Fax (216) 796-8835

Dr. Jan Walczak
ADINA R&D, Inc.
71 Elton Avenue
Watertown, MA 02172
(617) 926-5199; Fax (617) 926-0238

Dr. Kang Ming Xu
Mail Stop 369
University of Virginia
NASA Langley Research Center
Hampton, VA 23681
(804) 864-9195; Fax (804) 864-8089

Mr. Thomas J. Yager
Mail Stop 497
NASA Langley Research Center
Hampton, VA 23681
(804) 864-1304; Fax (804) 864-8090

INTRODUCTION

A significant capability has been developed over the past two decades for the computational modeling and analysis of tires. Several in-house and commercial software systems are currently available for accurate determination of static load deflection characteristics, contact area shape, free vibration modes, and quasi-static rolling resistance. This success can be attributed, in part, to the joint NASA/U.S. tire industry National Tire Modeling Program (NTMP). This program was initiated in 1983 and was completed in 1991. At its peak seven U.S. tire companies, four universities, and a software developer participated in the program. The NTMP established a set of benchmark tire modeling problems, developed a national database of experimental tire measurements, and led to the development of a number of tire modeling strategies and solution algorithms that could be incorporated into new or existing software packages.

Despite the significant advances made in the computational modeling and analysis of tires, a number of technology needs and related tasks must be addressed by the research community to enhance the state-of-the-art in computational modeling of tires and to make it an effective tool in tire design. The joint University of Virginia/NASA workshop held at the Peninsula Graduate Center of the Virginia Consortium of Engineering and Science Universities, October 26-27, 1994 focused on the status of computational modeling of tires and the current and future needs for further development of this technology. The list of pacing items given in this introduction was compiled from a number of participants.

COMPUTATIONAL NEEDS

The technology needs identified by the participants can be grouped into the following five major headings: 1) material characterization of filled rubber and heat generation mechanisms; 2) understanding the physical phenomena associated with frictional contact, wear and noise generation; 3) accurate determination of tire footprint shape, size and pressure distribution; 4) prediction of wear resistance, failure and fatigue; and 5) tire/vehicle interaction and its effect on riding and handling qualities and performance.

For each of the aforementioned items, attempts should be made to exploit the major characteristics of high-performance computing technologies, as well as the future computing environment. The five primary technology needs and related tasks are described subsequently.

1. Material characterization of cord and filled rubber and heat generation mechanisms. The reliability of the predictions of the tire response, damage and failure is critically dependent on the accurate characterization and modeling of the material behavior and heat generation mechanisms under different operational conditions.

2. Understanding the physical phenomena associated with frictional contact, wear and noise generation. This includes understanding the frictional contact between the rubber and road and its effect on handling and braking forces, and mechanisms of wear and abradability of material.

3. Accurate determination of the footprint shape, size and pressure distribution which includes development of simple and fast numerical algorithms for handling continuous contact and modeling the actual tread patterns.

4. Prediction of wear resistance, failure and fatigue. This includes capability for the accurate calculation of contact forces, and predictions of failure/fatigue and wear initiation and propagation based on stress/strain history.

5. Tire/vehicle interaction and its effect on riding quality and handling performance - relating the response characteristics to the tire performance. This requires identifying the key elements in the computational model of the tire and vehicle that are required to capture the major response characteristics.

RELATED TASKS

To accomplish the aforementioned technology needs, some related tasks need to be implemented before computational modeling of tires can have a significant impact on the tire design process. These are: 1) high-fidelity modeling of tire and tread pattern; 2) efficient computational strategies for rolling contact; 3) improved test methods, measuring techniques and scaling laws; and 4) validation of numerical simulations through a number of carefully designed benchmark tests.

Highlights of the Workshop

Ahmed K. Noor
Center for Computational Structures Technology
University of Virginia

OBJECTIVES AND FORMAT OF WORKSHOP

The computational modeling of tire response represents one of the challenging applications of computational structural mechanics and has been the focus of intense efforts in recent years. Despite these efforts, major advances are needed in various areas of the technology before computational modeling can be routinely used in tire design. The objectives of the present workshop are (Fig. 1): to assess the state-of-technology in computational modeling of tires; and to identify current and future needs for further development of the technology.

The workshop includes presentations and two panels. The presentations are included in the proceedings to illuminate some of the diverse issues, and to provide fresh ideas for future research and development.

Objectives

- **Assess the state-of-technology in computational modeling of tires**
- **Identify future directions for research**

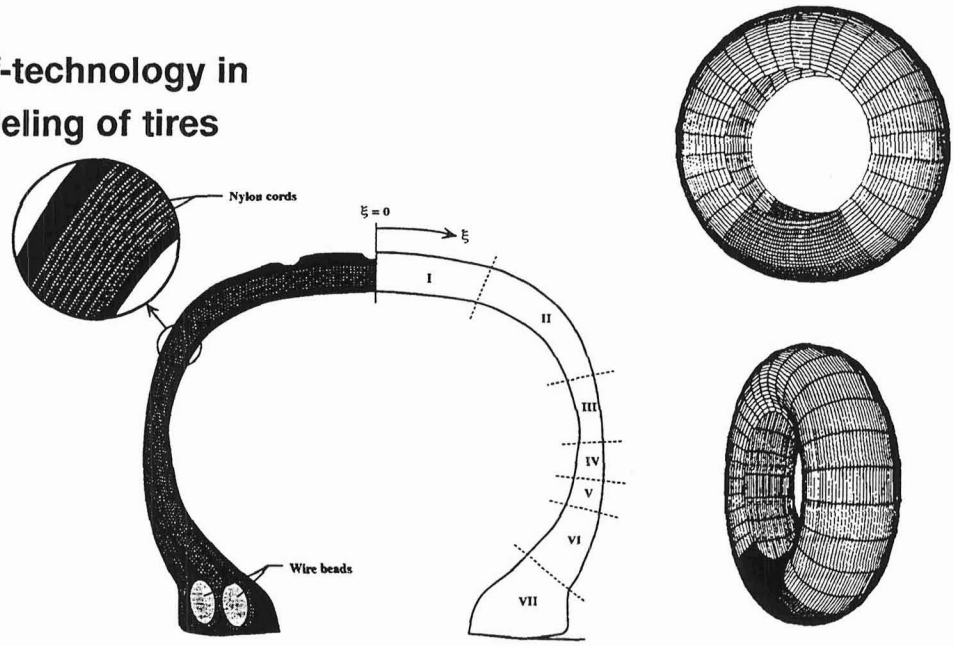

Format

- **Presentations**
- **Panels**
  - **Panel 1 - Computational Needs for Tire Modeling and Design. Moderators: R. Ridha and A. Noor**
  - **Panel 2 - Experimental Needs and Effective Coupling Between Experiments and Numerical Simulations. Moderators : J. Tanner and J. Luchini**
- **Proceedings**

Figure 1

ASSESSMENT OF THE STATE-OF-TECHNOLOGY

The first aspect of assessing the state-of-technology is to assess our understanding of the physical phenomena associated with tire response and durability. Some of the issues that affect these physical phenomena are listed in Fig. 2. These are: characterization of tire materials; footprint definition; noise, damage, wear, aging and failure mechanisms; friction modeling; accurate determination of operational conditions (viz., loads, strains, and temperature).

- **Understanding physical phenomena associated with tire response and durability**
  - **Footprint definition**
  - **Noise, damage, wear, aging and failure mechanisms**
  - **Friction modeling**
  - **Traction on both wet and dry surfaces**
- **Characterization of tire materials**
- **Accurate determination of operational conditions**
  - **Loads and strains**
  - **Temperature**

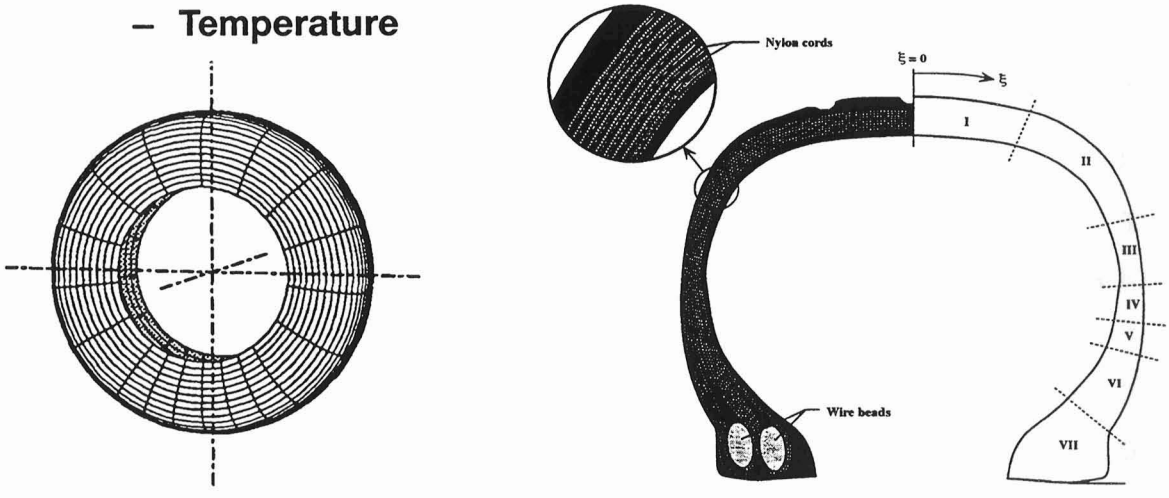

Figure 2

ASSESSMENT OF THE STATE-OF-TECHNOLOGY (Cont'd.)
Current Capabilities

The second aspect of assessment of technology is that of current capabilities for computational modeling of tires (Fig. 3). These capabilities include computational material models ranging from micromechanical models for cord-rubber (flexible) composites and friction models to damage mechanisms, wear and failure models; modeling of the cross-sectional details using three-dimensional, quasi three-dimensional and two-dimensional finite element models; efficiency of currently-used computational strategies for handling frictional contact and rolling tire problem; and assessment of software systems currently used for modeling tire response and failure.

- **Computational Material Models**
  - **Micromechanical modeling for cord-rubber (flexible) composites**
  - **Friction modeling**
  - **Damage mechanisms, wear and failure models**
- **Level of Details**
  - **Three-dimensional and quasi-three-dimensional models**
  - **Two-dimensional shell models**
  - **Other (detailed) models**
- **Efficiency of Computational Strategies**
  - **Frictional contact algorithms**
  - **Rolling tire problem**
- **Current Software Systems: MSC NASTRAN, ABAQUS, ANSYS, ADINA, . . .**

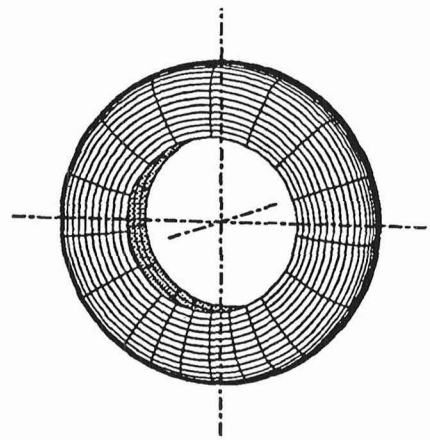

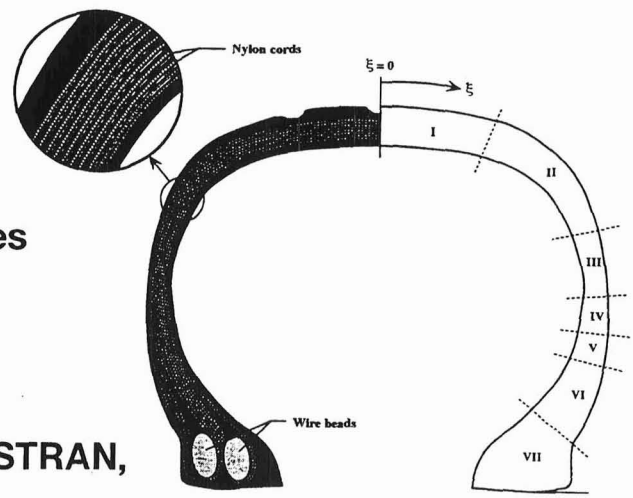

Figure 3

FUTURE DIRECTIONS FOR RESEARCH

Three factors should be taken into account in identifying future directions for research (Fig. 4):

1) Characteristics of future tires and their implications on design requirements;

2) Future computing environment and computing paradigm; and

3) Recent and future developments in other fields of comptuational technology which can be adapted to computational modeling of tires.

Three of the important research tasks are:

1) Validation of numerical simulations and selection of benchmark tests for assessing new computational strategies and numerical algorithms. The standardized tests would provide a measure of confidence in added functional capabilities to existing codes, or in new codes;

2) Treatment of uncertainties in material properties, geometry, loading and operational environment through probabilistic analysis, stochastic modeling and sensitivity analysis; and

3) Understanding the relationship between the various response quantities and key performance measures for the tire (viz., durability and life, tread wear, noise, rolling resistance, vibrations, cornering, riding and handling qualities).

- **Characteristics of future tires and their implications on design requirements.**
- **Validation of numerical simulations and effective coupling with experiments (benchmarks).**
- **Treatment of uncertainties in material properties, geometry, loading and operational environment (probabilistic analysis, stochastic modeling and sensitivity analysis).**
- **Impact of developments in other fields of computational technology (e.g., modeling of rigid composites, virtual manufacturing and IPPD).**
- **Impact of emerging and future computing environment (high-performance computers, multi-media workstations, advanced visualization technology).**

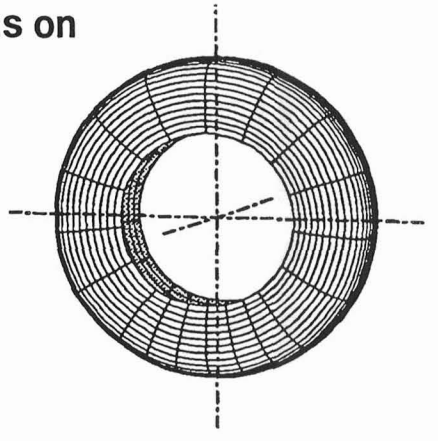

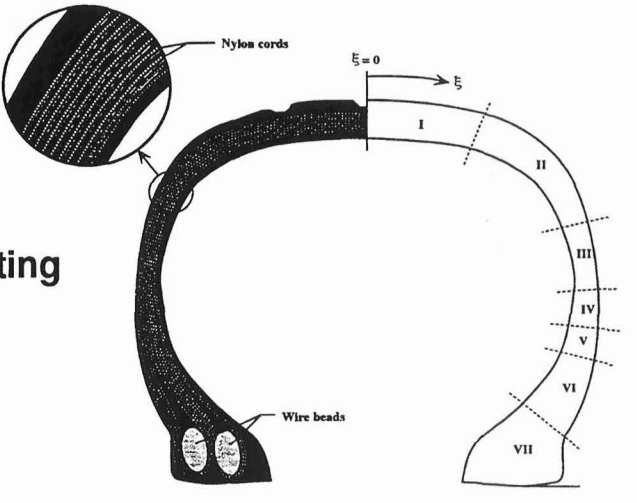

Figure 4

Touchdown Dynamics

Samuel K. Clark
Precision Measurement Company
Ann Arbor, MI

TOUCHDOWN DYNAMICS

Samuel K. Clark
Precision Measurement Co.
Ann Arbor, MI

INTRODUCTION

Aircraft tire wear results from operating conditions are quite different from those encountered in land vehicles. One of the most important of these is touchdown, where the tire suddenly spins up from zero to a large angular velocity. This phenomenon is studied from both the analytical and experimental points of view. The analysis is basic, using elementary properties of the tire and wheel. It results in a new dimensionless description of the process. The experimental study consists primarily of small scale laboratory data, although limited full scale tire data is also presented.

The data show increasing weight loss during touchdown as the dimensionless severity increases.

[1]This work was conducted under USAF Contract F33657-92-C-2167. Mr. Paul Wagner was the USAF project engineer.

WHEEL AND AIRCRAFT PARAMETERS

The analysis assumes that a tire and wheel are attached to the axle of an aircraft moving at forward velocity V_x with constant sink rate V_z, with the wheel at zero angular velocity ω at time t=0 of initial contact. The tire of diameter D is attached to a wheel with brake rotor, all of which have polar moment of inertia I_y. The vertical and horizontal contact forces are F_z and $F_x = \mu F_z$, respectively, where the friction coefficient μ is assumed constant during spin-up.

The tire is assumed to be rigid torsionally, but to be a linear spring in the vertical direction, so that $F_z = K_z \delta_z$ where δ_z is vertical deflection and K_z is the vertical spring rate. The contact area is controlled by tire deflection.

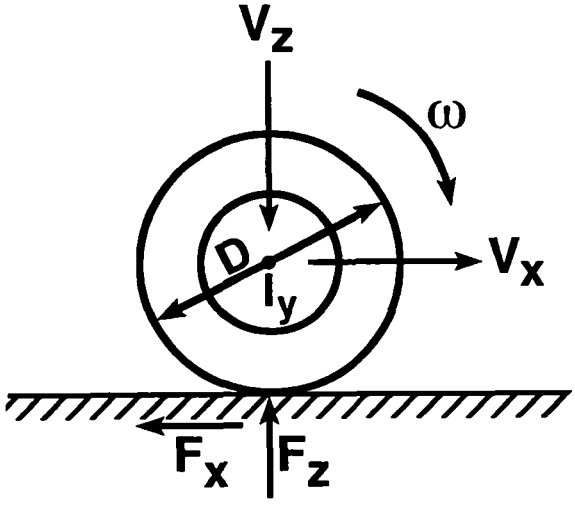

F_x = tire horizontal force
V_x = landing speed, assumed constant
V_z = sink rate, assumed constant
I_y = polar inertia of tire, wheel and brake
K_z = tire vertical spring rate
μ = friction coefficient
ω = tire angular velocity
D = tire diameter
F_z = tire vertical force

Figure 1 - Wheel and tire parameters.

TOUCHDOWN ANALYSIS

The analysis is based on evaluating the integral of contact area times sliding distance as a measure of the volume of tread material lost by abrasion and/or ablation.

Assuming the volume of a tire is approximately proportional to the square of the diameter and the first power of the tire width, the resulting dimensionless loss of volume during touchdown is given in Fig. 2. This new parameter is called Touchdown Severity and is postulated to be a dimensionless measure of volume lost, as shown in Fig. 2.

The friction coefficient μ is not considered further in this analysis.

Assumptions:

(a) V_x, V_z are constant during spin-up.

(b) μ is constant during spin-up.

(c) Contact patch area is proportional to tire deflection.

(d) Wear is the integral of contact patch area x sliding distance.

Result:

$$\frac{\text{volume lost}}{\text{volume of tire}} = \frac{1}{\mu}\sqrt{\frac{D}{W}}\left[\frac{V_x^2 I_y}{D^4 K_z}\right]$$

V_x = touchdown speed

I_y = polar moment of inertia

D = tire diameter

K_z = tire vertical stiffness

$$\text{Touchdown Severity} = \left[\frac{V_x^2 I_y}{D^4 K_z}\right]$$

A dimensionless number.

Figure 2 - Touchdown Severity Index.

LABORATORY TESTING

Based on the concept of dimensionless parameters, small scale tires were fabricated from Buna N (nitrile) O-rings mounted on nylon pulleys. These miniature wheels were mounted on an axle, which in turn could be forced into sudden touchdown to a rotating abrasive disc via a solenoid and a controlled timing circuit. By adjusting the point of touchdown on the disc from an inner position to the outer edge, touchdown velocity could be varied from 100 to slightly over 200 feet per second. By using inertia rings attached to the nylon wheel, polar moment of inertia could be varied. Using both of these as variables, the dimensionless severity index could be varied from values of approximately 10 up to 200.

The timing circuit was adjusted to bring the wheel-tire into contact with the spinning abrasive disc for 0.4 sec., a time sufficient to spin up, and then to retract it for 10 sec., allowing the wheel to spin down to rest by bearing friction effects.

Ten touchdowns were used to make one complete set at a given condition. Weight of the tire-wheel was recorded both before and after the ten runs using a sensitive laboratory balance.

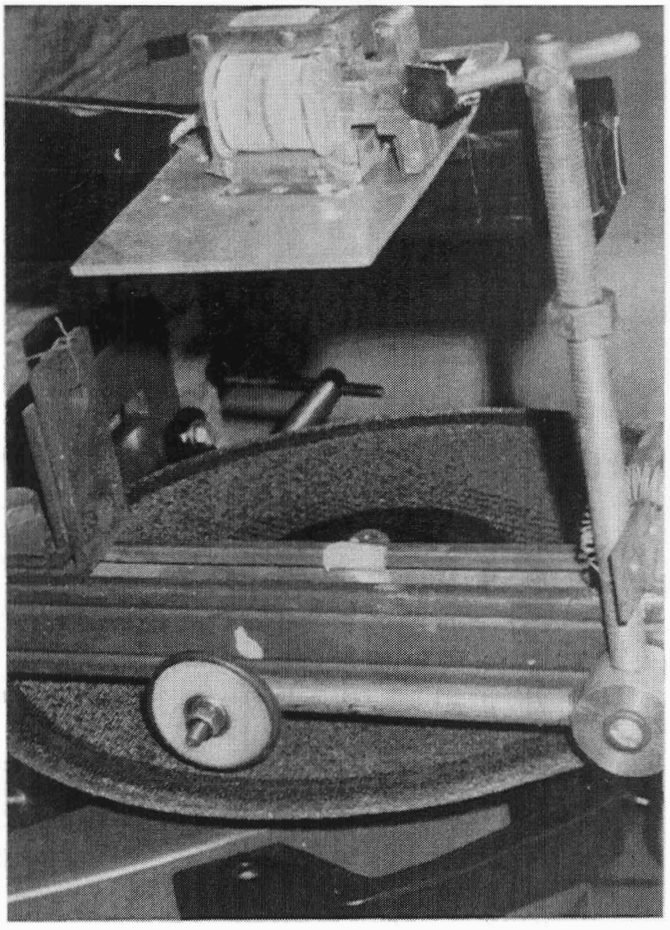

Figure 3 - Small scale test apparatus for touchdown wear.

LABORATORY DATA ON BUNA N (NITRILE)

Using the laboratory apparatus described on the previous page, data on Buna N (nitrile) rubber was obtained over a very wide range of values of the severity index, up a value of nearly 200. The values obtained were plotted as percent weight loss of the small tire due to ten touchdowns vs. severity index number. The data show a relatively smooth increase in weight loss as severity index increases.

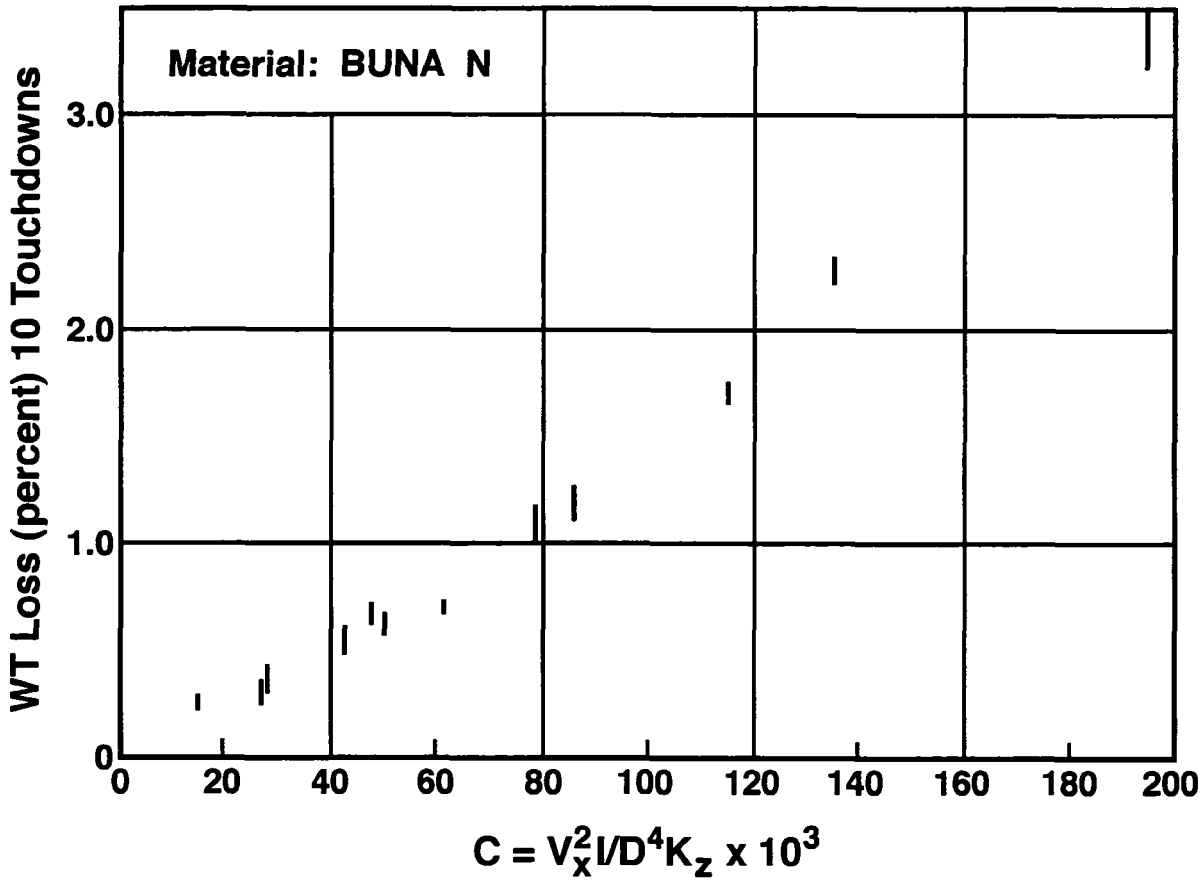

Figure 4 - Percent weight loss vs. severity index.

LABORATORY DATA ON NR AND NR-SBR COMPOUNDS

Further data was obtained by fabricating small scale tires from compounds similar to those used in commercial aircraft tire treads. These were plotted against increasing severity index, and compared with the Buna N data previously obtained. As might be expected, the commercial compounds exhibited less wear. Two compounds were studied. The first, denoted No. 3 and plotted in Fig. 5 as circles, is a 100% NR compound. The second, denoted No. 13, is a 65% NR-35% SBR compound. They appear to be very close in their resistance to touchdown wear, but both are clearly more resistant than nitrile.

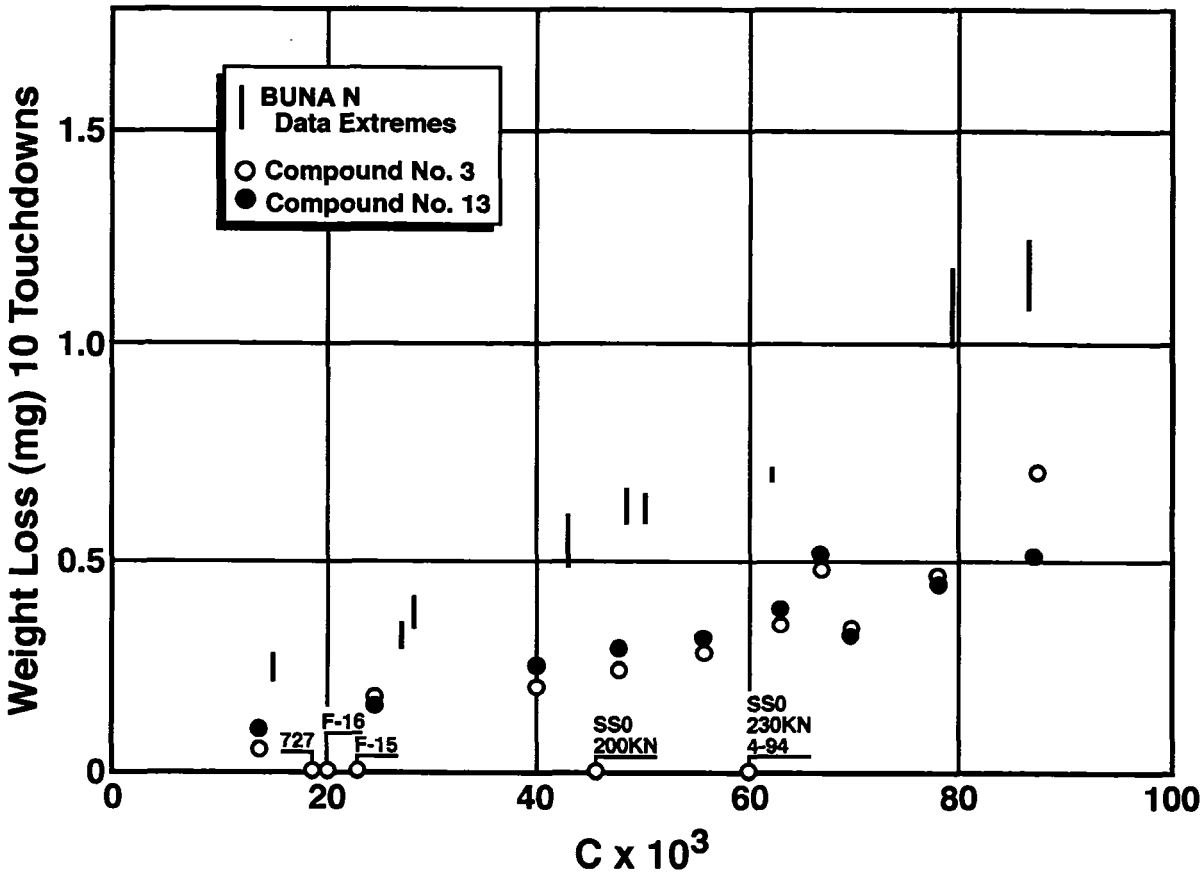

Figure 5 - Weight loss at ten touchdowns vs. severity index.
Three compounds.

ANALYSIS OF SHEAR STRESS

It is known that at high values of the severity index cutting of the tread can occur. In order to examine the information available from this simplified analysis, the shear stress caused by touchdown is calculated by forming the ratio of the tangential force to the contact area. The resulting value of shear stress is probably as good a measure of cutting as is available. The resulting expression is primarily dependent on tire vertical stiffness K_z, which in turn is controlled to a great extent by inflation pressure. This implies that cutting is most severe at high inflation pressures, but gives little other insight to the phenomenon, since there is in this analysis no simple means for defining the counter surface.

Contact Area A = $\pi\delta_z\sqrt{\omega D} = \pi V_z\, t\sqrt{wD}$

Tangential Force $F_x = \mu F_z = \mu\, V_z\, t\, K_z$

Shear Stress $\tau_x = F_x / A = \frac{\mu}{\pi} \quad \frac{K_z}{\sqrt{wD}}$

Figure 6 - Shear stress as a measure of cutting.

SPIN DOWN TEST ANALYSIS

In order to utilize existing spin down data, an analysis was conducted on the problem of a spinning tire, held at zero forward velocity, allowed to drop onto a rigid fixed surface. The result showed that the ratio of tread loss to tire volume is controlled by the same dimensionless severity index as obtained previously. In this particular case, a modified spin down experiment was considered in which the tire deflection was limited to preset value $\bar{\delta}$ by the use of air cylinders simulating aerodynamic lift. The specific value of $\bar{\delta}$ does not appear in the resulting volume loss. The rotational velocity decreases linearly with time in this analysis, as shown in Fig. 7.

Modified Spin Down Test

$\bar{\delta}$ = allowable tire deflection

Other assumptions same

$$\frac{V_L}{V_T} = \frac{1}{\mu}\sqrt{\frac{D}{w}}\left[\frac{V_x^2 I}{D^4 K_z}\right]$$

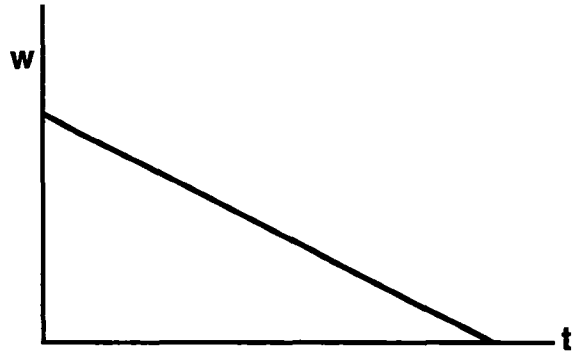

Figure 7 - Volume loss and spin down speed.

SPIN DOWN TEST SPEED

Full-scale spin down tests were conducted to evaluate tire wear under this condition. Instrumentation was installed to measure wheel and tire rotational speed during the test, and typical values of this data are shown in Fig. 8. The wheel speed decreases almost linearly with time, and this is in good agreement with the result of the analysis shown in Fig. 7.

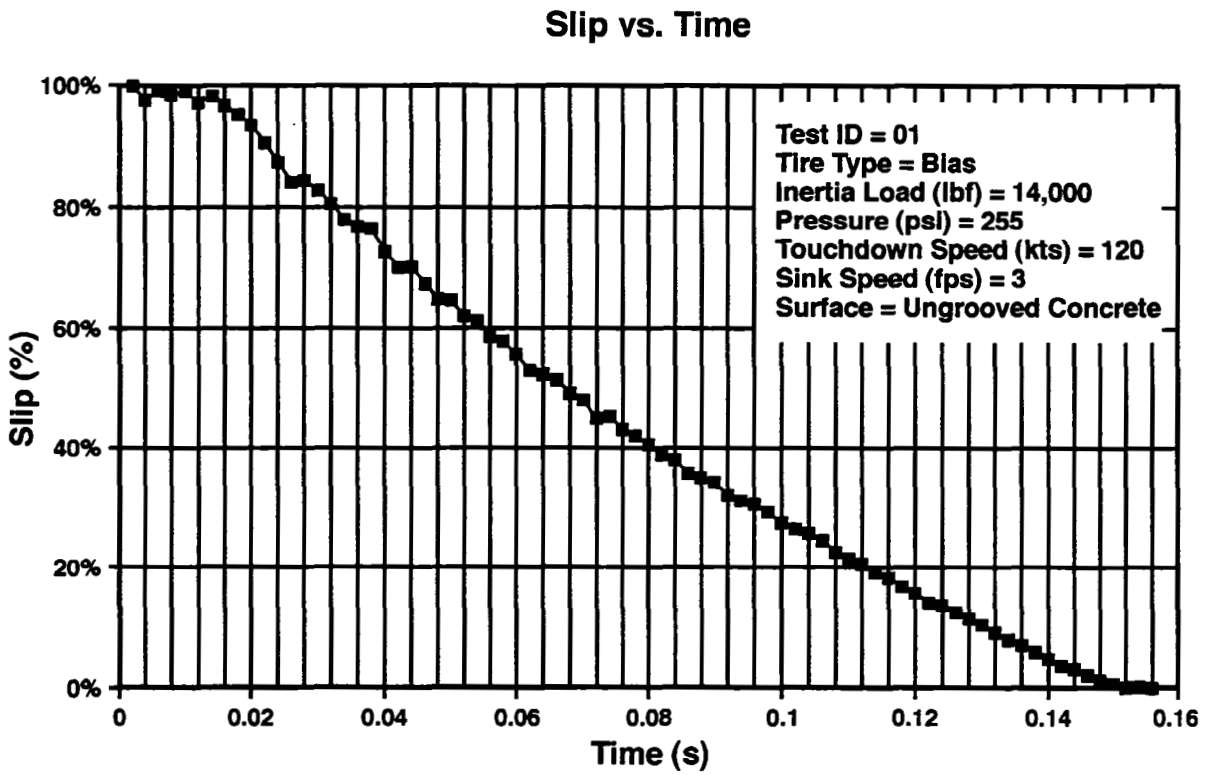

Figure 8 - Wheel speed vs. time on spin down test.

WEIGHT LOSS VS. TOUCHDOWN SEVERITY

Using data from the full-scale drop tests, expressed as percent of tire weight for ten touchdowns, and from the small-scale NR and NR-SBR laboratory tires, a single combined plot of data can be produced as a function of touchdown severity. This shows that the resulting loss values are similar in magnitude, although the full-size data exhibits some scatter. The mass of the small tire was 2.4 grams, while that of the full-size tire was over 18,000 grams. Both bias and radial tires were used in the full-size test plan.

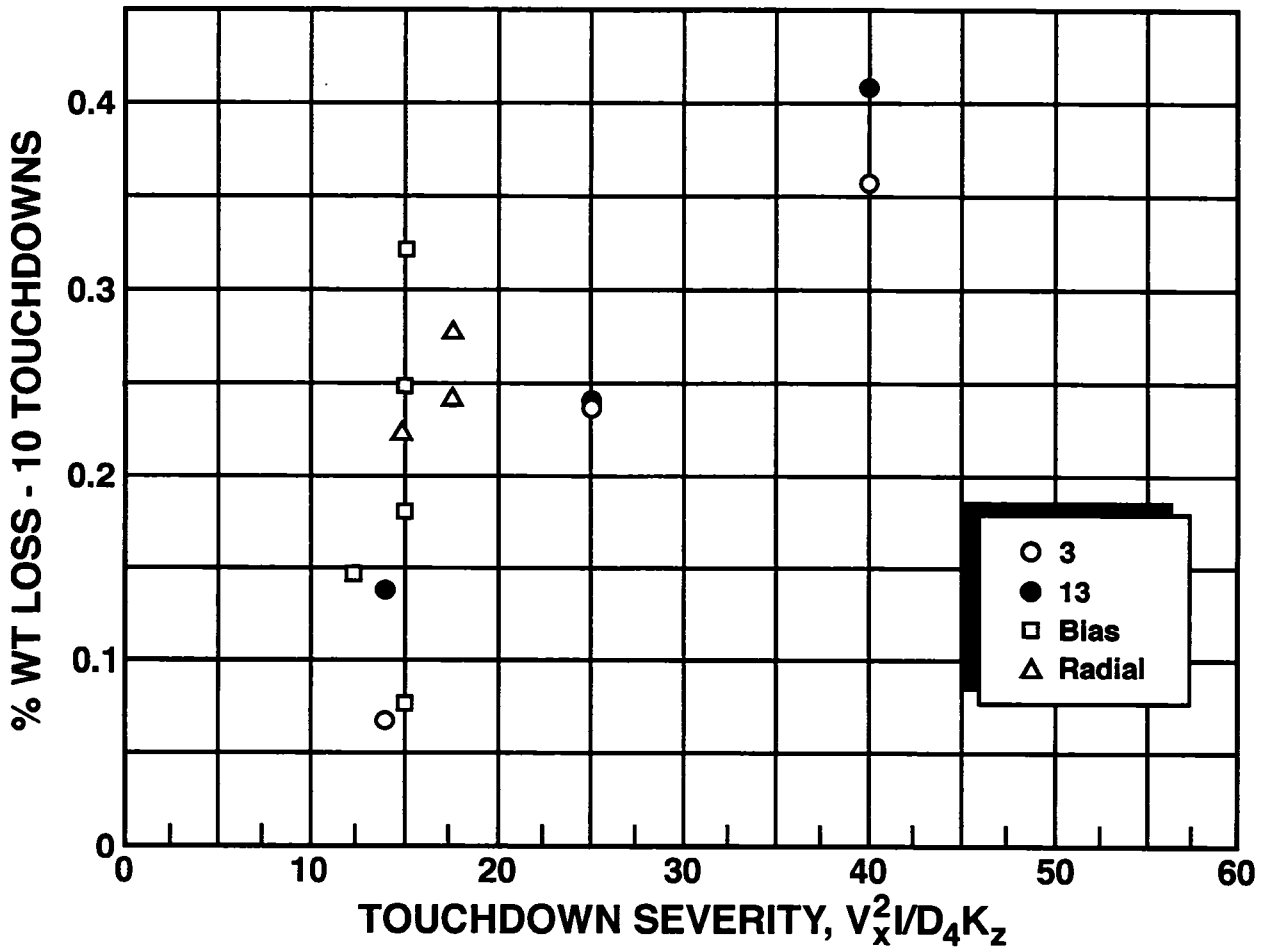

Figure 9 - Weight loss for both small-scale and full-size tires vs. touchdown severity index.

SEVERITY INDEX

The touchdown severity index may be useful as a measure of the damage (abrasion, ablation or cutting) which is experienced by a tire during spin-up. Little reliable full-size tire data is available as yet to assess the validity of such predictions, but it is hoped that such data may be obtained in the future.

This index may be interpreted as the ratio of the spin-up kinetic energy to the potential energy of the deflected tire, as shown in Fig. 10.

$$\left[\frac{V_x^2 I}{D^4 K_z}\right] = \left(\frac{V_x}{D}\right)^2 I/\left(D^2 K_z\right) = \frac{\text{K.E. of Tire \& Wheel Assembly}}{\text{P.E. of Deflected Tire}}$$

Figure 10 - Touchdown severity index.

Requirements for Energy Based Constitutive Modeling in Tire Mechanics

John R. Luchini, Jim M. Peters and Will V. Mars
Cooper Tire and Rubber Company
Findlay, OH

REQUIREMENTS FOR ENERGY BASED CONSTITUTIVE MODELING IN TIRE MECHANICS

John R. Luchini, Jim M. Peters and Will V. Mars
Cooper Tire and Rubber Company
Findlay, Ohio

ABSTRACT

The history, requirements, and theoretical basis of a new energy based constitutive model for (rubber) material elasticity, hysteresis, and failure are presented. Energy based elasticity is handled by many constitutive models, both in one dimension and in three dimensions. Conversion of mechanical energy to heat can be modeled with viscoelasticity or as structural hysteresis.

We are seeking unification of elasticity, hysteresis, and failure mechanisms such as fatigue and wear. An energy state characterization for failure criteria of (rubber) materials may provide this unification and also help explain the interaction of temperature effects with failure mechanisms which are described as creation of growth of internal crack surface.

Improved structural modeling of tires with FEM should result from such a unified constitutive theory. The theory will also guide experimental work and should enable better interpretation of the results of computational stress analyses.

OUTLINE

Introduction
- Background
- Thesis

Problem Statement
- Generalized, unified three-dimensional theory of elasticity and fatigue
- Assumptions/constraints for elasticity
- Assumptions/constraints for hysteresis and fatigue
- Reasonable experiments to obtain parameters

Energy Based Elasticity Theory
- Elasticity from energy
- Thermo-mechanical interaction

Entropy Based Damage Theory
- Damage criteria aids FEM interpretation
- Thermal hysteresis and entropy
- Hysteresis and Fatigue Damage

Conclusions
- Hysteresis, thermal energy and entropy
- Model form and flow chart

References and Bibliography to Related Work

INTRODUCTION
Background

This essay is part of our current research on "an energy based theory for three-dimensional elasticity, hysteresis, fatigue and wear." The word "essay" has its roots in the Latin verb for "to try." This presentation documents our current efforts, but not a final form for others to use. We hope that by presenting this admittedly preliminary discussion, we may stimulate other experts to aid in the search for an improved three-dimensional constitutive model for rubber. These others may offer insights as well as rigor to the concepts presented here. This three-dimensional constitutive model for rubber would ideally encompass three-dimensional elasticity as well as criteria for material damage or failure including hysteresis, fatigue and wear.

The objective of this research is to develop a new, unified set of constitutive relations for an energy based material theory for the materials used in our product. Our emphasis on material property modeling was initially directed toward identifying better ways to provide input to the FEM computer programs and better ways to use material properties to interpret the output of the FEM programs.

In an article [1] describing the fate of the ship "Titanic" and the space shuttle "Challenger," a common theme was identified. In 1912, no one understood how the Titanic's steel would react when subjected to 31°F water temperature. The article claimed that many technological disasters could be traced to a common warning: know your materials.

In the last decade researchers in tire mechanics have developed significant insights and understanding of the mathematical material model needed by the FEM technology [2-8]. We have achieved a level of technical sophistication with the FEM technology such that shortcomings in the laboratory measured material properties showed as a limitation in the utilization of FEM.

Our current work on an energy based material theory started as a result of a meeting among personnel from research and materials development to discuss the differing requirements from testing for properties needed to use FEM, and to develop compounds. We saw that the current test results were distinct but that they should have some common basis which would allow a single set of tests to provide information which could be used for both FEM and materials development.

We realized that a single underlying theory used in the creation of new material tests would not need separate tests for each application. The required test(s) may be more complex than any single current test but would provide a deeper understanding of the material being used or developed and would eventually lead to simpler and more distinguished tests.

Thesis

Energy theories for elasticity of a material are based entirely on the capacity of the material to generate, tolerate and contain energy as described in the Principle of Virtual Work and Castigliano's Theorem. The fatigue damage limit of a material might be entirely controlled by the capacity of the material to generate, tolerate and contain entropy. We propose a unified formulation of rubber behavior based on the Conversion of Energy Law and the Increase in Entropy Principle.

PROBLEM STATEMENT
Generalized Unified Three-Dimensional Theory of Elasticity and Fatigue

Energy based elasticity theories for the three-dimensional constitutive model for rubber should:
- provide a theory to guide experiments and analysis of results
- define inputs for FEM characterization of the material
- provide material based criteria to use in FEM evaluations
- combine what we know and what we need into a single framework
- be based on scalar quantities such as the energy in the material.

There are energy based elasticity theories, but we wanted to unify these with an energy based theory for hysteresis and accumulated damage. A unified energy theory should express theoretical relationships among material hysteresis, one-dimensional material modulus, three-dimensional elasticity modulii, and material fatigue. This theory must be applicable to rubber and should be consistent with SED fatigue theories, rubber incompressibility, and the DIOSS hysteresis theory. This model should include SED and temperature relationships to enhance the interpretation of FEM results. The constitutive model should be consistent with energy based elasticity as noted above and should also provide a theory for:
- an "energy capacity" of the material related to the energy input
- the cycle of energy the material must survive
- the hysteresis damage which may be accumulated before failure.

For several years FEM studies have used and displayed a scalar quantity called "strain energy density" (SED) which "summarized" the stresses and made tire to tire comparisons simpler. While this provides an engineer with a simple graph to analyze, it does not interpret how different rubber compounds will react to similar levels of strain energy nor how many cycles a specific compound can tolerate at operating temperature. Thus, a better model for the material was needed but we were unable to find such a model in the technical literature.

PROBLEM STATEMENT
Assumptions/Constraints for Elasticity

The following is a list of the primary assumptions for the proposed material model:

1. Uniaxial tension and compression stress-strain behavior which has been observed and modeled must be derivable from the general three-dimensional theory. Experiments performed in one direction must provide data for modeling the material behavior in other directions as well.

2. Shear stress-strain behavior is isotropic.

3. Shear stress-strain behavior is independent of the normal stress-strain behavior. This is based on data and analysis in a paper by Meineke and Porter [9].

4. Volume is constant, even at large strains. Large distortions must be accommodated by the theory, and initial volume and final distorted volume must be the same. Note that Poisson's ratio, which is defined for infinitesimal strains, will be a function of strain. Based on this fact, the classically defined Poisson's ratio should not be an input at all.

5. Normal, volumetric, and shear elasticity parameters for the model may be used to derive equivalent values (at zero strain) for the classical elastic constants: Young's modulus, E, the shear modulus, G, and the Poisson's ratio, ν. The derived values should correspond to the experimentally determined values in the literature.

6. Normal, volumetric and shear elasticity in the model may be approximated as linear functions (single values) for low strains. However, for larger tensile, compressive, or shear strains, they must be nonlinear functions.

7. The elasticity model must provide for or permit functional relationships of stresses and strains with temperature. Frequency effects, or other parameters, which are determined to be important must be handled in a way that is consistent with the hysteresis and failure theories which are under parallel development.

PROBLEM STATEMENT
Assumptions/Constraints for Hysteresis and Fatigue

A paper presented at the Tire Society last year pointed out that there is no uniquely good way to analyze and interpret tire three-dimensional stress analysis problems [2]. To develop a new fatigue theory, we are considering available theories of polymer fatigue from a distortional energy basis. This has led us in the direction of an entropy capacity fatigue model. The theoretical model we desire will:

1. View hysteresis as a result of an internal (dry) friction process [3] which creates an accumulation of entropy within the material micro-structure.

2. Blend with, or extend, the DIOSS theory for hysteresis related to distortional energy to include fatigue and elasticity. This can be modeled as: H=B*exp(-rT)*(A0SS^2)/(1+P0SS).

3. Demonstrate that higher hysteresis within the material reduces crack growth rate due to energy dissipation.

4. Have material properties or parameters which can be used in tire stress analysis. There are theories which may work but are incompatible with the other assumptions used in tire analysis.

5. Be implemented into FEM and coupled with stress/strain analysis for durability prediction.

6. Avail itself of straight-forward laboratory tests which can be used directly for materials development, and provide data for material properties or parameters.

PROBLEM STATEMENT
Reasonable Experiments to Obtain Parameters

The motivation for needing a new constitutive relationship is the unique behavior of filled, vulcanized polymers. While the points listed in the previous page must be part of the foundation for the new three-dimensional model, they are not sufficient to specify the experiments which define the parameters for the material properties. This parametrization will probably require unique tests and measurements to define material parameters.

Energy storage modes within the material would include: strain energy; thermal energy; chemical energy stored in bonds; and a "surface energy" which increases as surface is formed as in crack growth or fracture.

Entropy capacity of the material would include factors such as: the ability of the chemical bonds to stretch, bend, or rotate; volume of the material (for "entropy density"); and the spatial distribution of material components of different entropy capacities including both structural features and dispersion.

Characterization of rubber compound behavior in the past has utilized various tests. Future experimental analysis techniques must be consistent with these results. In addition, rubber compounds used in tires exhibit characteristics which the new constitutive model must include. The features of the model must:

- provide for a nonlinear relation between stress and strain
- provide for anisotropic behavior, and describe stress and strain uniquely in different directions
- provide for incompressibility and permit distortion with no volume change. There is a temperature volume change effect.
- possess a firm theoretical foundation, be experimentally verifiable and compatible with existing FEM theory.

ENERGY BASED ELASTICITY THEORY
Elasticity From Energy

The Mooney-Rivlin material model quantifies rubber modulus in terms of two tensor invariants. One of these relates to the energy stored in the material by compression and the other energy stored by shear. It is generally agreed that all energy stored by a compressive stress on an incompressible material is elastic, that is, fully recoverable. However, some of the energy input as shear will not be recovered. Experimental measurements of the Mooney-Rivlin constants for carbon black filled rubber show different values in extension, compression and shear. In other words, the "constants" depend on the strain conditions and would require complex computer coding to obtain a result which is both physically meaningful and mathematically stable.

The use of a scalar quantity such as SED or energy is a common approach in constitutive material modeling because it permits the development of an unambiguous three-dimensional theory from a theory developed in one dimension. We have noted that the existence of constant values for E, G and ν imply a volume change for the material under stress. We have conducted laboratory measurements to confirm the non-tire industry research published in 1993 [10] on a new constitutive model for rubber using a variable for Poisson's ratio. The assumption that the shear modulus and material volume must remain constant implies that the modulus, "E", and/or Poisson's ratio, "ν", must generate a nonlinear relation between stress and strain.

Nonlinear modulus theories which are not based on scalar quantities can develop mathematical difficulties or predict nonphysical results when extended into three dimensions. One such case is the use of nonlinear rubber modulus in the current Cooper FEM program. This created directional properties in the elements under stress which were not seen in real tires and which caused mathematically unstable computations. The incompressibility material model in the current Cooper FEM program must be computationally complex in order to prevent these mathematical difficulties.

The "Directional Incremental Octahedral Shear Strain" theory ("DIOSS") quantifies rubber hysteresis in laboratory experiments and provides parameters for use in FEM analyses. This theory uses a scalar quantity, Octahedral Shear Strain (OSS), to compute the quantity of energy lost to hysteresis. The research completed shows that the OSS is related to the distortional energy mechanically put into the material, some of which is lost to hysteresis.

A combination of the Mooney-Rivlin tensor invariant related to the energy stored in the material by compression and the DIOSS scalar quantity for energy stored by shear and lost to hysteresis could form the foundation for a new three-dimensional constitutive model. The model would retain the hyseretic response from our DIOSS theory. The new constitutive model could also have terms for the elastic response which would replace current elastic modulus in FEM.

The features we desire in the theory should be based on tensor invariants in order to provide a nondirectional material model. This is desirable in order to be both physically meaningful based on the observed experimental data as well as providing for a mathematically stable solution.

ENERGY BASED ELASTICITY THEORY
Thermo-Mechanical Interaction

We have noted that a mechanical cycle puts energy into the material and then removes it. While we can remove enough energy to return the material to its original energy density, some entropy increase will persist in the material after the cycle is complete.

In several papers [2-8] the thermo-mechanical interactions which occur in tires have been modeled with sequential applications of FEM stress analysis, a stress-strain to hysteresis thermal energy estimate, and a thermal analysis. Some of these approaches allow for iterative solutions, but none directly allow for interaction of the thermal and mechanical energies. A diagram, shown below, describes a way these energies may interact.

ENTROPY BASED DAMAGE THEORY
Damage Criteria Aids FEM Interpretation

The general answer to the need for a three-dimensional elasticity theory should be in terms of energy. Elastic strain energy is one form of energy and hysteresis is another form. There are problems with this approach in terms of the mechanical analysis available from FEM. We are able to compute the response of the material in three-dimensional space, but the computation of energy (either strain energy or hysteretic energy) eliminates the directional information. We need a computation which can be done within FEM before the directional information is lost.

An analog of the computation required is the "wind-chill index" from the weather reports. Temperature is a scalar quantity similar to energy. However, your body is actually responding to heat transfer (energy flux) when you say you are cold. A correspondence between a person's level of comfort in a given "still air" temperature and the current temperature and wind velocity, related via heat transfer coefficients, is the "wind-chill index."

We need to identify what the material is actually responding to at a given level of energy. Then we may be able to create one or more indices which can be computed within the FEM program to correspond to the material's potential discomfort. Since we are dealing with tensors rather than vectors, we expect that at least two indices would be needed.

As an example, consider an "elastic strain-energy index" and an "hysteretic energy index" which could have critical values for various failure modes. Another set of indices could be a dilational energy index" and a "distortional energy index" which could have critical values for energy storage and energy dissipation, respectively. Unfortunately, we do not know which set of indices are desirable to compute, nor how to compute these desirable indices in a way which accurately represents the material's level of discomfort.

ENTROPY BASED DAMAGE THEORY
Thermal Hysteresis and Entropy

The concept which has emerged has variously been called a "material wind-chill index," the "material energy limit," the "energy capacity," or the "hysteretic energy index." The hysteretic energy index would be a material property which describes the ability of a material to tolerate hysteresis. A term we have coined, the "thermal hysteresis" would be the heat energy left over after a thermal loading has been applied to a system and then removed. We now think the idea we have been describing is actually entropy generation within a material.

For example, consider a slab of rubber heated from 75°F to 150°F and then cooled once again to 75°F. The difference between the thermal energy input to the rubber sample and the thermal energy returned after cooling would be zero for an ideal material. However, the heating process is not completely reversible and the difference between the thermal energy input and the thermal energy returned would be the thermal hysteresis of the material. Based on the first law of thermodynamics the above may be written as:

Thermal energy input = thermal energy output + thermal hysteresis

This thermal hysteresis process is the same as the principle of increase in entropy from the second law of thermodynamics. While entropy may be conserved during idealized reversible processes, entropy is generally a nonconserved property. There is no such thing as the conservation of entropy principle, and it increases during all actual processes.

Heat transfer to a system increases system entropy along with the energy increase. Heat transfer from a system decreases both the energy and the entropy of the system. Entropy change as a result of reversible heat transfer is called entropy flow and does not involve any entropy generation.

Irreversibilities such as friction, fast expansion or compression, and heat transfer through a finite temperature difference always cause the entropy to increase. It is hypothesized that the material damage is a result of the entropy increase and/or can be quantified as proportional to this thermal entropy increase.

Energy theories for elasticity of a material are based entirely on the capacity of the material to generate, tolerate, and contain energy, as described in the principle of virtual work and Castigliano's Theorem. The fatigue damage limit of a material might be entirely controlled by the capacity of the material to generate, tolerate, and contain entropy rather than energy.

Thermal energy input by itself is not assumed to cause material damage, although it can change the physical properties of the material and thus affect the loading conditions. The damaging portion of the thermal energy, the "thermal hysteresis," is the entropy increase which results from chemical changes in the material. This entropy increase would be a function of time, and could also be used to explain the effects of aging on rubber.

We hypothesize that, for a given application, there is a "material limit" for entropy generation, instead of energy content. In such a material constitutive model, the material's life is determined by the quantity of entropy generated throughout its history. When this quantity exceeds the limit, it is considered to have failed. This principle should be reconcilable with accumulated damage theories such as Miner's Rule.

ENTROPY BASED DAMAGE THEORY
Thermal Hysteresis and Entropy (Cont'd.)

If we could quantify a property of the rubber for the entropy generation rate as a function of strain and temperature, we should be able to integrate over time to find the total entropy generated. This entropy generated and accumulated in the material would quantify the total damage done in the cycle of strain and temperature. By these hypotheses, the energy content at a given time and the total accumulated entropy would determine the elasticity and life of the material. The damage done to the material would be equivalent to that done by heat and could be called the thermal hysteresis or accumulated entropy generation.

ENTROPY BASED DAMAGE THEORY
Hysteresis and Fatigue Damage

This paper proposes that fatigue damage is the accumulation of entropy. The discussion here also implies that thermal hysteresis by itself could be used to predict durability. The "energy limit" of a material we initially described is now seen as the amount of thermal energy needed to increase the entropy beyond the material's tolerance and thus cause material failure.

This "energy/entropy limit" is still an imprecise concept and we have no straight-forward laboratory process to measure it. However, there is a strong analogy between what happens to the rubber mechanically and what happens thermodynamically during a fatigue process. The following diagram depicts the analogy between heat energy, Q, and mechanical stress, σ.

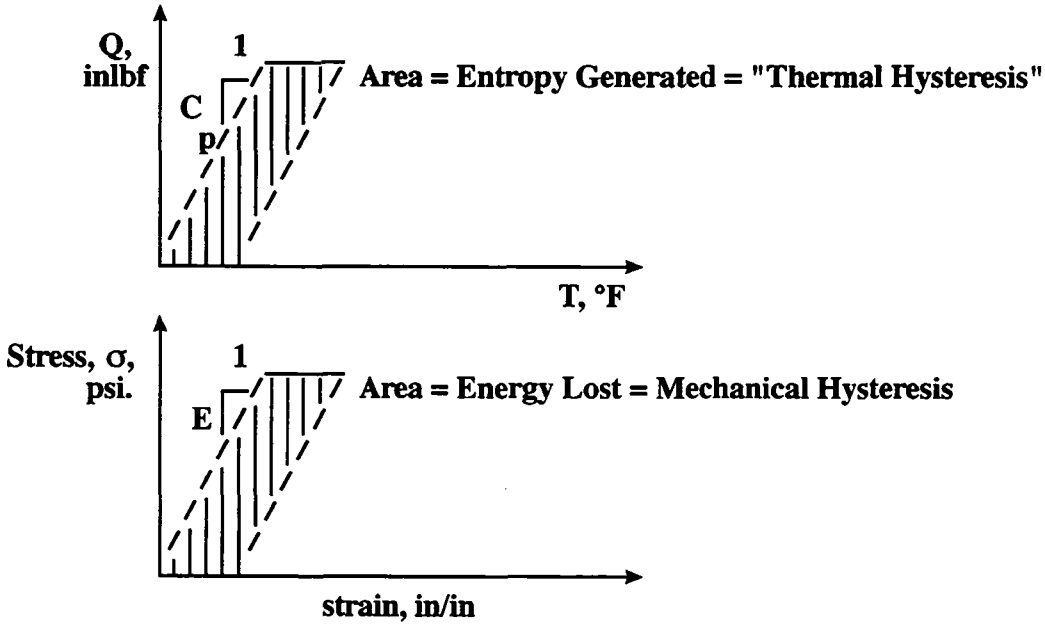

CONCLUSION
Hysteresis, Thermal Energy and Entropy

While there are good energy based elasticity theories, we have been unable to find or develop a good entropy/energy based damage theory. We, therefore, are proposing "HEAT," the hysteretic entropy accumulation theory. HEAT claims that entropy generation occurs due to irreversible microscopic structural changes, at the elastomer network level. Energy loss occurs due to irreversible macroscopic structural changes, at the filler level. While the friction generated macroscopically would not damage the rubber, irreversible changes in the elastomer network would damage the rubber. Energy lost due to macroscopic irreversibilities shows up as heat, part of which ends up causing microscopic irreversibilities.

This model would encompass chemical interactions that occur in the rubber. Chemical interactions (changes to the molecular network) would be the source of entropy generation, just as friction between filler particles is the source of energy loss.

One reason that hysteresis is historically related to fatigue damage may be due to the heat generation which results from mechanical losses. In a "real" material mechanical hysteresis presents itself as a temperature rise. This temperature rise is a thermal energy input, and as that thermal energy input dissipates into the environment the material would accumulate an entropy increase. It is our hypothesis that the entropy is either the cause of the damage or the result of the damage, but in either case it provides a measure of the damage. The material property which we seek is one which can be used to quantify the material's tolerance of the entropy accumulation.

CONCLUSION
Model Form and Flow Chart

A schematic idea of how the HEAT fatigue/damage accumulation process would operate is shown below. This model not only addresses the mechanisms of fatigue, but could also be used to describe rubber aging.

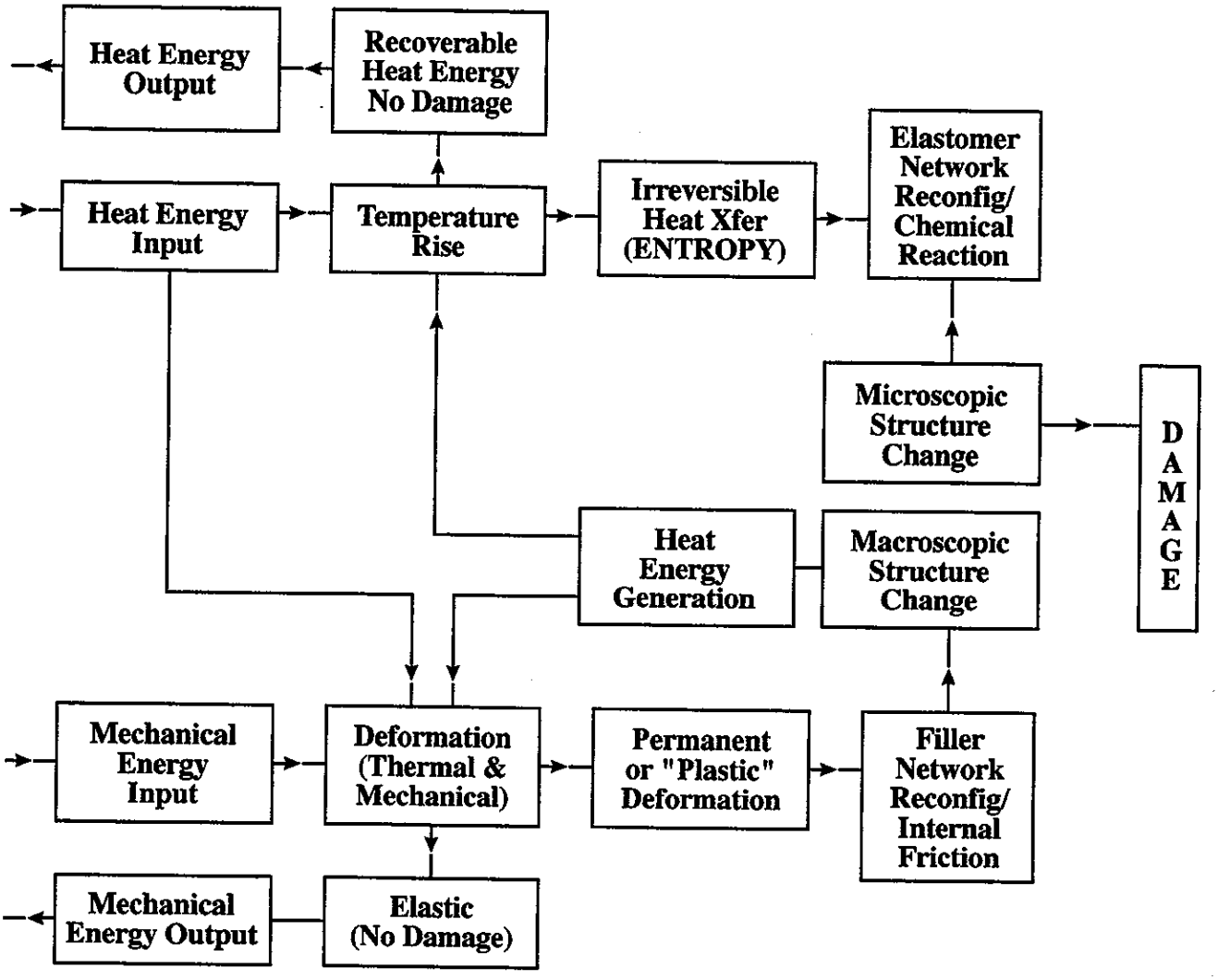

REFERENCES

1. Schwarz, Frederic, "Deep Thoughts," *Invention and Technology*, Summer 1994.

2. Ebbot, T. G., "An Application of Finite Element Based on Fracture Mechanics Analysis to Cord/Rubber Structures," presented at the Tire Society Meeting, March 24, 1993 (to appear in *Tire Science and Technology*).

3. Luchini, J. R., Peters, J. M., Arthur, R. H., "Tire Rolling Loss Computation with the Finite Element Method," presented at the Tire Society Meeting, March 23, 1993 (to appear in *Tire Science and Technology*).

4. Whicker, D., Browne, A. L., et al, "A Thermo-Mechanical Approach to Tire Power Loss Modeling," General Motors Research Laboratories Research Publication GMR-3310, May 30, 1980. Portions also published in SAE Papers 810161-810164, and *The General Problem of Rolling Contact*, AMD Vol. 40, ASME, NY, 1980.

5. Sakar, K., Kwon, Y. D., Prevorsek, D. C., "A New Approach for the Thermomechanical Analysis of Tires by the Finite Element Method," *Tire Science and Technology*, Vol. 15, No. 4, Oct.-Dec. 1987.

6. Warholic, T. C., *Tire Rolling Loss Prediction From the Finite Element Analysis of a Statically Loaded Tire*, M.S.E. Thesis, University of Akron, 1987.

7. Yavari, B., Tworzydlo, W. W. and Bass, J. M., "A Thermomechanical Model to Predict the Temperature Distribution of Steady-State Rolling Tires," presented at the Tire Society Meeting, March 1992.

8. Dehnert, J. and Volk, H., "An Approach to Predict Temperature Distributions in Rolling Tires Using the Finite Element Method," presented at the Tire Society Meeting, March 1991.

9. Porter, L. S. and Meineke, E. A., "Influence of Compression Upon the Shear Properties of Bonded Rubber Blocks," *Rubber Chemistry and Technology*, Vol. 53, No. 5, Nov.-Dec. 1980.

10. Erickson, L. L., "A New Constitutive Equation for Elastomers," *Rubber and Plastics News*, March 15, 1993.

Bibliography to Related Works

1. Whiteman, I. R., "A Mathematical Model Depicting the Stress-Strain Diagram and Hysteresis Loop," *Journal of Applied Mechanics*, March 1959.

2. Luchini, J. R., *Mathematical Model for Rubber Hysteresis*, Ph.D. Dissertation, University of Michigan, 1977.

3. Stechschulte, R. A. and Luchini, J. R., "A Laminated Composite Solid Element ...," *Tire Science and Technology*, Vol. 15, No. 1, Jan.-March 1987.

4. Kenny, T. M. and Stechschulte, R. A., "Applications of Finite Element Analysis in Tire Design," *Tire Science and Technology*, Vol. 16, No. 2, April-June 1988.

A Kinematically Driven Anisotropic Viscoelastic Constitutive Model Applied to Tires

Arthur R. Johnson, John A. Tanner and Angela J. Mason
NASA Langley Research Center
Hampton, VA

A KINEMATICALLY DRIVEN ANISOTROPIC VISCOELASTIC CONSTITUTIVE MODEL APPLIED TO TIRES

Arthur R. Johnson†, John A. Tanner‡, and Angela J. Mason‡
NASA Langley Research Center
Hampton, VA 23681-0001

INTRODUCTION

Aircraft tires are composite structures manufactured with viscoelastic materials such as carbon black filled rubber and nylon cords. When loaded they experience large deflections and moderately large strains. Detailed structural models of tires require the use of either nonlinear shell or nonlinear three dimensional solid finite elements. Computational predictions of the dynamic response of tires must consider the composite viscoelastic material behavior in a realistic fashion. In this extended abstract we describe a modification to a nonlinear anisotropic shell finite element so it can be used to model viscoelastic stresses during general deformations. The model is developed by introducing internal variables of the type used to model elastic strain energy. The internal variables are strains, curvatures and transverse shear angles which are in a one-to-one correspondence with the generalized coordinates used to model the elastic strain energy for nonlinear response. A difference-relaxation equation is used to relate changes in the observable strain field to changes in the internal strain field. The internal stress state is introduced into the equilibrium equations by converting it to nodal loads associated with the element's displacement degrees of freedom. In this form the tangent matrix in the Newton-Raphson solution algorithm is not modified from its form for the nonlinear statics problem. Only the gradient vector is modified and the modification is not computationally costly. The existing finite element model for the Space Shuttle nose gear tire is used to provide examples of the algorithm. In the first example, the tire's rim is displaced at a constant rate up to a fixed value. In the second example, the tire's rim is enforced to follow a saw tooth load and unload curve to generate hysteresis loops.

† MS240, Army Research Laboratory, Computational Structures Branch.

‡ MS497, Structural Dynamics Branch.

SPACE SHUTTLE NOSE GEAR TIRE LOADING AND UNLOADING DATA

Loading and unloading a Space Shuttle nose gear tire results in a hysteretic load displacement curve. The curve shown below was taken from Ref. 3. It is clearly seen that a significant amount of energy is not recovered during unloading. The objective of this effort is to develop a computational method to model general time dependent deformations of composites using stress and strain measures similar to those used to model the elastic (time independent) material behavior; that is, to make maximum use out of the existing form of the nonlinear finite element code and the energy method which it is based upon. The model can then be used to predict the hysteretic behavior of tires so as to improve their design for enhanced performance and life.

The work presented in this extended abstract is limited to a brief description of the computational method developed and of its use to simulate tire loading and unloading.

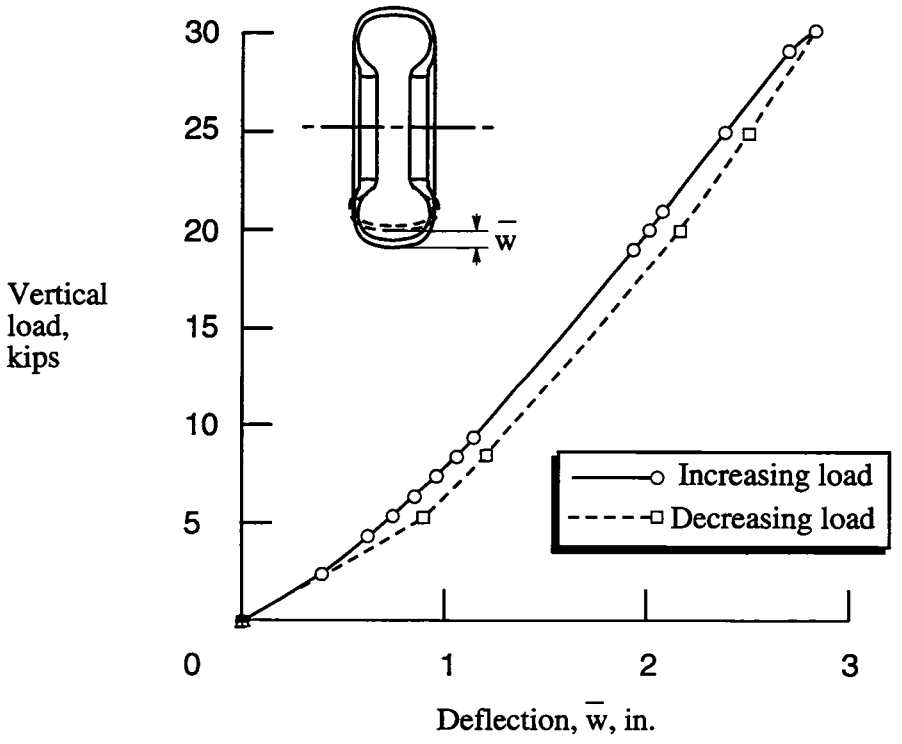

Load deflection data for Space Shuttle nose gear tire.

NONLINEAR SHELL ELEMENT AND TIRE MODELING CODE

A shell element capable of modeling geometrically nonlinear deformations of laminated composites developed by Noor, et al [1,2] is shown below. It is the element used in NASA's tire footprint finite element code. This shell element has nine displacement nodes with five variables at each node and four stress nodes with eight variables at each.

The NASA tire footprint code[3] allows the user to generate a tire stress analysis model based on shell theory. The code can then simulate the tire inflation and enforced rim displacements with the tire pressing against a frictionless flat surface (for a surface with friction see Ref. 4).

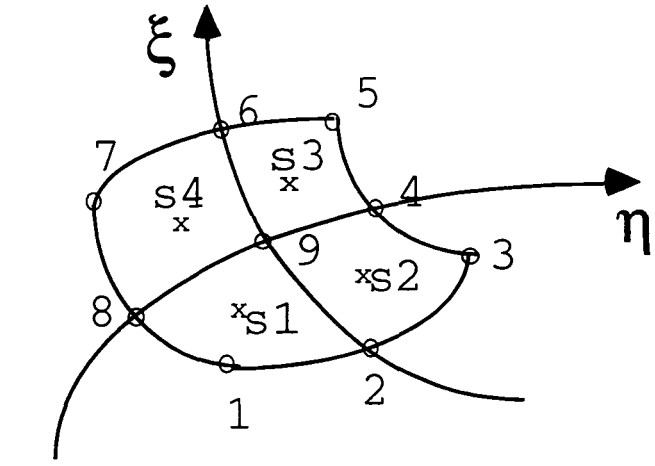

o Displacement Node

x Stress Node

(η , ξ) Nondimensional Element Coordinates

ELASTIC CONSTITUTIVE EQUATION

The stress strain relation used to model the composite shell is given below. The shell's inplane stresses are N_s, N_q and N_{sq}, moments are M_s, M_q and M_{sq}; and transverse shear forces are Q_s and Q_q. The shell's inplane strains are ε_s, ε_θ and $2\varepsilon_{s\theta}$; curvatures and twist are κ_s, κ_θ and $\kappa_{s\theta}$; and transverse shear strains are $2\varepsilon_{s3}$ and $2\varepsilon_{\theta 3}$.

$$\begin{Bmatrix} N_s \\ N_q \\ N_{sq} \\ M_s \\ M_q \\ M_{sq} \\ Q_s \\ Q_q \end{Bmatrix} = \begin{bmatrix} c_{11} & c_{12} & c_{16} & f_{11} & f_{12} & f_{16} & 0 & 0 \\ & c_{22} & c_{26} & f_{12} & f_{22} & f_{26} & 0 & 0 \\ & & c_{66} & f_{16} & f_{26} & f_{66} & 0 & 0 \\ & & & d_{11} & d_{12} & d_{16} & 0 & 0 \\ & & & & d_{22} & d_{26} & 0 & 0 \\ & \text{SYM} & & & & d_{66} & 0 & 0 \\ & & & & & & c_{55} & c_{45} \\ & & & & & & & c_{44} \end{bmatrix} \begin{Bmatrix} \varepsilon_s \\ \varepsilon_\theta \\ 2\varepsilon_{s\theta} \\ \kappa_s \\ \kappa_\theta \\ \kappa_{s\theta} \\ 2\varepsilon_{s3} \\ 2\varepsilon_{\theta 3} \end{Bmatrix}$$

We abbreviate the constitutive matrix as follows:

$$\begin{Bmatrix} N \\ M \\ Q \end{Bmatrix} = \begin{bmatrix} c & f & 0 \\ f^{\mathrm{T}} & d & 0 \\ 0 & 0 & c_\gamma \end{bmatrix} \begin{Bmatrix} \varepsilon \\ \kappa \\ \gamma \end{Bmatrix}$$

where,

$$\begin{Bmatrix} \varepsilon \\ \kappa \\ \gamma \end{Bmatrix} = \text{the Sanders-Budiansky nonlinear strains}^{5,6}.$$

PLATE ELEMENT STRAINS AS INTERNAL VARIABLES

Johnson, et al[7-14] recently demonstrated that the three - dimensional strain dependent viscoelastic stresses measured in rubberlike materials can be modeled using either time dependent reference shapes (an internal solid theory) or an auxiliary set of time dependent strain variables (a kinematic variable theory.) Here, we follow the second method mentioned above. A set of internal strain variables and a constitutive relation are introduced to specify the magnitude of the viscous stresses. The continuous time dependent deformation of the solid is approximated by discrete strain steps in time. A step strain relaxation finite difference equation then drives the internal strain variables magnitudes at each discrete step of the physical system and also partially relaxes the internal strain variables between the discrete steps.

Under the assumption of time - strain separability the viscoelastic stresses in the shell element at any time can be written as follows:

$$\begin{Bmatrix} N(t) \\ M(t) \\ Q(t) \end{Bmatrix} = \begin{bmatrix} c & f & 0 \\ f^{T} & d & 0 \\ 0 & 0 & c_{\gamma} \end{bmatrix} \begin{Bmatrix} \varepsilon(t) \\ \kappa(t) \\ \gamma(t) \end{Bmatrix} + \begin{Bmatrix} N^{*}(t) \\ M^{*}(t) \\ Q^{*}(t) \end{Bmatrix}$$

where $N^{*}(t)$, $M^{*}(t)$ and $Q^{*}(t)$ are the viscous components of $N(t)$, $M(t)$ and $Q(t)$ respectively. It is assumed that the constitutive model for the viscous stresses is given by:

$$\begin{Bmatrix} N^{*}(t) \\ M^{*}(t) \\ Q^{*}(t) \end{Bmatrix} = \begin{bmatrix} c^{*} & f^{*} & 0 \\ f^{*T} & d^{*} & 0 \\ 0 & 0 & c_{\gamma}^{*} \end{bmatrix} \begin{Bmatrix} \varepsilon^{*}(t) \\ \kappa^{*}(t) \\ \gamma^{*}(t) \end{Bmatrix}$$

where $\varepsilon^{*}(t)$, $\kappa^{*}(t)$ and $\gamma^{*}(t)$ are internal kinematic variables (i.e., they are strain measures not stress measures.) The components in the constitutive matrix are assumed to be constants.

KINEMATIC EXCITATION OF THE INTERNAL VARIABLES

During a general time dependent deformation of a solid the stresses measured in any given strain state will be different than the long term (relaxed) stresses in that strain state. Molecular theories of viscoelasticity (see Ref. 15) use a measure of the solid's deformation per unit time to drive the internal variables during an increment in strain. The internal variables such as molecular entropy and molecule length are then relaxed during the time between strain steps. This technique (see also Ref. 12) is applied to the shell's internal variables as follows:

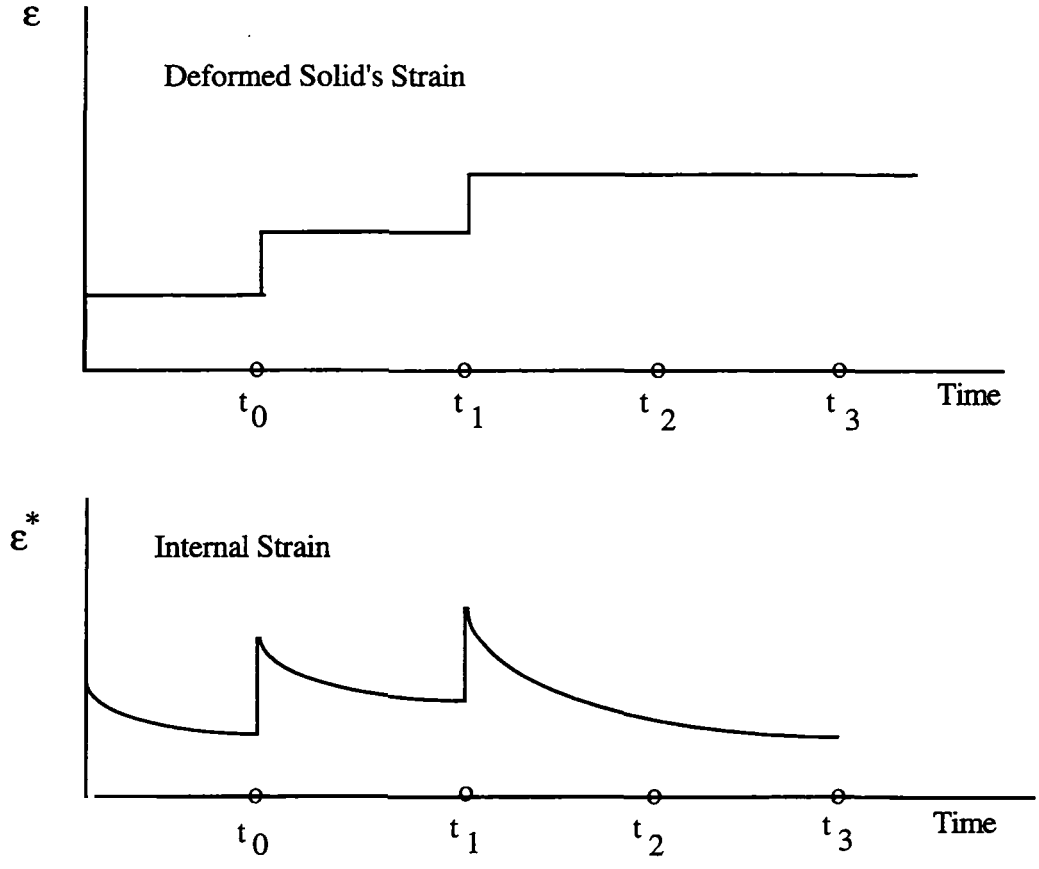

The finite difference update equation used to drive and define the internal variables is

$$\varepsilon^{*}_{j+1} = \left[\varepsilon^{*}_{j} + \left(\varepsilon_{j-1} - \varepsilon_{j}\right)\right] e^{-\Delta t / \tau}$$

The relaxation factor, τ, is selected by fitting the constitutive model to step-strain relaxation data. This is an explicit update and results in an implementation with minimal changes to the finite element code. It does, however, require the use of small time steps (and several executions at different time step sizes) to maintain accuracy.

EQUILIBRIUM EQUATIONS

In this model the viscous stresses due to the internal (state) variables at any given time are converted to applied forces at the displacement nodes. The finite element equilibrium equations are then modified by changing the load vector. The total stress at any time within the shell element is the sum of the elastic and viscous stresses. Equilibrium is then achieved between the stresses and the loads due to applied pressure, supports, and contact.

Using the notation of Noor, et al[1-4] and the equations introduced above, one has at any time, t, the viscous stresses at the stress nodes given by:

$$\left\{ h^* \right\} = \left[c^* \right] \left\{ e^* \right\}$$

These stresses are converted to forces $\left\{ f^* \right\}$ at the displacement nodes using the interpolation functions. Again, using the notation of Noor, et al the following expression results:

$$\left\{ f^* \right\} = \left[s_\ell \right]^{\mathrm{T}} \left\{ h^* \right\}$$

where $\left[s_\ell \right]^{\mathrm{T}}$ = the linear strain displacement matrix. The nonlinear force contributions due to the viscous stresses undergoing large displacements is not computed in this effort.

The Newton-Raphson equations used to find equilibrium are modified by subtracting $\left\{ f^* \right\}$ from the gradient vector determined in the Taylor expansion of the equilibrium equations. It becomes:

$$\begin{bmatrix} -\mathrm{f}_\ell & \mathrm{s}_\ell + m_{n\ell} & 0 \\ \left[\mathrm{s}_\ell + m_{n\ell} \right]^{\mathrm{T}} & 0 & q_C \\ 0 & q_C^{\mathrm{T}} & \dfrac{r_C}{\varepsilon} \end{bmatrix} \begin{Bmatrix} \Delta h \\ \Delta x \\ \Delta \lambda \end{Bmatrix} = \begin{Bmatrix} rh \\ rx - f^* \\ r\lambda \end{Bmatrix}$$

where f_ℓ = the linear flexibility matrix, $m_{n\ell}$ = the nonlinear strain displacement matrix, q_C = a matrix associated with contact, r_C = a matrix for regularization of the functional for contact, ε = a penalty parameter, Δh, Δx, $\Delta \lambda$ = stress resultants, nodal displacements, and Lagrange (contact) multipliers, rh, rx, $r\lambda$ = gradient expressions from the Taylor expansion of the equilibrium equations.

SIMULATION OF RELAXATION AND HYSTERESIS

The NASA tire footprint finite element code was modified to implement the model described above†. Since experimental data was not available to calibrate the viscous material law a number of trial simulations were made with different relaxation times, τ, and with different constitutive matrices, $\left[c^* \right]$, to determine sample values for use in a computational simulation. We used $\tau = 1.0\ sec$ for the relaxation of the internal variables, and $\left[c^* \right] = [c]$. The viscous moduli were assumed equal to the elastic moduli since the internal variable update relation is explicit in time. Recall:

$$\varepsilon^*_{j+1} = \left[\varepsilon^*_j + \left(\varepsilon_{j-1} - \varepsilon_j \right) \right] e^{-\Delta t / \tau}$$

A number of trial computer executions were used to determine an appropriate time step size. That is, a numerically determined time step, small enough for convergence, was used; namely $\Delta t = 0.0625\ sec$.

In the first simulation the rim displacement was ramped to 1.2 in. over a time of 5.0 sec. The displacement was held constant. The computed force-time curve is shown below. Both the total stress (viscous) and the elastic (static) stress are shown.

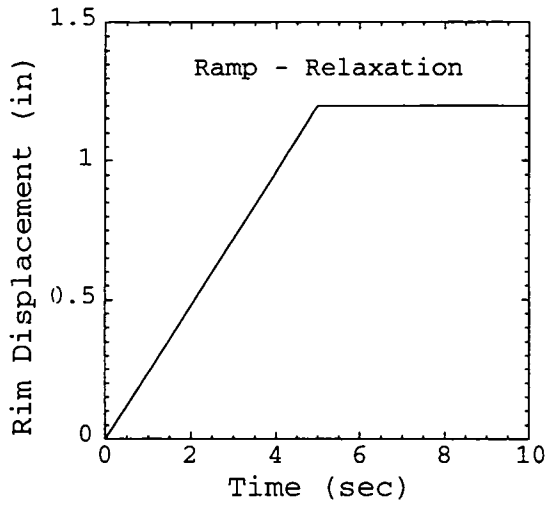

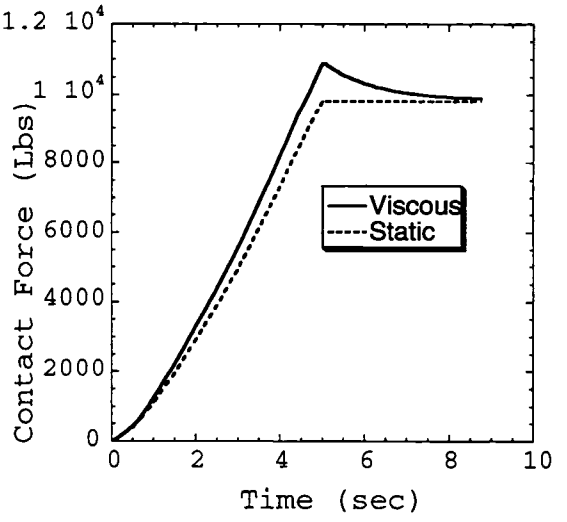

† The authors wish to thank Ms. Jeanne M. Peters of the Center for Computational Structures Technology, University of Virginia, NASA Langley Research Center for her assistance in making the necessary changes to the finite element code.

SIMULATION OF RELAXATION AND HYSTERESIS (Continued)

The second simulation consisted of forcing the tire rim from 0.0 in. to 1.2 in. over a period of 5.0 sec and then back to 0.0 in. during the next 5.0 sec. This simulation produced the hysteretic loop shown below. The load displacement curve for the static loading (without any viscoelasticity) is also shown.

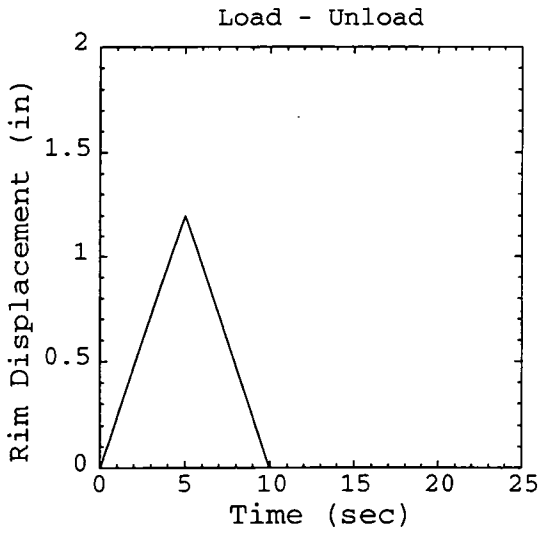

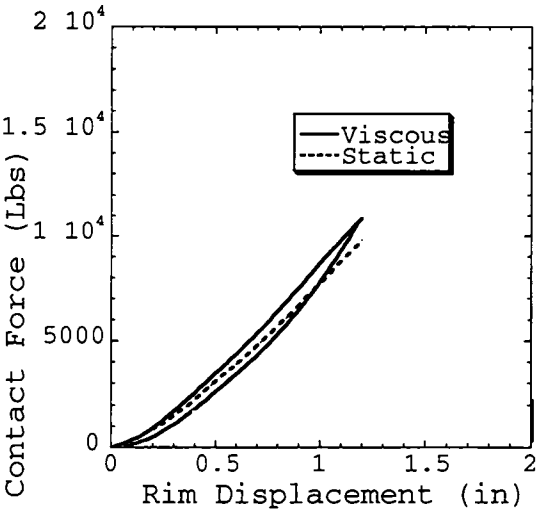

In the third simulation the same rim displacement rate was used, but the rim was displaced to 1.8 in. before it was unloaded. It was then displaced to 0.9 in. The total (viscous) and elastic (static) stresses are shown below.

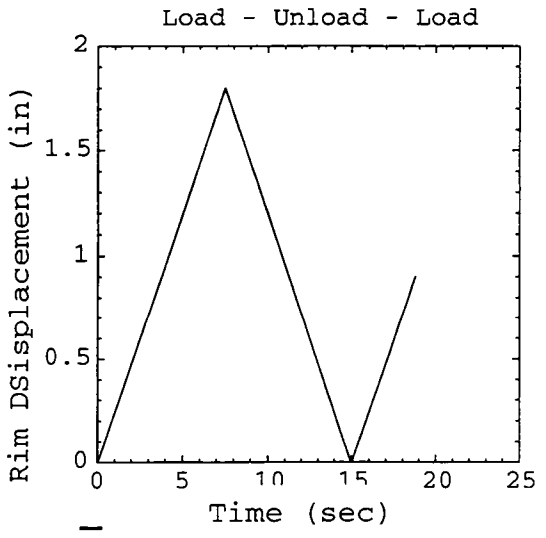

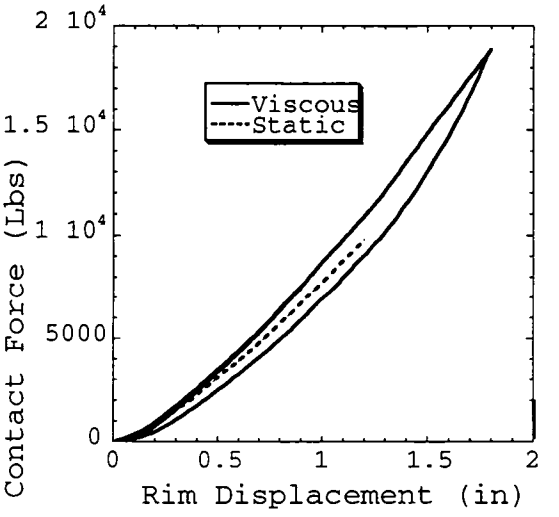

SIMULATION OF RELAXATION AND HYSTERESIS (Continued)

A detailed look at the Contact Force vs Rim Displacement graph shown below indicates that the contact force went to zero when the rim was "unloading". This is due to the fact that the "tire" did not have time to fully recover during the unloading. It separated from the contact surface. As is shown below, while the contact surface continued to drop and rise the tire recovered slightly and contact was made at a smaller rim displacement upon reloading.

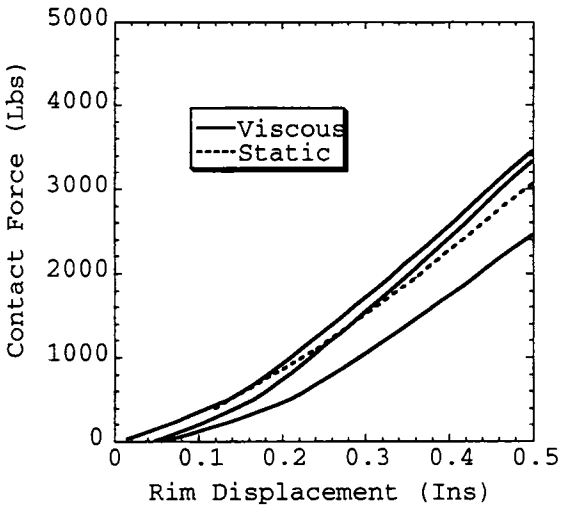

SUMMARY

A method was presented in which the mixed nonlinear shell element of Noor, et al[1,2] was used to simulate viscous deformations of a Space Shuttle nose gear tire during a vertical loading and unloading against a frictionless surface. The viscous constitutive model introduced is anisotropic and is defined by internal variables in one-to-one correspondence with the generalized coordinates used in the shell's constitutive model. The computational simulations were limited to a demonstration of the algorithm since experimental data was not available to calibrate the viscous model. The algorithm appears promising in that it can be modified to include more complicated time dependent material behavior than was demonstrated above. That is, additional internal variables can be introduced if several relaxation times are needed to model the material's behavior.

REFERENCES

1. Noor, A. K. and Hartley, Nonlinear Shell Analysis via Mixed Isoparametric Elements, Computers & Structures, Vol. 7, pp 615-626, 1977.

2. Noor, A. K., Anderson, C. M., and Tanner, J. A., Exploiting Symmetries in the Modeling and Analysis of Tires, NASA Technical Paper 2649, March 1987.

3. Kim, K. O., Tanner, J. A., Noor, A. K., and Robertson, M. P., Computational Methods for Frictionless Contact With Application to Space Shuttle Orbiter Nose-Gear Tires, NASA Technical Paper 3073, May 1991.

4. Tanner, J. A., Computational Methods for Frictional Contact with Application to the Space Shuttle Orbiter Nose-Gear Tire, PhD Dissertation, George Washington University, September 1992.

5. Sanders, J. L., Nonlinear Theories for Thin Shells, Q. Appl. Math., vol. 21, no. 1, pp 21-36, 1963.

6. Budiansky, B., Notes on Nonlinear Shell Theory, J. Appl. Mech., vol. 35, no. 2, pp 393-401, 1968.

7. Johnson, A. R., Quigley, C. J., Cavallaro, C. and Weight, K. D., A large deformation viscoelastic finite element model for elastomers, in The Mathematics of Finite Elements and Applications VII, Edited by J. R. Whiteman, Academic Press Limited, ISBN 0-12-747257-6, 1991.

8. Johnson, A. R., Quigley, C. J., Weight, K. D., Cavallaro, C. and Cox, D. L., Inflation and deflation of a thick walled viscohyperelastic sphere, in Transactions of the Eighth Army Conference on Applied Mathematics and Computing, U. S. Army Research Office Report No. 91-1, 847-857(1991).

9. Johnson, A. R. and Quigley, C. J., A viscohyperelastic Maxwell model for rubber viscoelasticity, Rubber Chemistry and Technology, **65**, 137-153(1992).

10. Johnson, A. R., Quigley, C. J. and Freese, C. E., Viscohyperelasticity, in Transactions of the Tenth Army Conference on Applied Mathematics and Computing, U. S. Army Research Office Report No. 93-1, 235-256(1993).

11. Johnson, A. R., Quigley, C. J., Young, D. G. and Danik, J. A., Viscohyperelastic modeling of rubber vulcanizates, Tire Science and Technology, TSTCA, **21**, No. 3, 179-199(1993).

12. Johnson, A. R. and Stacer, R. G., Rubber viscoelasticity using the physically constrained system's stretches as internal variables, Rubber Chemistry and Technology, **66**(4), 567-577(1993).

13. Johnson, A. R., Quigley, C. J. and Mead, J. L., Large Strain Viscoelastic Constitutive Models for Rubber. Part I: Formulations, accepted for publication, Rubber Chemistry and Technology, **67**, (1995).

14. Quigley, C. J., Mead, J. L. and Johnson, A. R., Large Strain Viscoelastic Constitutive Models for Rubber. Part II: Determination of Material Constants, accepted for publication, Rubber Chemistry and Technology, (1995).

15. Doi, M. and Edwards, S. F., The Theory of Polymer Dynamics, Oxford, New York, 1986.

The Mode I Mechanical Crack Tip Stress Field in Hyperelastic and Incompressible Materials

Claudia J. Quigley
U.S. Army Research Laboratory
Materials Directorate
Watertown, MA

THE MODE I MECHANICAL CRACK TIP STRESS FIELD IN HYPERELASTIC AND INCOMPRESSIBLE MATERIALS

Claudia J. Quigley
U.S. Army Research Laboratory
Materials Directorate
Watertown, MA

INTRODUCTION

The finite deformation field of a plane strain Mode I crack in a hyperelastic and incompressible material was examined under the assumptions of small scale nonlinearity. Finite element analyses were performed for two different material laws, a Neo-Hookean material and a third order invariant of a Rivlin material. The numerical results for both materials were compared to the appropriate theoretical asymptotic solution. A local cavitation locus surrounding the crack tip was identified for the Neo-Hookean material. For the third order invariant Rivlin material, maximum values of the dominant stress component were found close to the surface of the crack, above and below the deformed crack tip.

PROBLEM DESCRIPTION

Consider a thick infinite plate of hyperelastic and incompressible material, as shown in Figure 1, containing a stationary crack. The crack faces were traction free and a uniform uniaxial stress, τ, was applied at infinity. No body forces or thermal forces were present. The stresses and deformation field in a small circular region encompassing the crack tip were examined to determine the size and the shape of the nonlinear crack tip region. Crack tip field quantities were compared to the theoretical asymptotic solution for this problem.

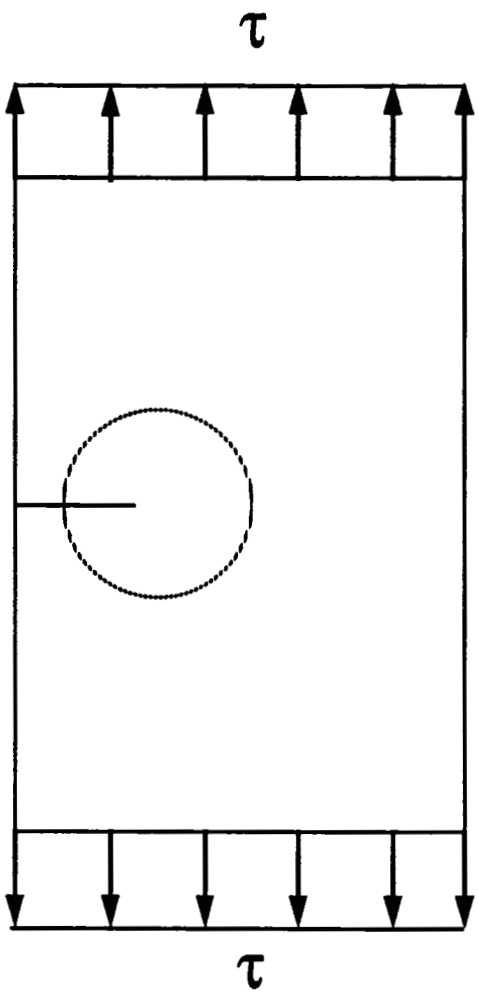

Figure 1. A crack in a thick, infinite plate of hyperelastic and incompressible material.

APPROACH: SMALL SCALE NONLINEARITY

The approach taken for this problem was that of small scale nonlinearity[1], which is analogous to small scale yielding. Referring to Figure 2, consider our circular region of radius, R. The crack length within this region is also of length, R. Under small scale nonlinearity, the applied load is sufficiently small to confine the crack tip field to a small region surrounding the crack tip, compared to the crack length and the overall geometry of the body. Three separate regions of material behavior can be identified. Far from the crack tip, small geometry changes are present, and material behavior approaches linear elasticity. Here, the linear elastic Mode I asymptotic solution was present. The linear elastic region encloses a smaller, second region, where material behavior transitions from linear elastic to nonlinear elastic. This second region encompasses a third, smaller region, where finite deformations and large deformations are present, indicative of nonlinear elastic material behavior. The nonlinear asymptotic solution is dominant in this region.

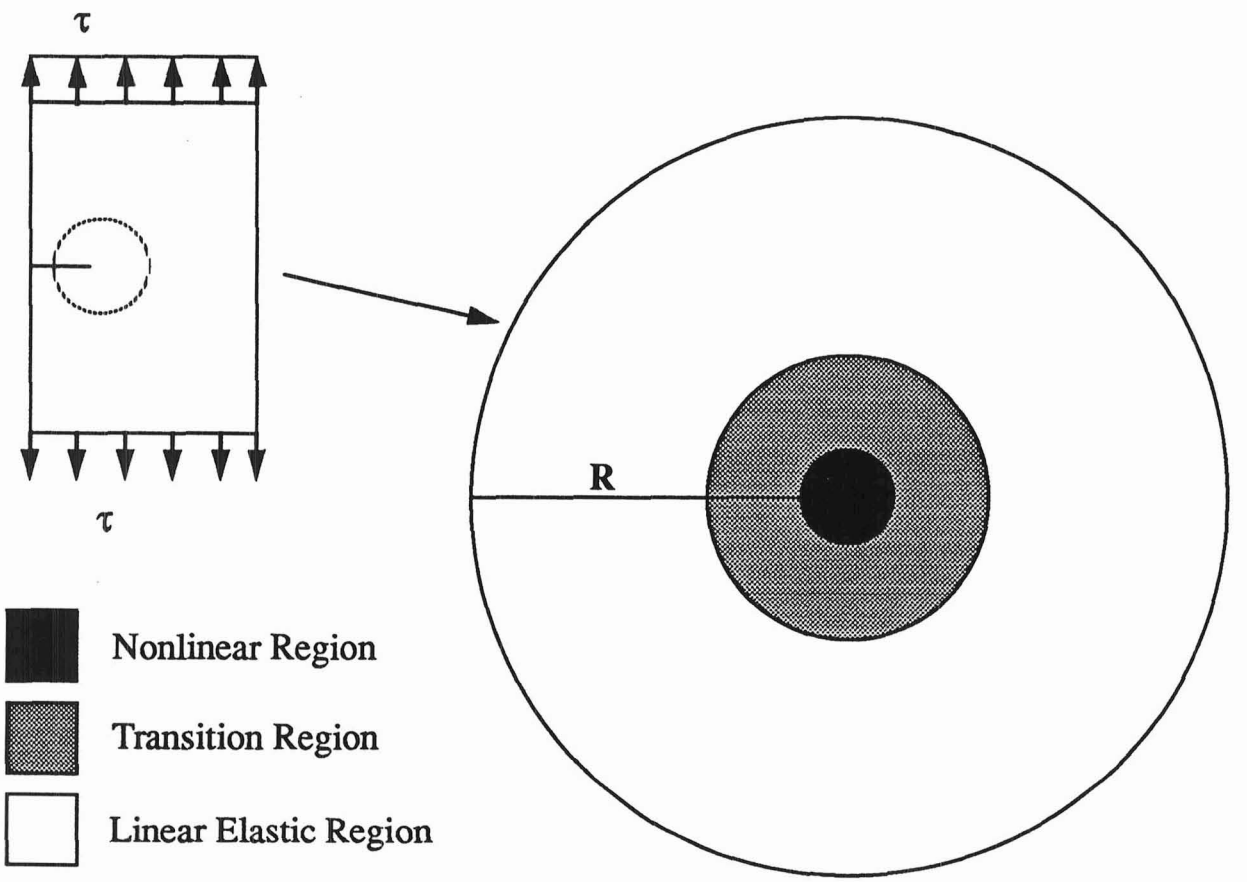

Figure 2. Small scale nonlinearity.

ASSUMPTIONS OF SMALL SCALE NONLINEARITY

Under small scale nonlinearity, the J-integral[2] is assumed to be path independent around any suitable contour, Γ, which surrounds the crack tip, as shown in Figure 3. The J-integral can be expressed as

$$J = \int_{\Gamma} (W n_1 - s_i u_{i,1})\, dS$$

where W represents the strain energy, n_1 is the unit normal in the x_1 direction, s_i is the nominal traction vector, and u_i is the displacement vector. Here, dS is an element of arc length along Γ. The J-integral is also assumed to be equivalent to the energy release rate, so that the value of the J-integral is a direct function of the applied stress intensity factor, K_I.

$$J = K_I^2 \frac{(1-\upsilon)}{2\mu}$$

Here, μ is the shear modulus, and the Poisson ratio, υ, equals 1/2 due to incompressibility.

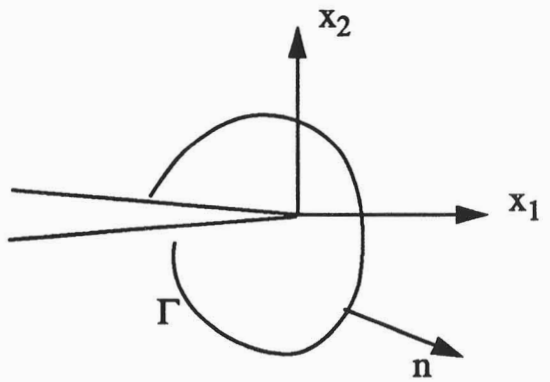

Figure 3. Evaluation of the J-integral around a suitable contour.

BOUNDARY CONDITIONS

Due to reflective symmetry about the x_1 axis, only the top half of the circular plate was modelled. Consistent with small scale nonlinearity, the Mode I linear elastic solution was applied as consistent nodal point forces along the outer radius, R, see Figure 4. The linear elastic solution[3] is given as

$$\sigma_{11} = \frac{K_I}{\sqrt{2\pi r}} \cos\frac{\theta}{2}\left(1 - \sin\frac{\theta}{2}\sin\frac{3\theta}{2}\right) + o\left(r^{1/2}\right)$$

$$\sigma_{22} = \frac{K_I}{\sqrt{2\pi r}} \cos\frac{\theta}{2}\left(1 + \sin\frac{\theta}{2}\sin\frac{3\theta}{2}\right) + o\left(r^{1/2}\right)$$

$$\sigma_{12} = \frac{K_I}{\sqrt{2\pi r}} \cos\frac{\theta}{2}\cos\frac{3\theta}{2}\sin\frac{\theta}{2} + o\left(r^{1/2}\right)$$

in terms of the undeformed polar coordinate system (r,θ).At sufficiently small loads, the linear elastic solution is found throughout the entire crack tip region. However, as the magnitude of K_I is increased, the nonlinear crack tip field began to evolve at the crack tip and grew in size and extent. It is the stresses and deformations in the nonlinear crack tip region that will be examined next.

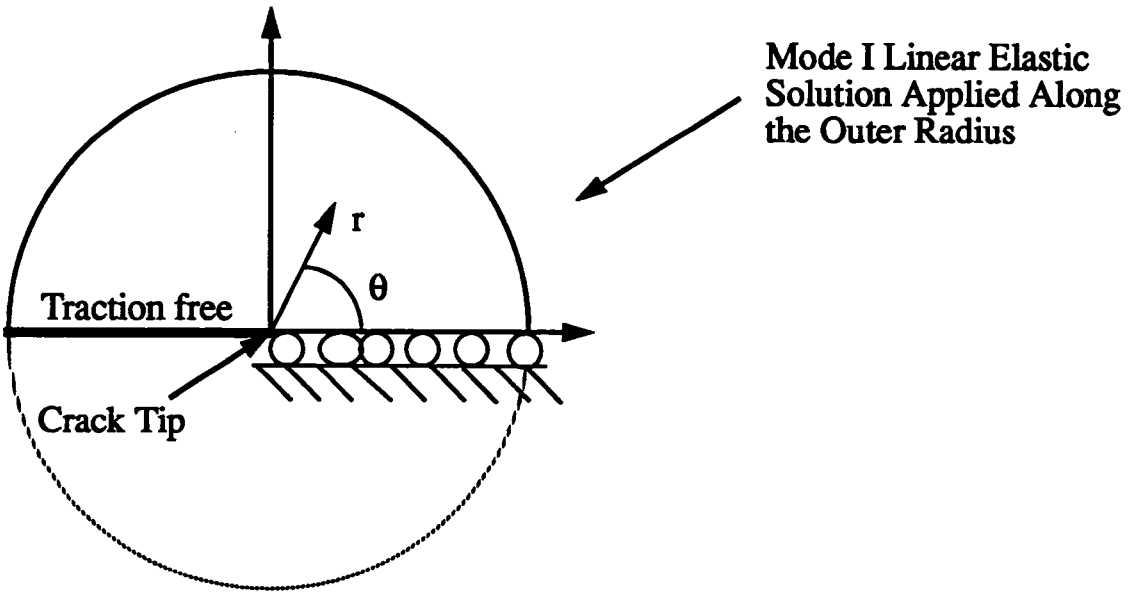

Figure 4. Boundary conditions applied along the outer radius, R.

FINITE ELEMENT MODEL

The finite element mesh[4] was designed to sustain very large deformations at the crack tip, so that the nonlinear region could sufficiently expand to a size at which the nonlinear crack tip field quantities could be compared to the theoretical asymptotic solution. At these large deformations, numerical mapping methods begin to break down, and the elements begin to evert, making the nonlinear crack tip field difficult to resolve. Consequently, the finite element mesh, Figure 5, was composed of two regions, a coarse mesh in the immediate vicinity of the crack tip, encompassed by a refined mesh, where accurate field quantities could be found.

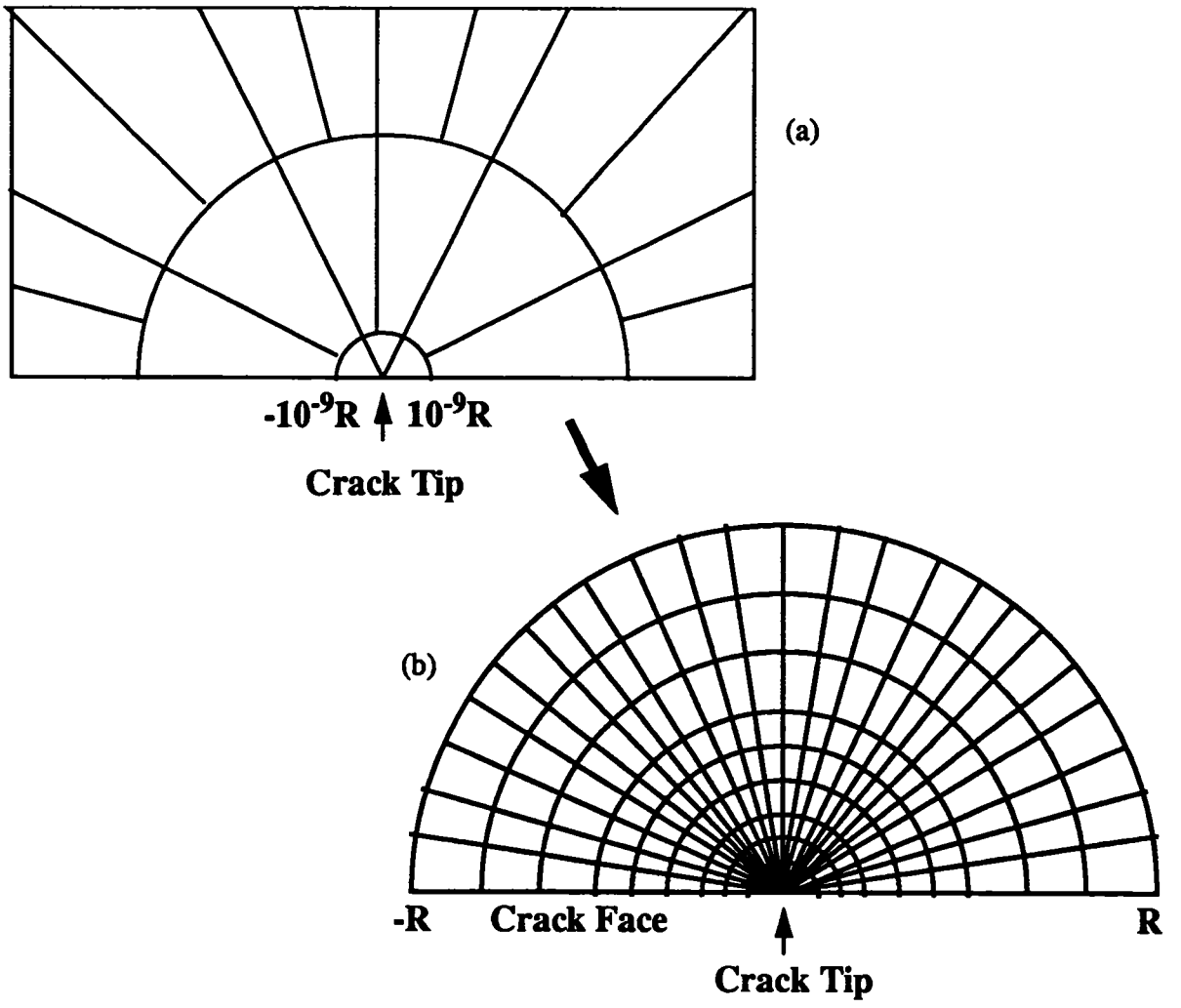

Figure 5. The finite element model. The coarse mesh in (a) is enclosed by the refined mesh in (b).

THE NONLINEAR ASYMPTOTIC SOLUTION FOR THE NEO-HOOKEAN MATERIAL

For the first finite element analysis, a Neo-Hookean constitutive law was chosen. For this material law, the strain energy is expressed as:

$$W = \frac{\mu}{2}(I-3)$$

where the principal strain invariant, I, is a function of the stretch ratios, λ_i,

$$I = \lambda_1^2 + \lambda_2^2 + \lambda_3^2$$

Under the assumptions of small scale nonlinearity, the Mode I nonlinear asymptotic solution[5] for this material is:

$$y_1 \sim br\sin^2\frac{\theta}{2} + \frac{1}{a}r^{3/2}\left(2\cos\frac{\theta}{2} - \frac{2}{3}\cos\frac{3\theta}{2}\right)$$

$$y_2 \sim ar^{1/2}\sin\frac{\theta}{2} + r^{3/2}\left(d\sin\frac{3\theta}{2} - \frac{b^2}{2a}\sin\frac{\theta}{2}\right)$$

$$\tau_{22} \sim \frac{\mu}{4}a^2 r^{-1}$$

$$\tau_{11} \sim \frac{\mu}{2}b^2(1-\cos\theta)$$

$$\tau_{12} \sim \frac{\mu}{2}abr^{-1/2}\sin\frac{\theta}{2}$$

where a, b, and d are load parameters. The deformation field is given by y_i, and the Cauchy stresses are represented as τ_{ij}. Substituting this asymptotic solution into the definition of the J-integral permits a direct solution for the load amplitude parameter, a, in terms of K_I.

$$a = \frac{K_I}{\mu\sqrt{\pi}}$$

From the finite element analysis, the remaining two load parameters were found.

$$b \sim -1.6 \qquad \text{when } J_{applied} = 0.065 \text{ MPa-m}$$

$$d \sim 1.1\frac{\mu}{K_I}$$

RESULTS FOR THE NEO-HOOKEAN MATERIAL

The graph below is a normalized plot of τ_{22} as a function of undeformed radial distance from the crack tip. These results were taken at an angle of 71.25 degrees. Far from the crack tip, at large values of r, the linear elastic asymptotic solution is found. As the crack tip was approached, the finite element results transition to the nonlinear elastic solution for this problem. Figure 6 is only one example in which the presence of the nonlinear elastic solution was verified. To see additional results, the reader is referred to reference 4.

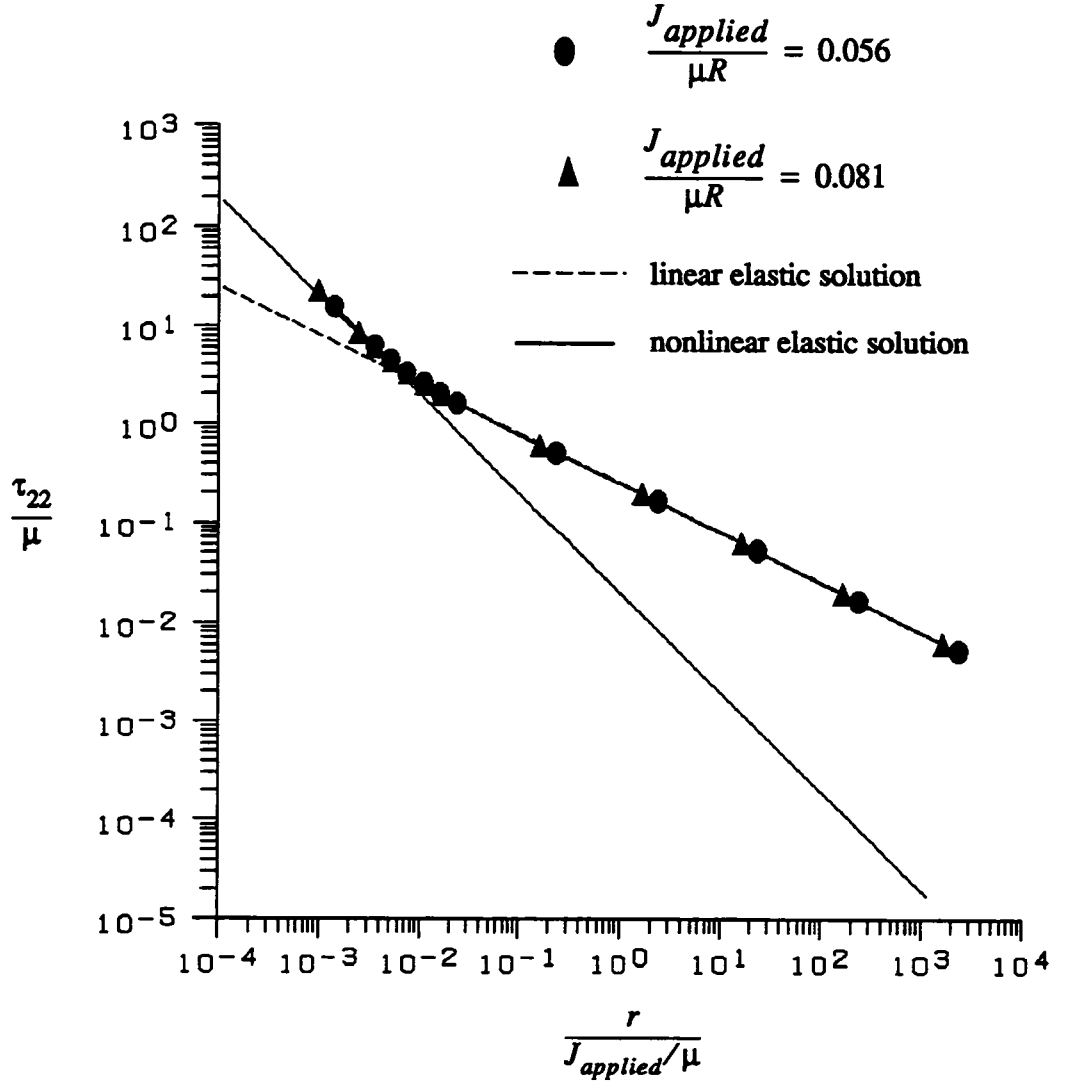

Figure 6. Logarithmic plot of τ_{22} as a function of radial distance at $\theta = 71.25$ degrees.

FAILURE MECHANISM

A potential failure mechanism in this material is cavitation of a pre-existing microvoid. For a Mode I crack, representative of a nonhydrostatic load condition, a cavitation criteria[6] has been expressed in terms of the principal Cauchy stresses, τ_i, as

$$(4\tau_3 - \tau_1 - \tau_2)\,((4\tau_2 - \tau_1 - \tau_3))\,(4\tau_1 - \tau_2 - \tau_3) - 125\mu^3 = 0$$

This criterion can be applied to the mechanical crack tip stress field to determine a surface surrounding the crack tip where cavitation is likely to occur. This region is outlined by the dashed line in Figure 7. Within this region, assuming that void nucleation occurs, the size and shape of several cavitated voids at arbitrarily selected material points were determined by the deformation gradient. The voids elongate in the direction of the applied loads and are close to the surface of the crack.

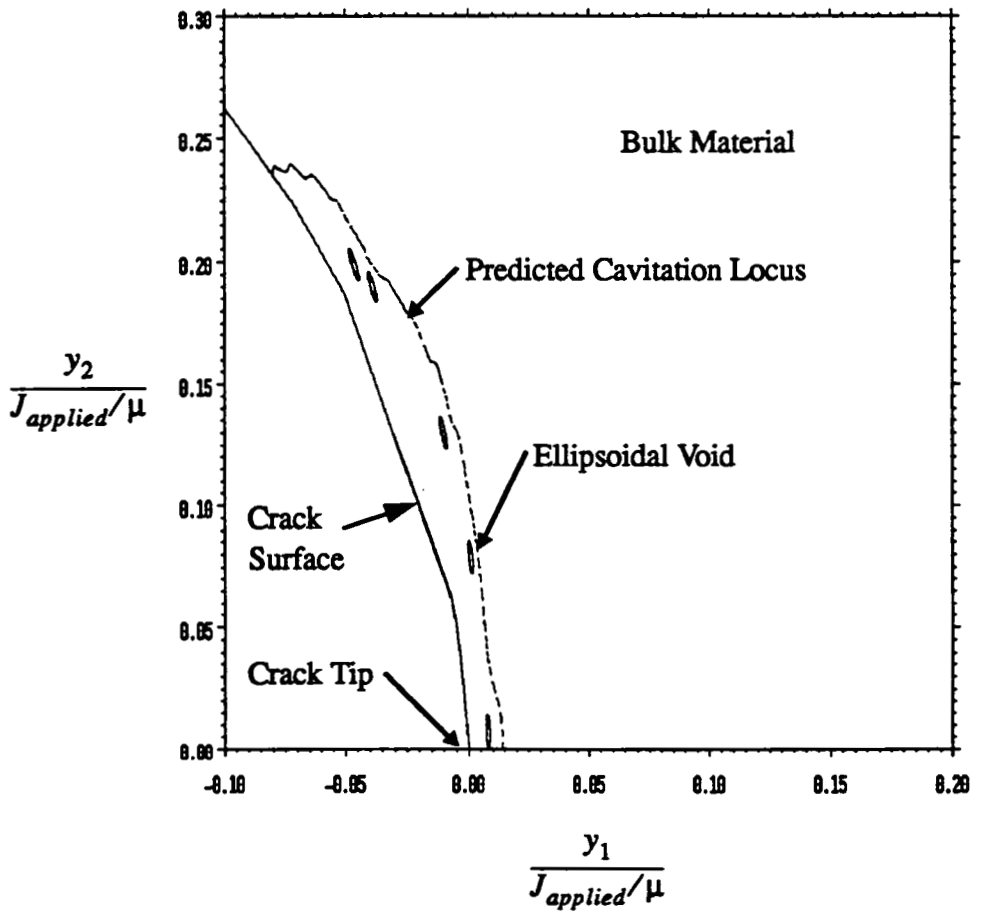

Figure 7. A cavitation locus surrounding the deformed crack tip.

THE NONLINEAR ASYMPTOTIC SOLUTION FOR THE THIRD ORDER INVARIANT MATERIAL

A second finite element analysis was completed using the third order invariant of the Rivlin constitutive model. Noting that I_1 and I_2 are equal in plane strain, this material model can be expressed in terms of a single strain invariant, I, as

$$W = (C_{10}+C_{01})(I-3) + (C_{20}+C_{02}+C_{11})(I-3)^2 + (C_{30}+C_{03}+C_{21}+C_{12})(I-3)^3$$

where C_{ij} are the material constants. The nonlinear asymptotic solution[7], under the assumptions of small scale nonlinearity, for this material model has been derived as

$$y_1 \sim \frac{-324\sqrt{3}}{25}\frac{r^{7/6}}{a}(\omega(\theta)+\frac{2}{3}\cos\theta)^{7/6} \times (\frac{5}{7}F(\frac{-7}{10};\frac{1}{2};\frac{3}{10};\cos^2\varepsilon_o) - \frac{2}{3}\cos\theta)$$

$$y_2 \sim ar^{5/6}\sin\frac{\theta}{2}\left(\frac{1-\frac{8}{9}\cos^2\frac{\theta}{2}}{1+\omega(\theta)}\right)^{1/2}(\omega(\theta)+\frac{2}{3}\cos\theta)^{1/3} - \frac{3\sqrt{6}}{50}\frac{B}{A}r^{7/6}(\omega(\theta)+\frac{2}{3}\cos\theta)^{1/6}(1+\frac{2}{3}\sin^2\theta-\omega(\theta)\cos\theta)^{1/2}$$

$$\tau_{11} \sim o(r^{-2/3})$$

$$\tau_{22} \sim r^{-1}(\frac{2}{9}A)(\frac{5}{6}a)^6(\omega(\theta)+\frac{2}{3}\cos\theta)^{-1}$$

$$\tau_{12} \sim r^{-2/3}T_{12}(\theta) + o(r^{-2/3})$$

where

$$\omega(\theta) = \frac{1}{3}[9-4\sin^2\theta]^{1/2}$$

THE NONLINEAR ASYMPTOTIC SOLUTION FOR THE THIRD ORDER INVARIANT MATERIAL (CONTINUED)

$$\cos\varepsilon_o = \frac{\left(1+\frac{2}{3}\sin^2\theta-\omega(\theta)\cos\theta\right)^{1/2}}{3\sqrt{2}\left(\omega(\theta)+\frac{2}{3}\cos\theta\right)}$$

$$A = C_{21}+C_{12}+C_{30}+C_{03} \qquad B = C_{11}+C_{20}+C_{02}-9A$$

and F[...] and $T_{12}(\theta)$ are hypergeometric functions. The sole load amplitude parameter, a, can again be determined by substituting the nonlinear asymptotic solution into the definition of the J-integral, yielding

$$a = \left(\frac{3\left(\frac{6}{5}\right)^5 K_I^2}{4\pi\mu A}\right)^{1/6}$$

This asymptotic solution is remarkably different from that of the linear asymptotic solution and the nonlinear asymptotic solution for the Neo-Hookean material. The dominant stress, τ_{22}, is of $o(r^{-1})$, but is inversely proportional to a function of θ. Both terms in the deformation field, y_1 and y_2, possess multiple functions of θ.

RESULTS FOR THE THIRD ORDER INVARIANT MATERIAL

The finite element results will now be compared to the nonlinear asymptotic solution for this material. Circumferential plots for the y_2 - deformation component and the τ_{22} stress component surrounding the crack tip were examined in the refined mesh region, close to the crack tip. Again, the normalized results were given in reference to the undeformed coordinate system. Close agreement was found between the finite element results and the theoretical solution for this problem, as shown in Figures 8 and 9.

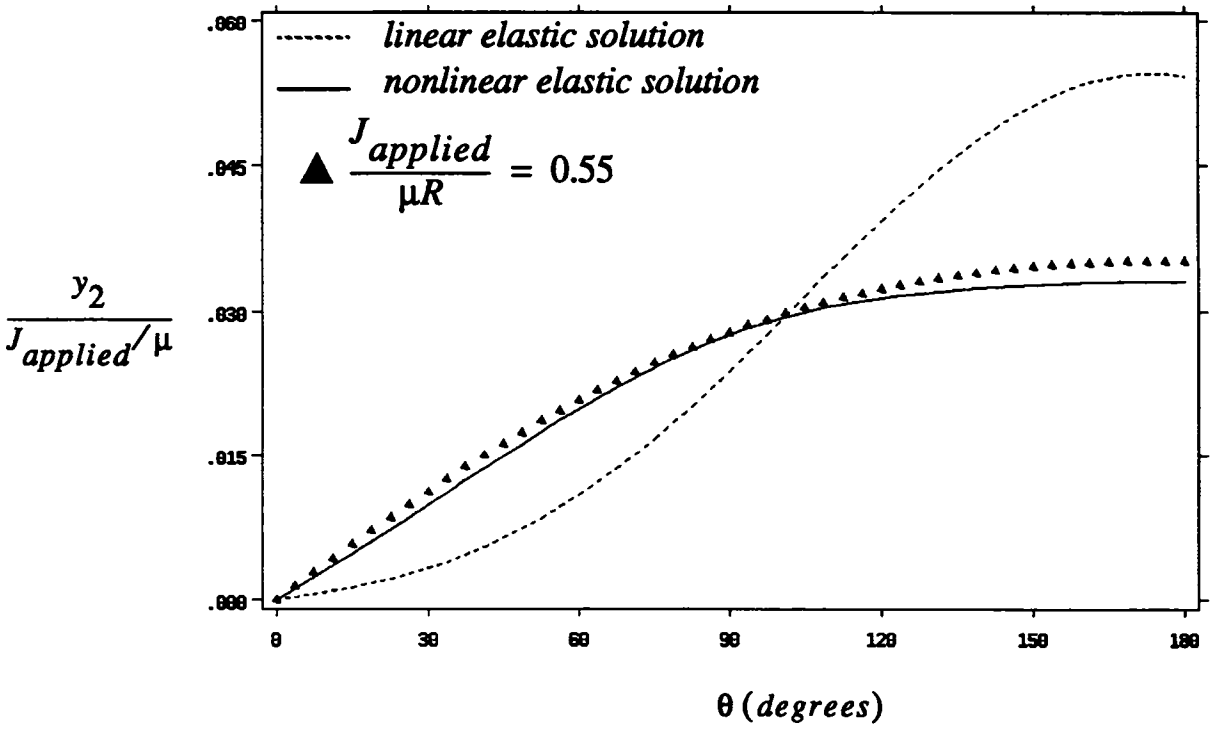

Figure 8. Circumferential plot of y_2 taken along a radius of 4.6E-3 $J_{applied}/\mu$.

RESULTS FOR THE THIRD ORDER INVARIANT MATERIAL (CONTINUED)

The circumferential plot of τ_{22}, as a function of θ, confirms the presence of the nonlinear asymptotic solution. A comparison of the finite element results to the linear elastic solution reveals some significant differences. In the linear elastic solution, the τ_{22} stress component is higher in magnitude directly in front of the crack tip, when θ is less than ninety degrees in the undeformed configuration. However for the nonlinear crack tip field, maximum values of τ_{22} were found as θ approached 180 degrees in the undeformed configuration, close to the crack surface. Assuming that failure would occur at locations of maximum stress, these results suggest that material failure and secondary crack growth should initiate close to the crack surface, which is above and below the crack tip in the deformed configuration. The results were consistent with experimental observations on tearing in carbon black filled elastomers[8].

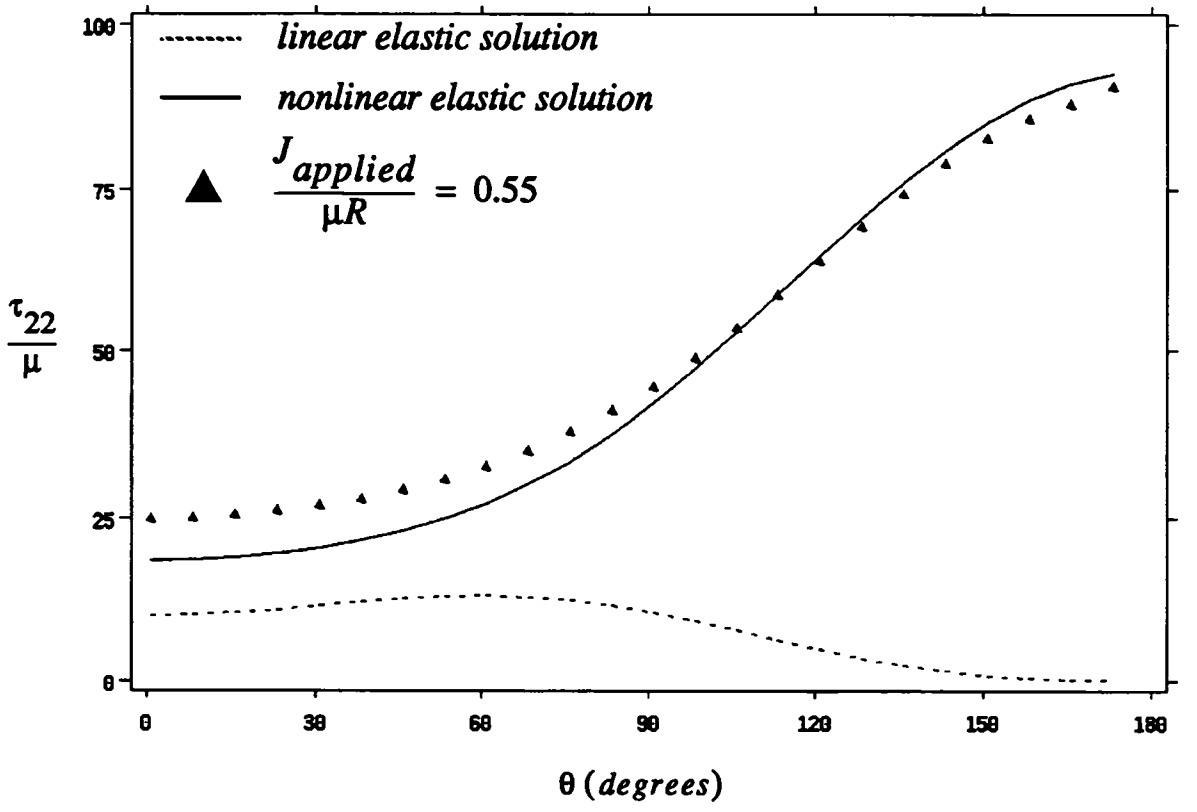

Figure 9. Circumferential plot of τ_{22} taken along a radius of 5.5E-3 $J_{applied}/\mu$.

CONCLUSIONS

A finite element analysis of a plane strain Mode I crack was performed for two different materials, a NeoHookean material and the third order invariant of the Rivlin constitutive law, under the assumptions of small scale nonlinearity. The numerical results for both materials confirmed the presence of the appropriate theoretical nonlinear asymptotic solution in a small region surrounding the crack tip. For the Neo-Hookean material, a potential cavitation locus encompassing the crack tip was identified. Within this cavitation region, possible sizes and orientation of nucleated microvoids were suggested. For the higher order material, localized material failure was predicted close to the crack surface, above and below the deformed crack tip, where the τ_{22} stress component reached maximum values.

REFERENCES

1. J.W. Hutchinson, Nonlinear Fracture Mechanics, The Technical University of Denmark, 1979.

2. J.R. Rice, A path-independent integral and the approximate analysis of strain concentrations by notches and cracks, Journal of Applied Mechanics, 35, 379 - 386, 1968.

3. M.L. Williams, On the stress distribution at the base of a stationary crack, Journal of Applied Mechanics, 24, 109 - 114, 1957.

4. C.J. Quigley and D.M. Parks, The finite deformation field surrounding a mode I plane strain crack in a hyperelastic incompressible material under small-scale nonlinearity, International Journal of Fracture, 65, 75 - 96, 1994.

5. J.K. Knowles, Finite elastostatic fields with unbounded deformation gradients, in Finite Elasticity, AMD - Vol. 27, 23 - 40, 1977.

6. H. Hou and R. Abeyaratne, Cavitation in elastic and elastic-plastic solids, Journal of the Mechanics and Physics of Solids, 40, 571 - 592, 1992.

7. R. Stephenson, The equilibrium field near the tip of a crack for finite plane strain of incompressible elastic materials, Journal of Elasticity, 12, 65 - 99, 1982.

8. C.J. Quigley, R. Dooley, and D.M. Parks, An experimental study of failure in circumferentially notched elastomer cylinders, Rubber Chemistry and Technology, 60, 646 - 663, 1993.

Advances in Reduction Techniques for Tire Contact Problems

Ahmed K. Noor
Center for Computational Structures Technology
University of Virginia
Hampton, VA

ADVANCES IN REDUCTION TECHNIQUES FOR TIRE CONTACT PROBLEMS

Ahmed K. Noor
Center for Computational Structures Technology
University of Virginia
NASA Langley Research Center
Hampton, VA

INTRODUCTION

Some recent developments in reduction techniques, as applied to predicting the tire contact response and evaluating the sensitivity coefficients of the different response quantities, are reviewed. The sensitivity coefficients measure the sensitivity of the contact response to variations in the geometric and material parameters of the tire. The tire is modeled using a two-dimensional laminated anisotropic shell theory with the effects of variation in geometric and material parameters, transverse shear deformation, and geometric nonlinearities included. The contact conditions are incorporated into the formulation by using a perturbed Lagrangian approach with the fundamental unknowns consisting of the stress resultants, the generalized displacements, and the Lagrange multipliers associated with the contact conditions. The elemental arrays are obtained by using a modified two-field, mixed variational principle.

For the application of reduction techniques, the tire finite element model is partitioned into two regions. The first region consists of the nodes that are likely to come in contact with the pavement, and the second region includes all the remaining nodes. The reduction technique is used to significantly reduce the degrees of freedom in the second region.

The effectiveness of the computational procedure is demonstrated by a numerical example of the frictionless contact response of the space shuttle nose-gear tire, inflated and pressed against a rigid flat surface. Also, the research topics which have high potential for enhancing the effectiveness of reduction techniques are outlined.

OBJECTIVES AND SCOPE

Despite the significant advances made in the development of effective computational models and computational strategies for the numerical simulation of the nonlinear tire response (see, for example, Refs. 1, 2 and 3), the modeling of aircraft tire contact response with the pavement remains one of the challenging applications of computational structural mechanics. The objectives of this presentation are to (see Fig. 1): a) review some of the recent developments in reduction techniques as applied to the tire contact problem, and b) identify some of the future directions for research. The scope of the presentation covers both the frictionless contact response of tires as well as sensitivity analysis.

Objectives

- **Review some of the recent developments in reduction techniques as applied to the tire contact problem**
- **Identify some of the future directions for research**

Scope

- **Frictionless contact response of tires**
- **Sensitivity analysis**

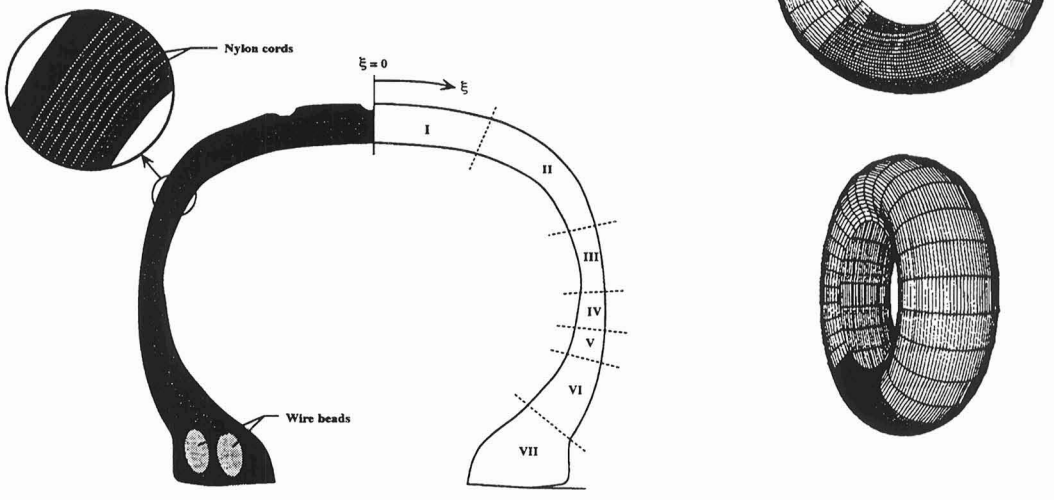

Figure 1.

FINITE ELEMENT MODELING
Two-Dimensional First-Order Shear Deformation Theory

The analytical formulation for frictionless contact of tires is based on a form of the nonlinear, moderate rotation, Sanders-Budiansky type shell theory (Refs. 4 and 5) with the effects of variations in the geometric and material parameters, anisotropic material response, and transverse shear deformation included. The fundamental unknowns consist of the stress resultants, the generalized displacements, and the Lagrange multipliers associated with the contact conditions (see Fig. 2).

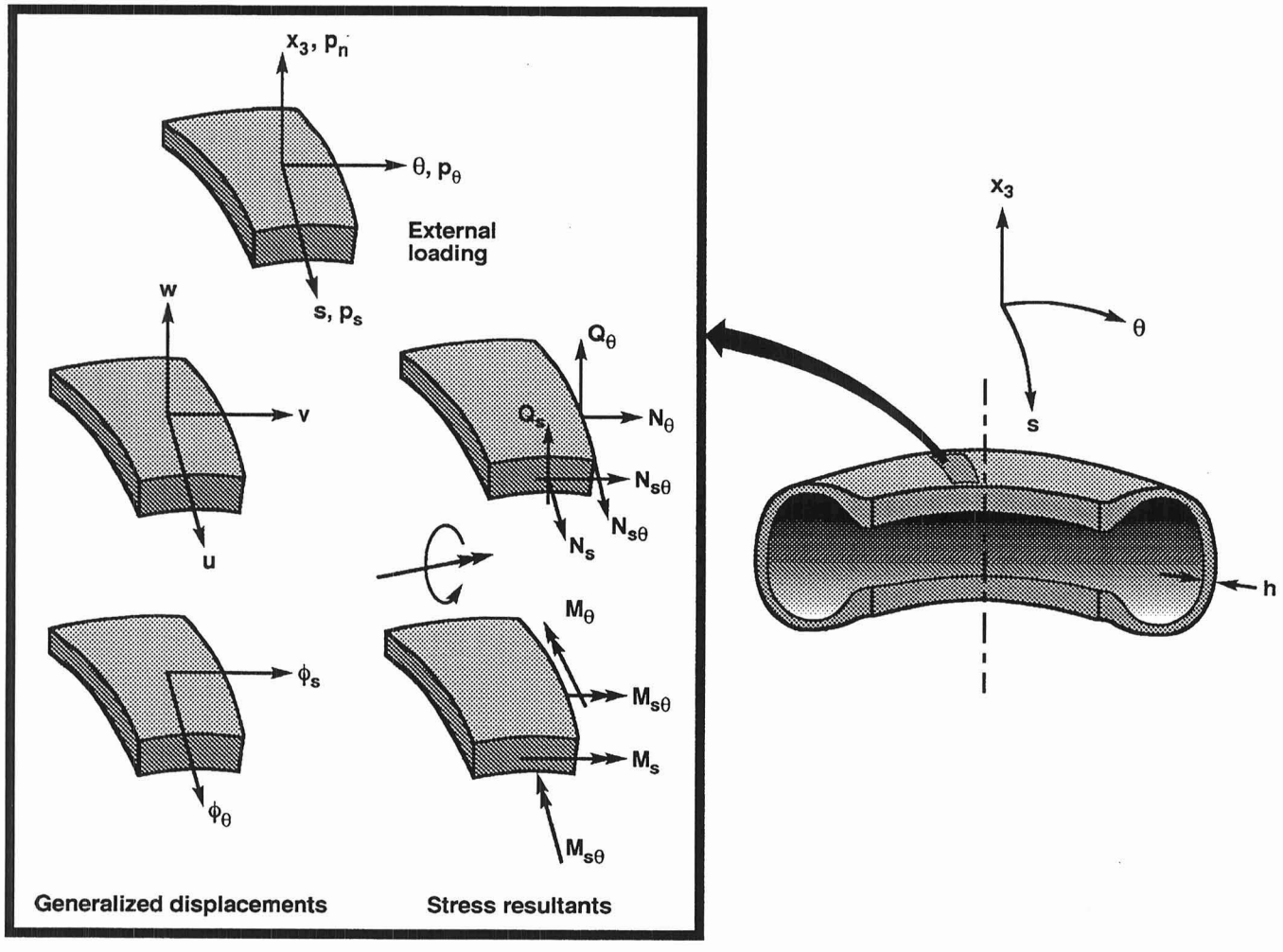

Figure 2.

FINITE ELEMENT MODELING (Cont'd.)

The discrete finite element equations governing the frictionless contact response of the tire are obtained by using a modified, two-field, Hellinger-Reissner mixed variational principle. The modification consists of augmenting the functional of that principle by two terms: the Lagrange multiplier associated with the nodal contact pressures and a regularization term which is quadratic in the Lagrange multipliers (Refs. 6 to 9). The resulting nonlinear equations are shown in Fig. 3. The vector $\{Z\}$ is the global response vector which includes the stress-resultant parameters and the nodal values of the generalized displacements; $\{\lambda\}$ is the vector of nodal values of Lagrange multipliers associated with the contact nodes; [K] is the linear matrix of the discrete tire model; [Q], [R] are the matrices associated with the contact condition and the regularization term; $\{G(Z)\}$ is the vector of nonlinear terms; p is a load parameter; $\{P\}$ is the vector of normalized external forces; $\{g_o\}$ is the vector associated with initial gaps in the contact region; and ε is a penalty parameter.

Response (Nonlinear Equations)

$$\begin{bmatrix} K & Q \\ Q & \frac{R}{\varepsilon} \end{bmatrix} \begin{Bmatrix} Z \\ \lambda \end{Bmatrix} + \begin{Bmatrix} G(Z) \\ 0 \end{Bmatrix} - \begin{Bmatrix} pP \\ g_o \end{Bmatrix} = 0$$

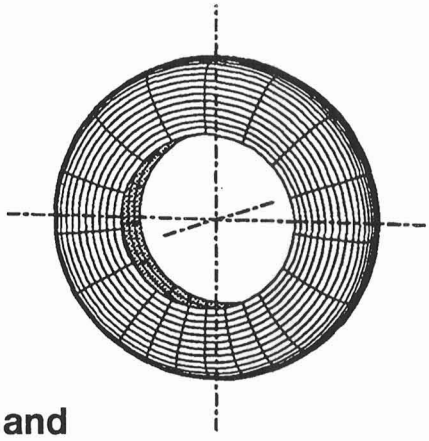

where

- $\{Z\}, \{\lambda\}$ = response and Lagrange multiplier vectors
- $[K]$ = linear matrix of the discrete tire model
- $[Q], [R]$ = matrices associated with contact condition and regularization term
- $\{G(Z)\}$ = vector of nonlinear terms
- p = load parameter
- $\{P\}$ = normalized load vector
- $\{g_o\}$ = vector associated with initial gap
- ε = penalty parameter

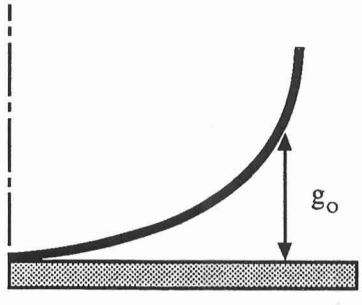

Figure 3.

The governing equations for the sensitivity coefficients are shown in Fig. 4. In these equations, d represents a typical tire parameter. Note that the governing equations for the response are nonlinear but those for the sensitivity coefficients are linear.

Sensitivity Coefficients (Linear Equations)

$$\begin{bmatrix} K+\dfrac{\partial G_i}{\partial Z_j} & Q \\ Q & \dfrac{R}{\varepsilon} \end{bmatrix} \begin{Bmatrix} \dfrac{\partial Z}{\partial d} \\ \dfrac{\partial \lambda}{\partial d} \end{Bmatrix} = \begin{Bmatrix} -\left[\dfrac{\partial K}{\partial d}\right]\{Z\} + \\ \dfrac{\partial g_o}{\partial d} \end{Bmatrix} - \begin{Bmatrix} pP \\ g_o \end{Bmatrix}$$

d = typical tire parameter

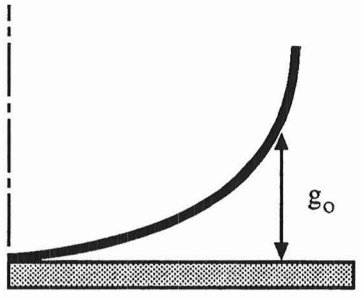

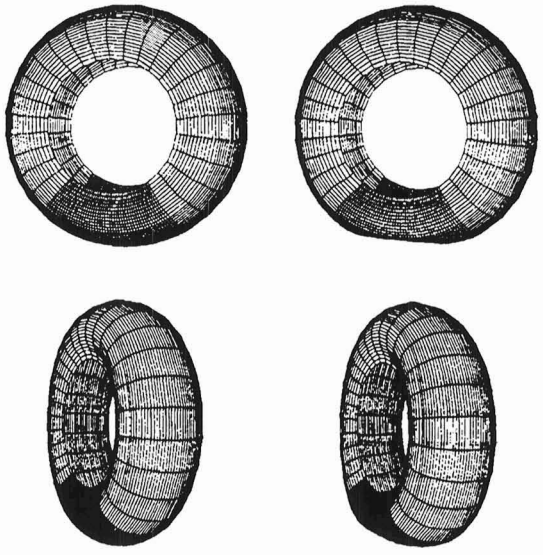

Figure 4.

SENSITIVITY COEFFICIENTS

Figure 5 highlights the sensitivity coefficients for tires, their uses, and the approaches used for their evaluation.

The tire parameters, with respect to which the sensitivity of the response need to be evaluated, include rubber and cord material properties, cord end counts, epi, cord diameters, and cord angles with the meridional direction.

Among the uses of the sensitivity coefficients are:

1. Determine a search direction in the application of nonlinear mathematical programming algorithms.
2. Assess effects of uncertainties in geometric and material parameters of the tire.
3. Predict changes in tire response due to changes in material parameters.
4. Identify changes in material and geometric parameters required to achieve certain performance characteristics.

The different approaches used in evaluating the sensitivity coefficients can be grouped into the following three categories:

1. Analytical direct differentiation methods.
2. Finite different methods.
3. Semi-analytical or quasi-analytical methods.

Tire Parameters

d refers to rubber and cord material properties, epi, cord diameters and cord angles

Uses

- **Determine a search direction in the application of nonlinear mathematical programming algorithms**
- **Assess effects of uncertainties in geometric and material parameters of the tire**
- **Predict changes in tire response due to changes in material parameters**
- **Identify changes in material and geometric parameters required to achieve certain performance characteristics**

Approaches

- **Analytical direct differentiation methods**
- **Finite difference methods**
- **Semi-analytical or quasi-analytical methods**

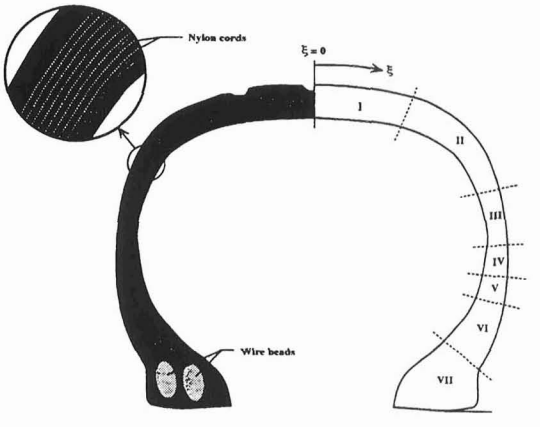

Figure 5.

REDUCTION TECHNIQUE FOR EVALUATING THE RESPONSE AND SENSITIVITY COEFFICIENTS

The reduction technique for evaluating the response and sensitivity coefficients is highlighted in Fig. 6.

The response vector {Z} is approximated by a linear combination of a few preselected basis vectors (columns of the matrix [Γ]). The approximation can be thought of as transformation of variables (from {Z} to {ψ}). The first-order derivatives of {Z} with respect to d are obtained by differentiating the approximate expression of {Z} with respect to d.

An effective choice for the basis vectors was found to be the path derivatives; namely, the various-order derivatives of {Z} with respect to a control parameter p.

Basis Reduction

$$\{Z\}_{n,1} = [\Gamma]_{n,r}\{\psi\}_{r,1} \qquad r << n$$

$$\left\{\frac{\partial Z}{\partial d}\right\}_{n,1} = [\Gamma]_{n,r}\left\{\frac{\partial \psi}{\partial d}\right\}_{r,1} + \left[\frac{\partial \Gamma}{\partial d}\right]_{n,r}\{\psi\}_{r,1}$$

where [Γ] = transformation matrix

$$\{\psi\}, \left\{\frac{\partial \psi}{\partial d}\right\} = \text{unknown parameters}$$

Selection of [Γ]

$$[\Gamma] = \left[\left\{\frac{\partial Z}{\partial p}\right\} \left\{\frac{\partial^2 Z}{\partial p^2}\right\} \left\{\frac{\partial^3 Z}{\partial p^3}\right\} \cdots\right]$$

p = load (or displacement parameter)

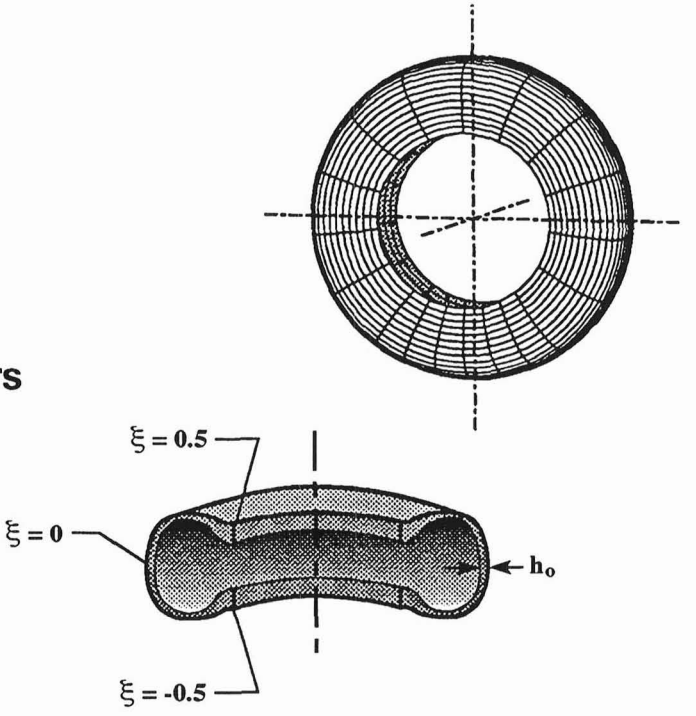

Figure 6.

REDUCTION TECHNIQUE FOR EVALUATING THE RESPONSE AND SENSITIVITY COEFFICIENTS (Cont'd.)

Treatment of Contact Response

For the application of the reduction technique to the tire contact problem, the finite element model is partitioned into two regions. The first region consists of the contact region (i.e., the nodes that are likely to come in contact with the pavement) and the second region consists of all the remaining nodes (see Fig. 7). The response vector $\{Z\}$ is partitioned accordingly.

The subvector $\{Z_1\}$ is expected to exhibit a significant change with the change in the applied load, and therefore, is not approximated. By contrast, the subvector $\{Z_2\}$ is not expected to change much, and is approximated by a linear approximation of a few preselected vectors (columns of the matrix $[\Gamma]$).

A Bubnov-Galerkin technique is used to replace the governing equations for the contact response and its sensitivity coefficients by two reduced systems of equations: a nonlinear system of equations in $\{Z_1\}$, $\{\psi\}$; and a linear systems of equations in $\left\{\frac{\partial Z_1}{\partial d}\right\}, \left\{\frac{\partial \psi}{\partial d}\right\}$.

Partitioning of {Z}

$$\{Z\} = \begin{Bmatrix} Z_1 \\ Z_2 \end{Bmatrix}$$

Basis Reduction

$$\begin{Bmatrix} Z_1 \\ Z_2 \end{Bmatrix} = \begin{bmatrix} I & 0 \\ 0 & \Gamma \end{bmatrix} \begin{Bmatrix} Z_1 \\ \psi \end{Bmatrix}$$

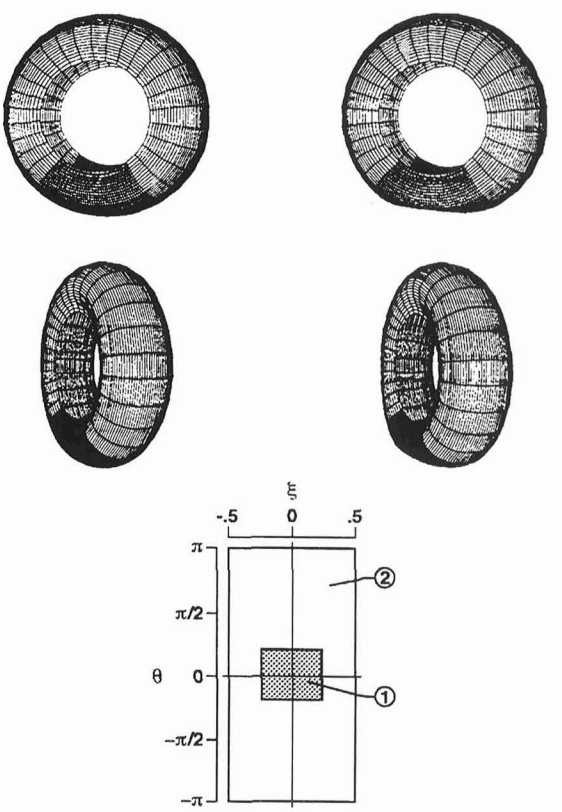

Figure 7.

SPACE-SHUTTLE NOSE-GEAR TIRE
Characteristics of the Cross Section

To test and evaluate the effectiveness of the reduction technique, the frictionless contact response of the space shuttle orbiter nose-gear tire and its sensitivity coefficients were generated by this technique. The geometric characteristics of the tire cross section are shown in Fig. 8. Each half of the tire cross section was divided into seven segments. Each segment contained a different number of layers, different material properties corresponding to different cord content in the composite, and varying cord orientations.

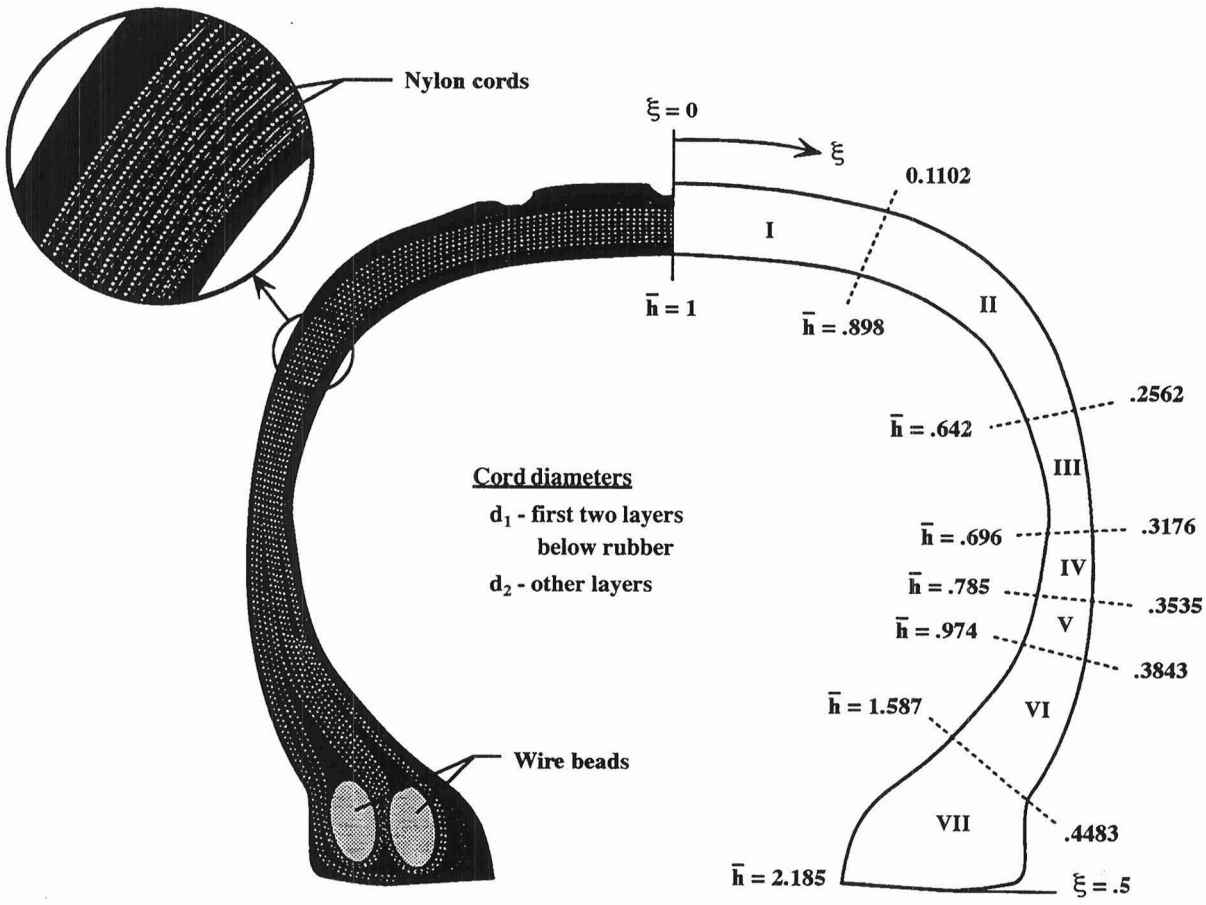

Figure 8.

STATIC LOAD DEFLECTION CHARACTERISTICS

Figure 9 shows a plot of the applied displacement versus the total vertical contact load obtained by two different discrete models. The full inflation pressure of 320 psi was applied to the tire, then the inflated tire was pressed against the rigid pavement, and the applied displacement was increased. Model 1 has a total of 10,188 displacement degrees of freedom in the full tire and model 2 has a total of 20,736 displacement degrees of freedom. The close agreement between the predictions of the two finite element models and the experiments is clearly seen in Fig. 9.

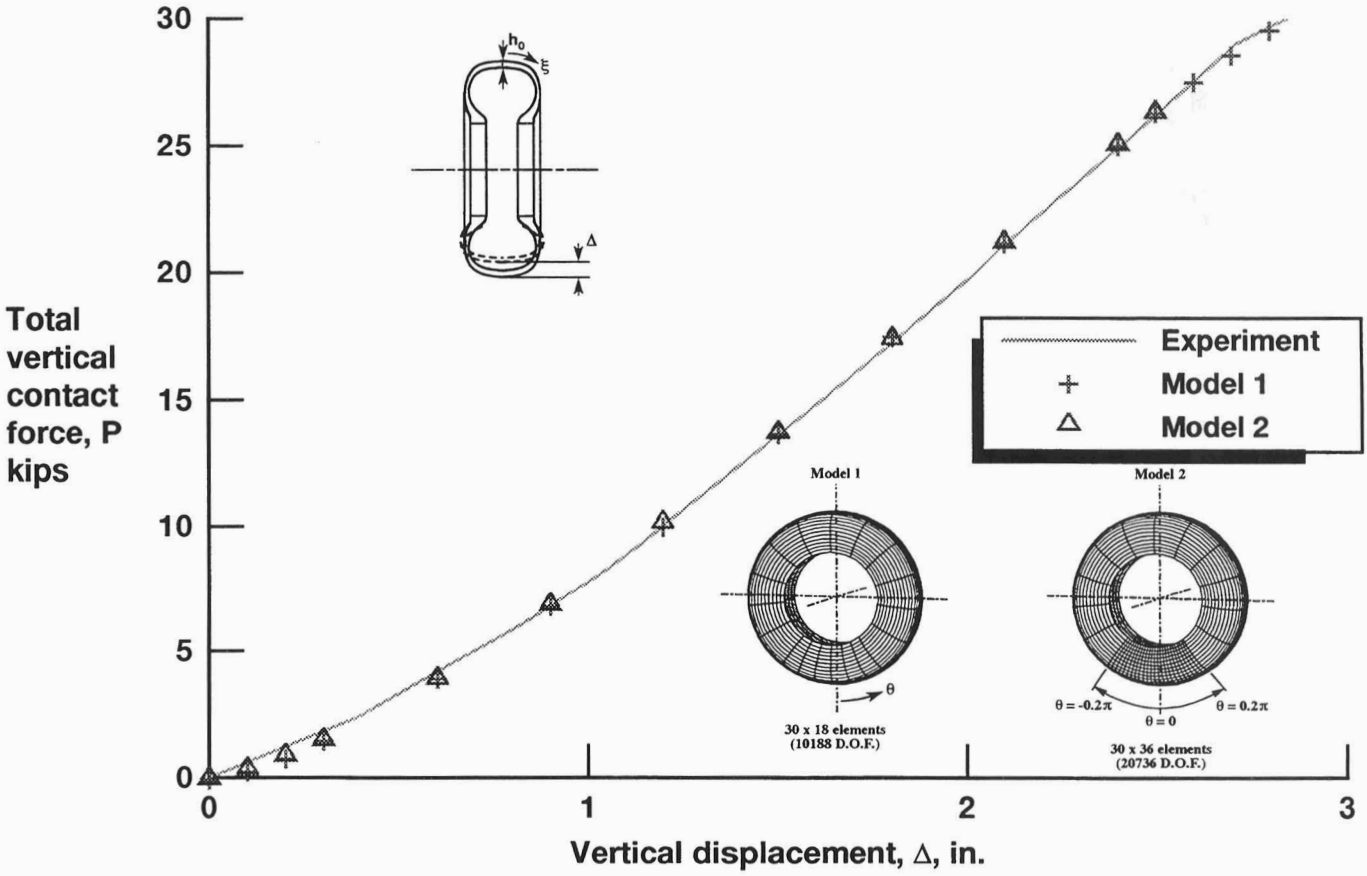

Figure 9.

ACCURACY OF NONLINEAR TIRE RESPONSE PREDICTED BY REDUCTION TECHNIQUE

Figure 10 shows the accuracy of the total vertical contact load and the total strain energy U, in the region $-0.45 \leq \xi \leq 0.45$ obtained by using the reduction technique in conjunction with model 2. The tire was divided into two regions. The contact region (region 1) had 432 elements and 9065 displacement degrees of freedom. Region 2 had 648 elements and 11,311 displacement degrees of freedom. The basis vectors were generated at $\Delta/h_0 = 0.1$ and were not updated throughout the range of the applied displacement considered. For the range of Δ/h_0 considered, the total vertical contact force obtained by using ten basis vectors are almost undistinguished from those obtained by using the full system of finite element equations. The error in the total strain energy obtained by using ten vectors was less than 2% (the scale selected in Fig. 10 amplifies that error).

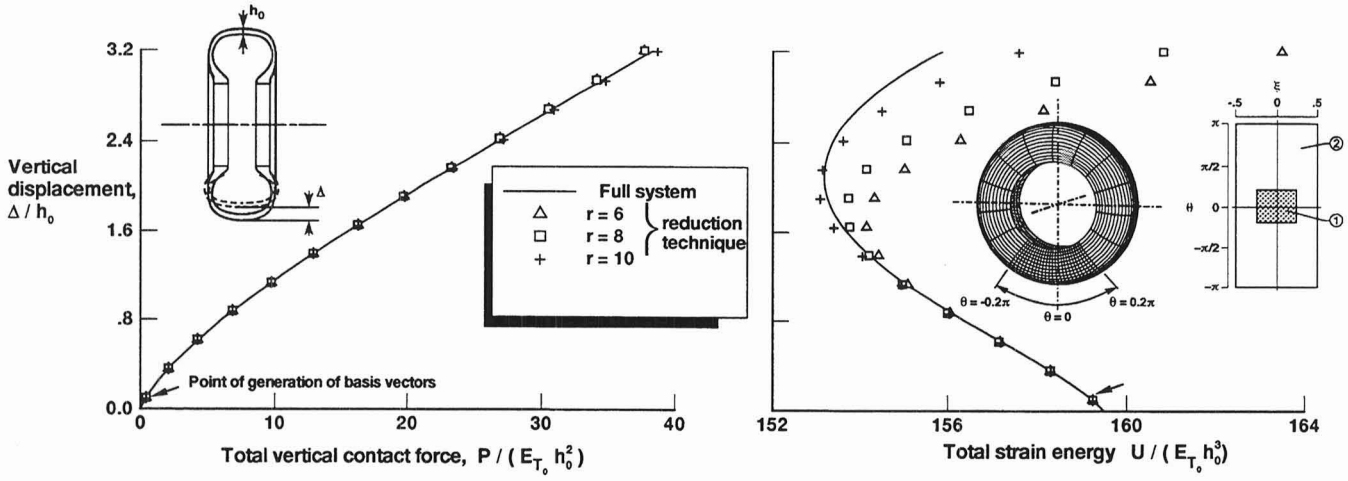

Figure 10.

VARIATION OF TOTAL STRAIN ENERGY DENSITY DISTRIBUTION WITH APPLIED DISPLACEMENT

Figure 11 shows the variation of the strain energy density with applied displacement in the region -0.45 $\leq \xi \leq$ 0.45. The strain energy density contours are normalized by dividing them by $E_{T_0} h_0$. The strain energy density is primarily influenced by the inflation pressure. Since the normal tractions associated with contact are compressive, the strain energy density is reduced in the contact region as well as in the sidewall area near the bead (away from the contact region).

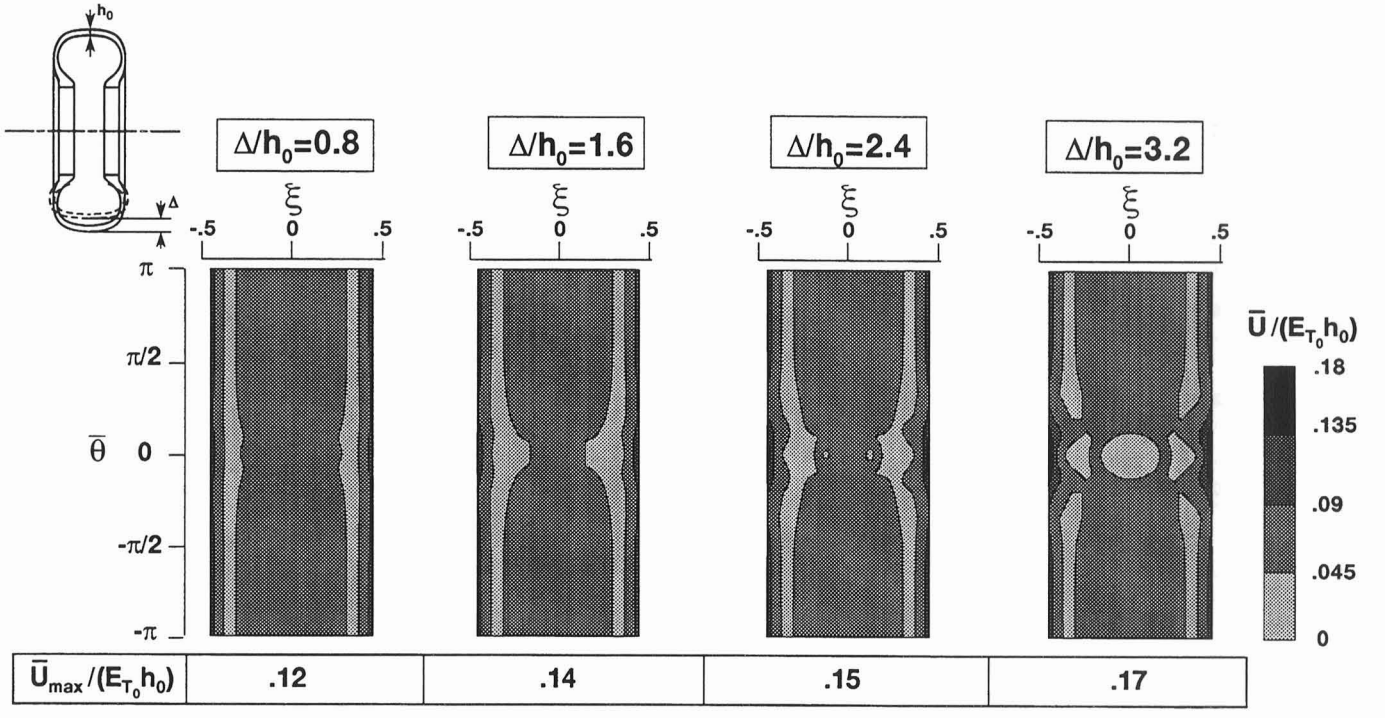

Figure 11.

ACCURACY OF THE SENSITIVITY COEFFICIENTS OF THE TOTAL STRAIN ENERGY WITH RESPECT TO CORD DIAMETERS AND YOUNG'S MODULI

Figure 12 gives an indication of the accuracy of the total strain energy with respect to the cord diameters d_1 and d_2, and Young's moduli of the cord and rubber E_c and E_r. As can be seen from Fig. 12, reasonable accuracy is obtained with only ten basis vectors.

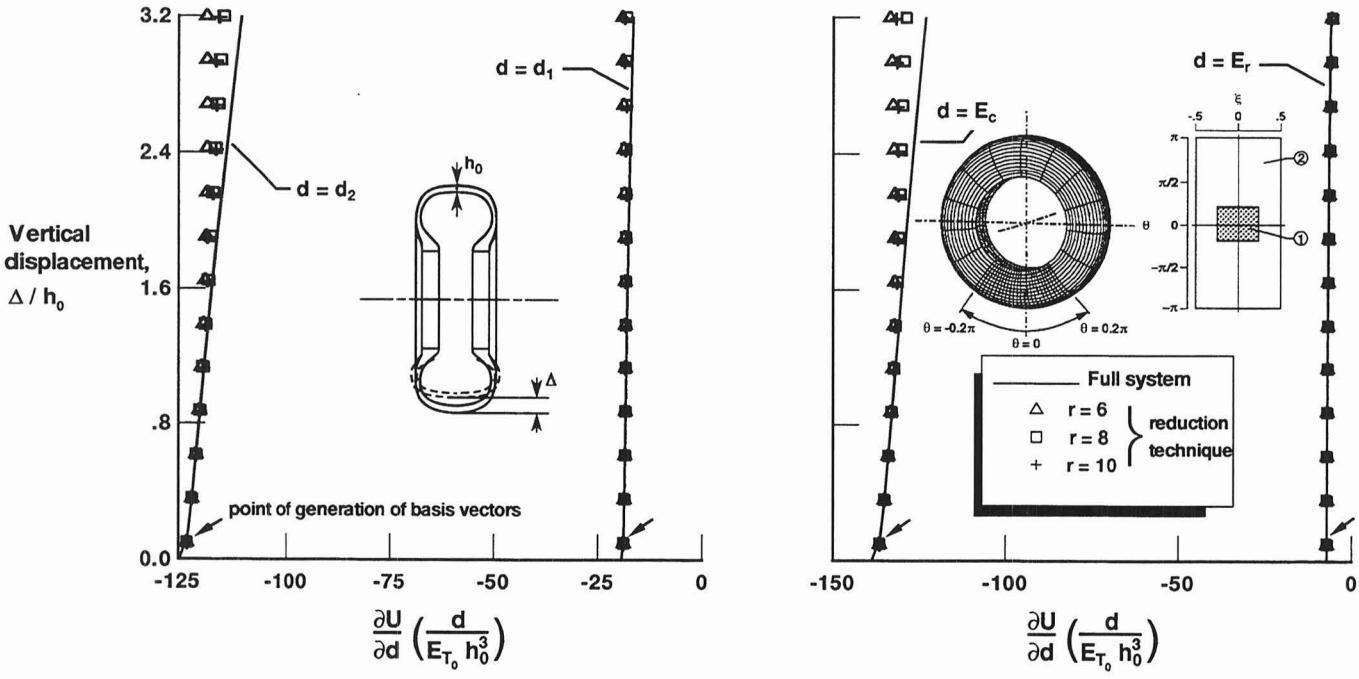

Figure 12.

ACCURACY OF THE SENSITIVITY COEFFICIENTS OF THE TOTAL STRAIN ENERGY WITH RESPECT TO THE PARAMETER OF THE CORD END COUNT AND CORD ANGLE

Figure 13 gives an indication of the accuracy of the sensitivity coefficients of the total strain energy with respect to the parameters of the cord end count, epi, and the cord angle $\tilde{\theta}$. Again, for the entire range of applied displacements, reasonable accuracy is obtained with only ten vectors.

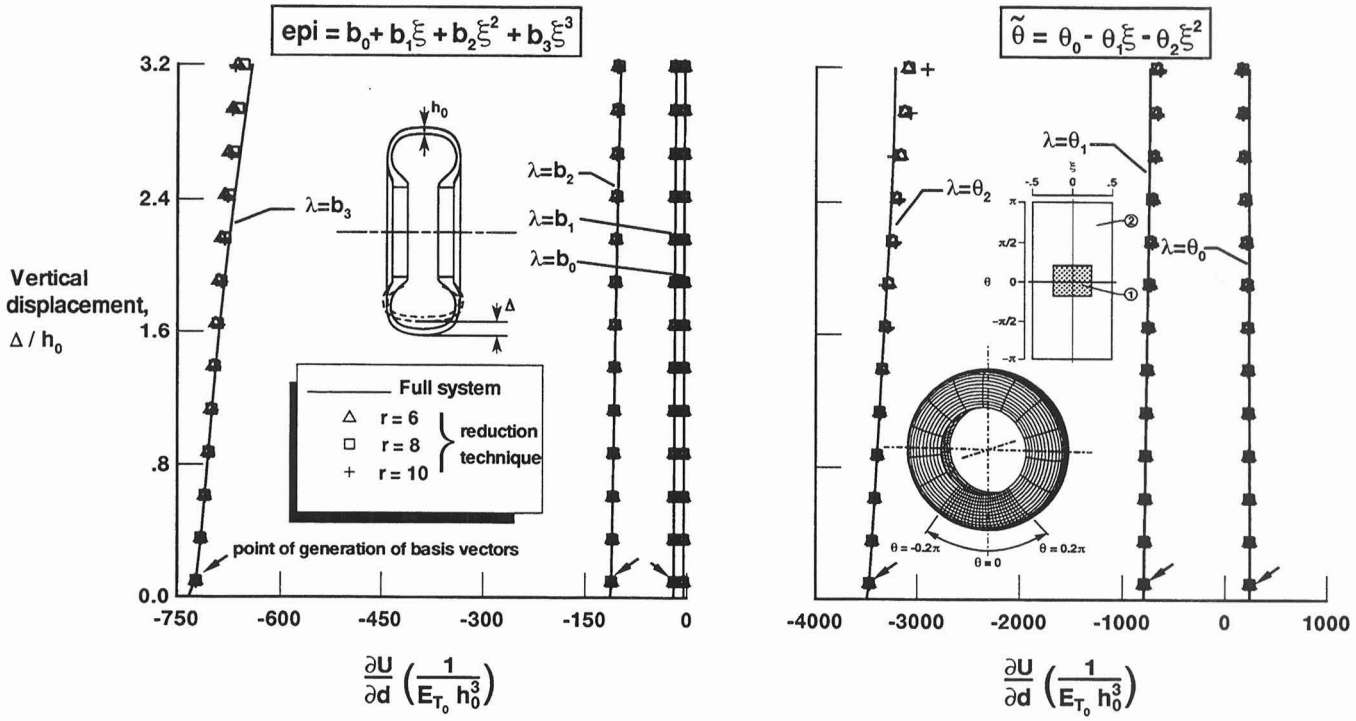

Figure 13.

NORMALIZED CONTOUR PLOTS OF TOTAL STRAIN ENERGY DENSITY $\frac{\partial \bar{U}}{\partial d} \Big/ \left.\frac{\partial \bar{U}}{\partial d}\right|_{max}$

Figure 14 shows normalized contour plots of the sensitivity coefficients of the total strain energy density $\bar{U}$ with respect to four tire parameters (E_c, E_r, d_1 and d_2) at $\Delta/h_0 = 0.8$ and $\Delta/h_0 = 3.2$. Each sensitivity coefficient is normalized by dividing by the maximum value at the given Δ/h_0. The distributions of the sensitivity coefficients of $\bar{U}$ differ from each other and from the corresponding $\bar{U}$ distributions. Also, the distributions of the sensitivity coefficients away from the contact area remain nearly axisymmetric.

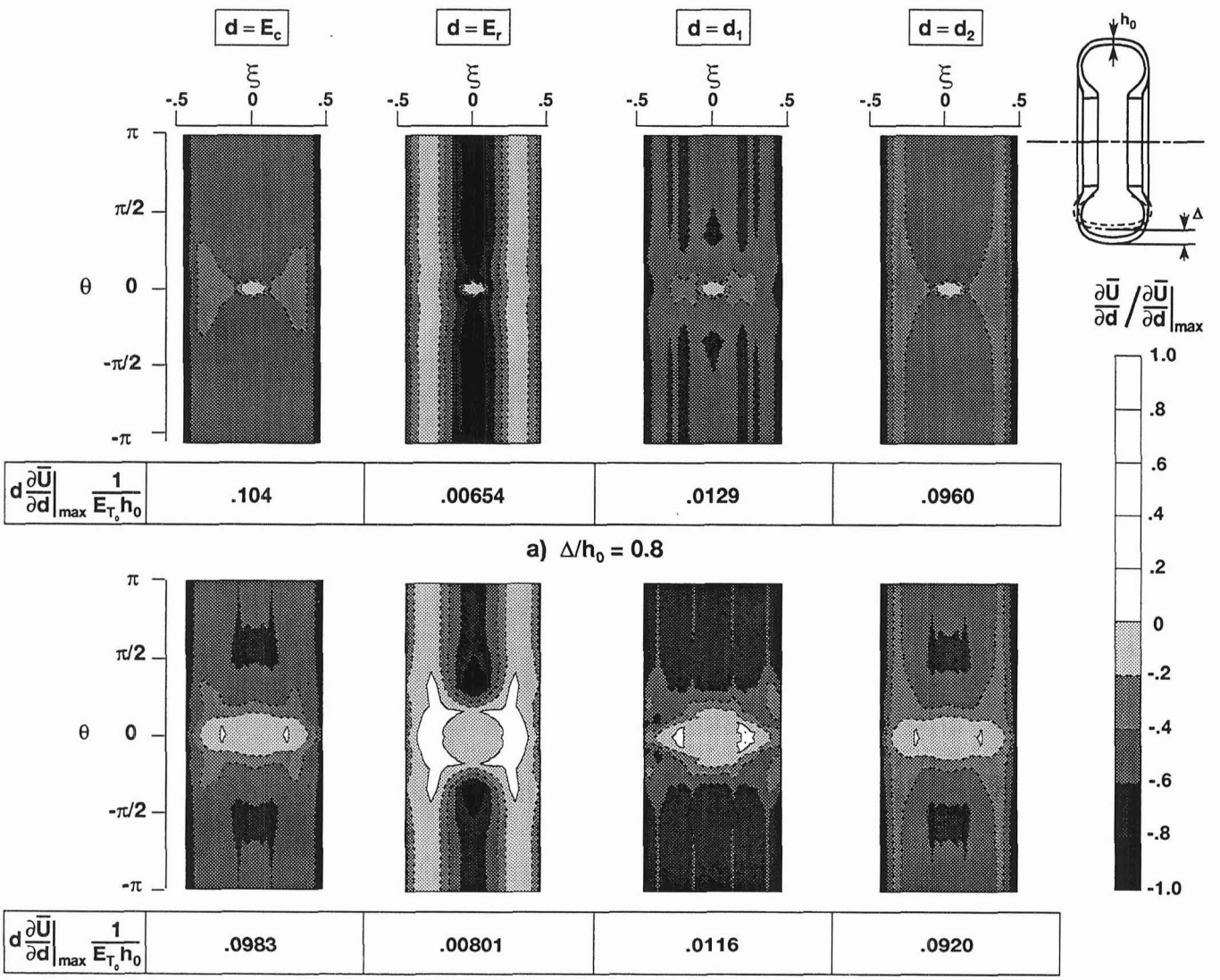

Figure 14.

FUTURE DIRECTIONS OF RESEARCH ON REDUCTION TECHNIQUES

Some of the research topics which have high potential for enhancing the effectiveness of reduction techniques are (see Fig. 15):

1. Development of reduction techniques for hierarchical sensitivity analysis, which includes evaluation of the sensitivity coefficients of the tire response with respect to a hierarchy of parameters ranging from the stiffnesses of the two-dimensional laminated shell model of the tire to the material and geometric parameters of the cord, rubber and interface/interphase.
   Hierarchical sensitivity analysis can be used to:
   a) bridge the gap between material development and structural design of tires;
   b) study the response of tires at different length scales; and
   c) study the effect of imperfections in the tire materials, cord diameters, and cord angles on the response.
2. Application of reduction techniques to: a) damage and failure analysis; b) thermomechanical response of tires; and c) rolling tire problem.

- **Development of reduction techniques for hierarchical sensitivity analysis**
  - **Bridge gap between material development and structural design of tires**
  - **Study the response of tires at different length scales**
  - **Study of the effect of imperfections on the tire response**
- **Applications to**
  - **Damage and failure analysis**
  - **Thermomechanical response of tires**
  - **Rolling tire problem**

Figure 15.

SUMMARY

In summary, some recent advances in the application of reduction techniques to tire contact problems have been reviewed. This included both prediction of contact response and sensitivity analysis.

Reduction techniques have the potential of making detailed (large scale) contact and sensitivity analysis practical.

Among the research topics that have high potential of increasing the effectiveness of reduction techniques are: a) hierarchical sensitivity analysis, which can be used to bridge the gap between material development and structural design of tires and to help in identifying the length scale required in modeling the different regions of the tire; and b) application of reduction techniques to damage and failure analysis of tires.

- **Reviewed some recent advances in the application of reduction techniques to tire contact problems**
  - **prediction of contact response**
  - **sensitivity analysis**
- **Reduction techniques can make detailed (large scale) contact and sensitivity analyses practical**
- **Future directions of research on reduction techniques**
  - **hierarchical sensitivity analysis-bridge gap between material development and structural design of tires**
  - **application to damage and failure analysis of tires**

Figure 16.

REFERENCES

1. Noor, A. K. and Tanner, J. A., "Advances and Trends in the Development of Computational Models for Tires," Computers and Structures, Vol. 20, Nos. 1-3, 1985, pp. 517-533.

2. Noor, A. K., Andersen, C. M. and Tanner, J. A., "Exploiting Symmetries in the Modeling and Analysis of Tires," Computer Methods in Applied Mechanics and Engineering, Vol. 63, 1987, pp. 37-81.

3. Noor, A. K., Kim, K. O. and Tanner, J. A., "Analysis of Aircraft Tires Via Semianalytic Finite Elements," Finite Elements in Analysis and Design, Vol. 6, 1990, pp. 217-233.

4. Sanders, J. Lyell, Jr., "Nonlinear Theories for Thin Shells," Quarterly of Applied Mathematics, Vol. 21, No. 1, April 1963, pp. 21-36.

5. Budiansky, Bernard, "Notes on Nonlinear Shell Theory," Journal of Applied Mechanics, Vol. 35, No. 2, June 1968, pp. 393-401.

6. Simo, Juan C., Wriggers, Peter, and Taylor, Robert L., "A Perturbed Lagrangian Formulation for the Finite Element Solution of Contact Problems," Computational Methods in Applied Mechanics and Engineering, Vol. 50, No. 2, Aug. 1985, pp. 163-180.

7. Stein, E., Wagner, W. and Wriggers, P., "Finite Element Postbuckling Analysis of Shells with Nonlinear Contact Constraints," in Finite Element Methods for Nonlinear Problems, P. G. Bergan, K. J. Bathe and W. Wunderlich (eds.), Springer-Verlag, 1986, pp. 719-744.

8. Wriggers, P., Wagner, W. and Stein, E., "Algorithms for Nonlinear Contact Constraints with Application to Stability Problems of Rods and Shells," Computational Mechanics, Vol. 2, 1987, pp. 215-230.

9. Kim, O. K., Tanner, J. A., Noor, A. K. and Robinson, M. P., Computational Methods for Frictionless Contact with Application to Space Shuttle Orbiter Nose-Gear Tires, NASA TP-3073, May 1991.

Tire Footprint Studies

Mangal Chawla and John Medzorian
Landing Gear Systems Group
Flight Dynamics Directorate
Wright Laboratory
Wright Patterson Air Force Base, OH

TIRE FOOTPRINT STUDIES

Mangal Chawla and John Medzorian
Landing Gear Systems Group
Flight Dynamics Directorate
Wright Laboratory
Wright Patterson Air Force Base, OH

ABSTRACT

This presentation covers the results of tire footprint studies conducted in the Landing Gear Development Facility of the USAF Wright Laboratory at the Wright Patterson Air Force Base, OH. Tire footprint studies are essential in understanding tire wear mechanisms and computing tire tread wear rates. The power input into the tread is the driving force for tread wear. Variables needed for power input calculations include the footprint pressure and slip velocity distributions. Studies were performed on the effects of power input distributions due to vertical load, camber, yaw, inflation pressure and tire construction. For the present study, two tire constructions, one radial and the other bias, were selected. These tires were for the F-16 Block 30 Fighter aircraft, both of which were previously worn. The present study was limited to steady straight roll with a 14,000 lb vertical load, a 310 psi inflation pressure, zero yaw and camber. All tests were conducted on the Tire Force Machine (TFM) with a specialized sensor plate with embedded pressure sensors (X, Y and Z) and slip sensors (X & Y). All tests were conducted for a table speed of 1 in/s. Tests on the TFM show that the power intensity distributions and total power for both tire constructions are quite similar for straight roll. Later on, tests were also conducted on a modified dynamometer which was overlaid with a grit wear surface. The tire speed was maintained at 40 miles per hour and yaw was set to four degrees. Dynamometer tests showed that radial tires have more tread wear than the bias tire, however, in the field, radial tires have longer life. This is a dilemma.

PROBLEM

Included is the problem statement of low tire life.

- ***Excessive tire wear due to***
  - ***Large contact pressures***
  - ***Large slip velocity***
- ***Very few sorties/tire***
  - ***F-16 Block 30...8-12 landings***
  - ***F-16 Block 40 & 50...4-8 landings***

Figure 1.

OBJECTIVES

This slide states the objectives of the program. The main objectives are to quantify parameters affecting tread wear.

- ***Overall Objective: Increase tread life***
- ***Focussed Objective: Quantify operating conditions and tire design parameters affecting tread wear***
  - ***Operating conditions***
    - ***Load***
    - ***Takeoff/Landing profile (speed, yaw, camber, braking)***
    - ***Antiskid characteristics***
  - ***Tire design parameters***
    - ***Inflation pressure***
    - ***Tire construction (bias/radial)***

Figure 2.

NEEDS

This slide states the need to study footprint pressures and slips so that power intensity can be calculated for tread-wear computations. This data is needed for steady roll, yaw and braking conditions.

- ***Determine aircraft tire footprint slips and pressures to quantify power intensity due to***
  - ***Steady roll***
  - ***Yaw***
    - ***Steady (crosswind)***
    - ***Cornering***
  - ***Braking***
    - ***Steady (constant slip)***
    - ***Transient (antiskid)***

Figure 3.

TOOLS

The tools for carrying out this work are the Tire Force Machine (TFM) and specialized sensors which measure footprint pressures and slips.

- ***Experimental***
  - ***TFM***
    - ***Steady conditions only***
    - ***Low speed (2 in/s max)***
- ***Analytical/Computational***
  - ***FEM***

Figure 4.

APPROACH

The approach to this work is to perform roll tests on the TFM and measure footprint data using specialized equipment. The data will be analyzed for wear energy rate determination. Parameter studies will be performed to compare the performance of radial against bias tire for vertical load, yaw and camber.

- ***Perform Footprint measurements on TFM***
  - ***Slip velocity x (longitudinal) y (lateral)***
  - ***Contact force intensity x, y and z (normal)***
- ***Data Analysis***
  - ***Wear energy rate determination***
  - ***Parametric studies on F-16 tires***
    - ***Type (Radial vs Bias)***
    - ***Vertical Load***
    - ***Yaw***
    - ***Camber***

Figure 5.

SENSORS FOR TIRE FORCE MACHINE

This slide shows the layout of pressure and slip sensors and the direction of roll. Pressure sensors give X, Y and Z components of pressure, whereas slip sensors measure X and Y components. There are 37 pressure gages and 37 slip gages. The holes are 1/4 inch in diameter. The pressure sensors are level with the top of the plate whereas the slip sensors are 4 mils above the plate surface.

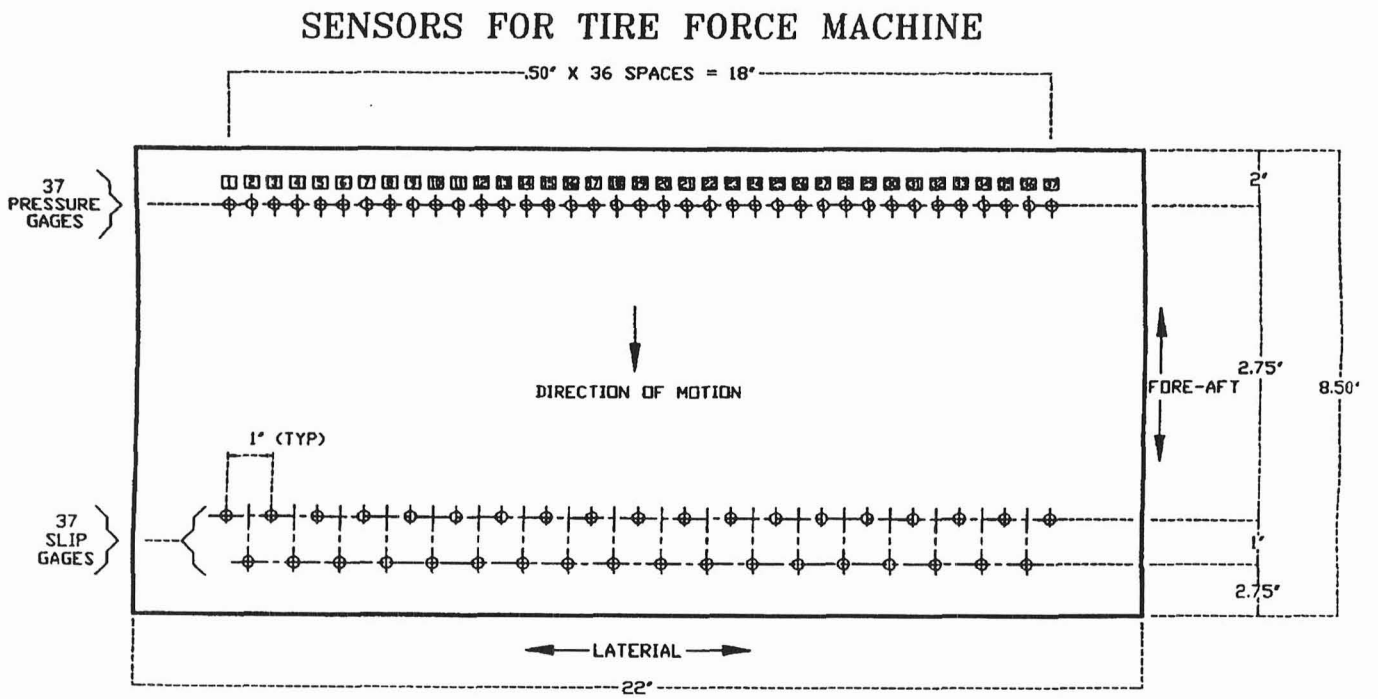

Figure 6.

F-16 BLOCK 30

This is a mesh plot of the vertical (Z) pressure for the bias and the radial F-16 Block 30 tires. Both plots look similar in shape and magnitude indicating that the normal pressures are nearly the same for these tires. In all runs, the tire is rolling towards the origin in the fore-aft direction. The table speed was 0.981 in/s for the radial tire and 0.913 in/s for the bias tire.

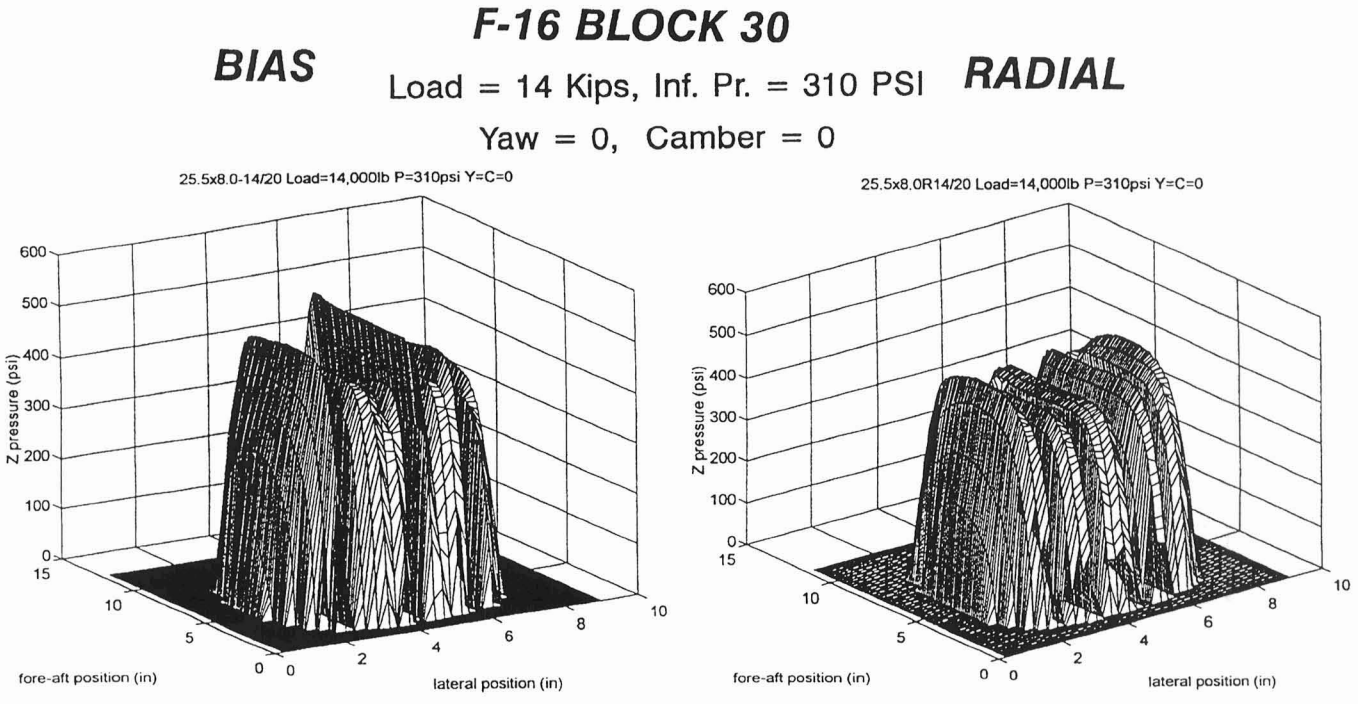

Figure 7.

X PRESSURE

This is a plot of the fore-aft (X) pressure distributions for both radial and bias tires. The total measured steady state X force is 140 lbs for the radial tire and 271 lbs for the bias tires. This compares favorably with the predicted integrated values of 265 lbs and 141 lbs. Therefore, the total dissipative power in these runs works out to be 137 in-lb/s for the radial tire and 247 in-lb/s for the bias tire.

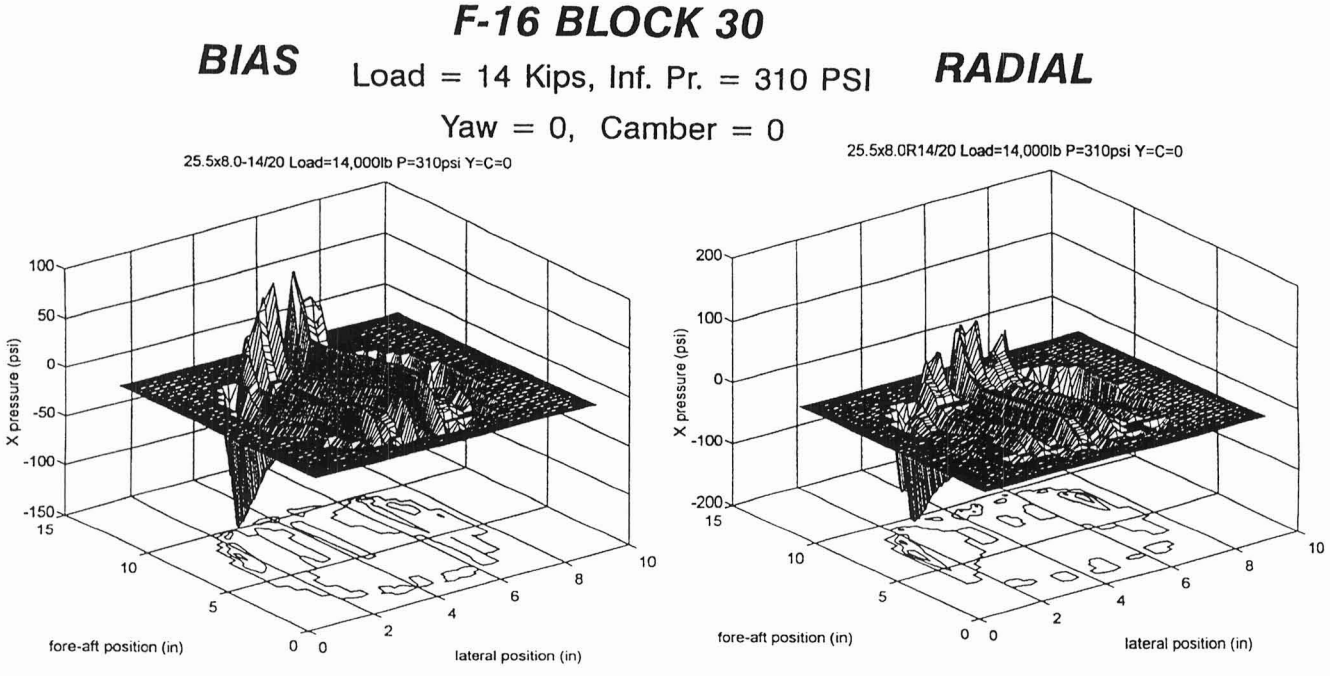

Figure 8.

Y PRESSURE

This is a plot of the lateral (Y) pressure distribution for both radial and bias tires.

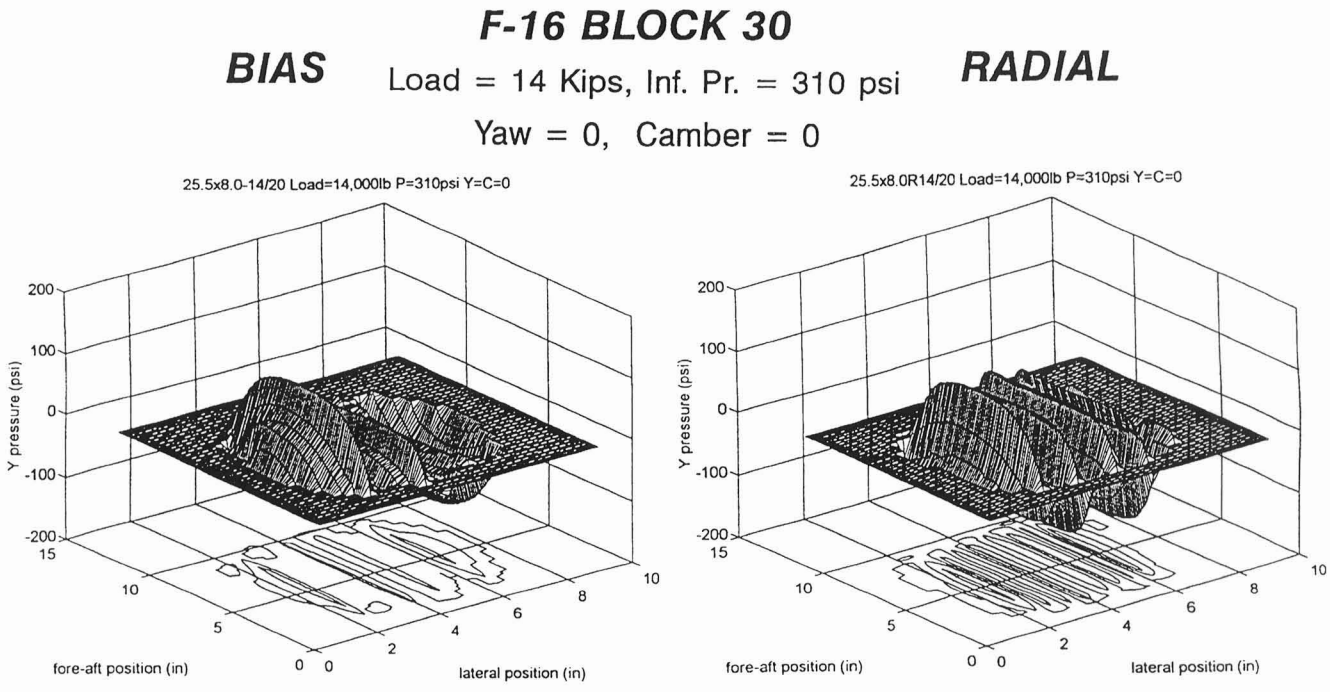

Figure 9.

TRACTION VECTOR

This is a plot of the traction vectors providing both magnitude and direction.

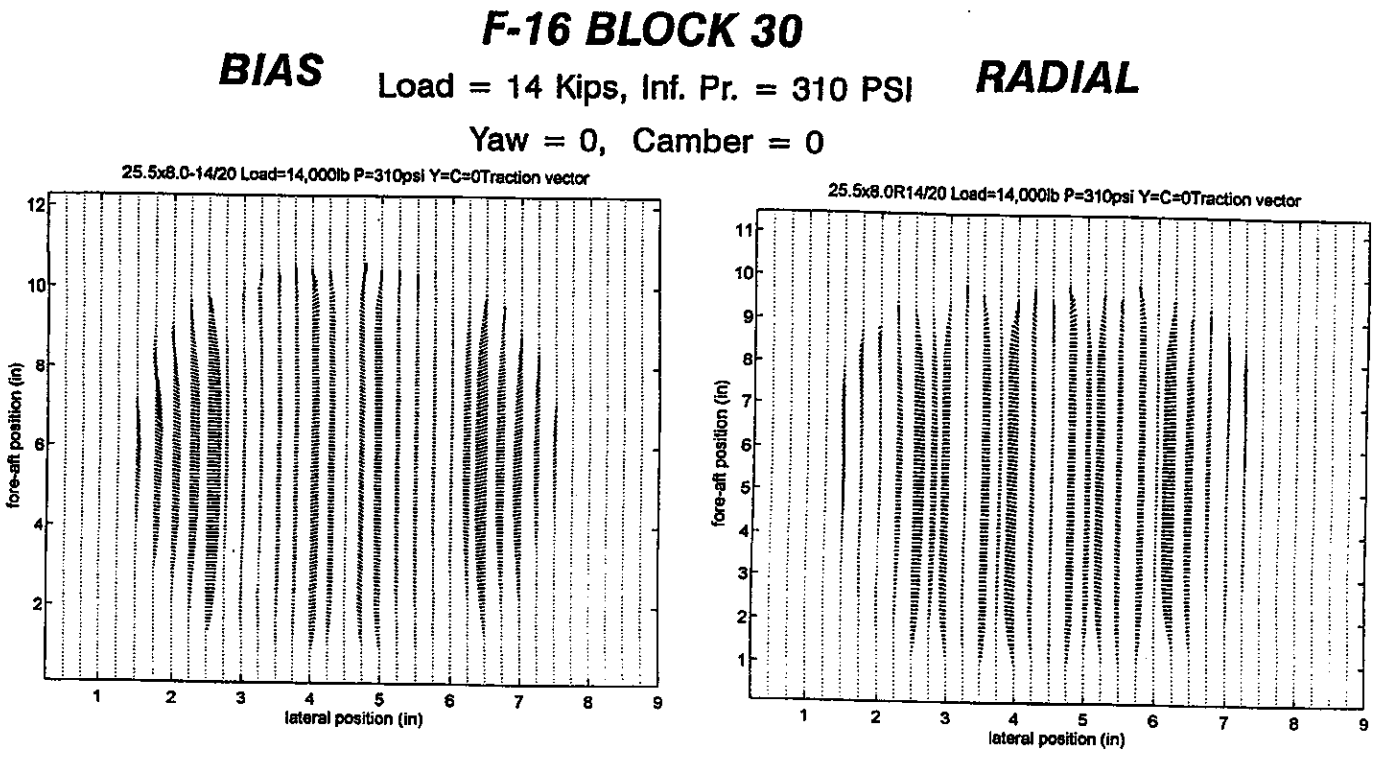

Figure 10.

X SLIP VELOCITY

This is the slip velocity in the fore-aft (X) direction, measured in mil/s. Note that the peaks occur at the trailing edges of the contact patch. The slip velocity was calculated from the slips by using the central difference method. The data was manipulated such that at zero normal (Z) pressure, no slip velocity occurs. Note that the maximum slip occurs at the trailing edge of the tire.

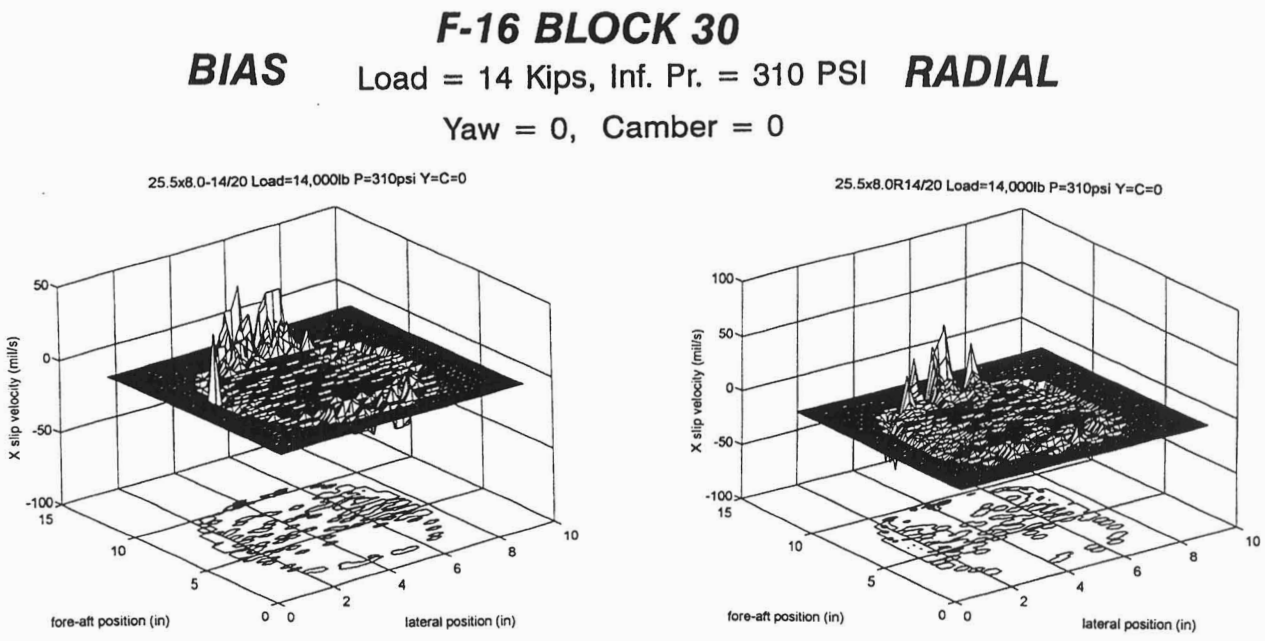

Figure 11.

Y SLIP VELOCITY

This is the slip velocity in the lateral (Y) direction, measured in mil/s. Note that the maximum values occur at the trailing and leading edges of the contact patch.

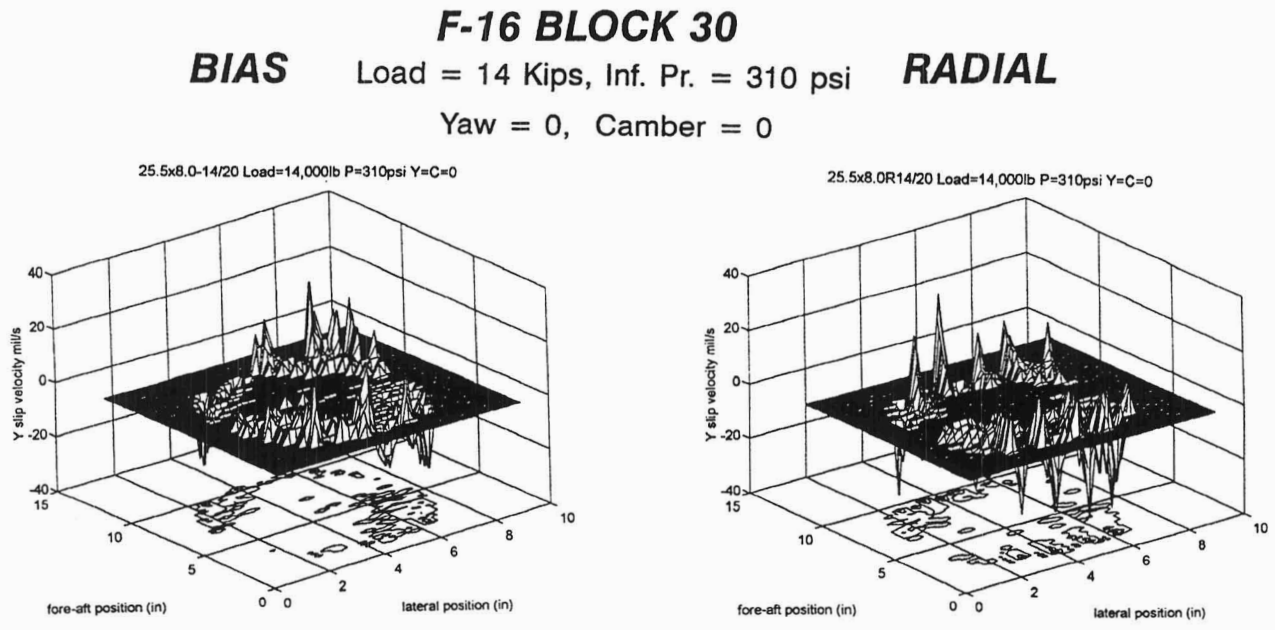

Figure 12.

SLIP VELOCITY MAGNITUDE

This is the slip velocity magnitude measured in mil/s. Note that the peaks occur at the trailing edge of the contact patch.

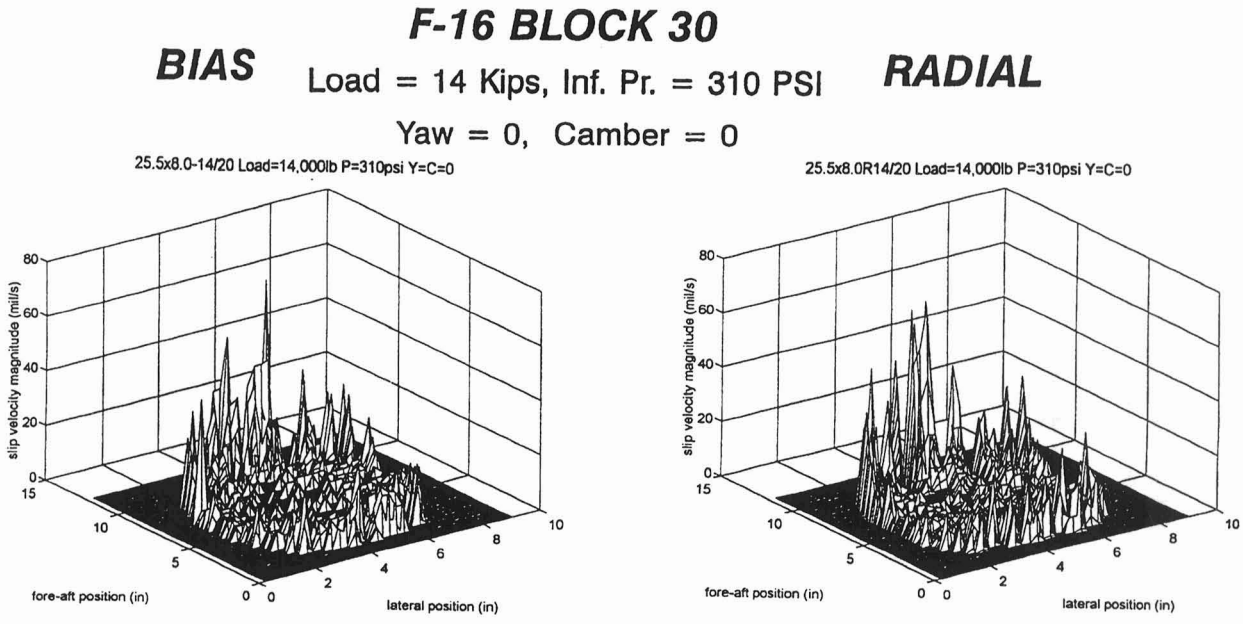

Figure 13.

SLIP VECTOR

This is the plot of the slip velocity vector giving both the magnitude and the direction. There is a lot of similarity between the two tires.

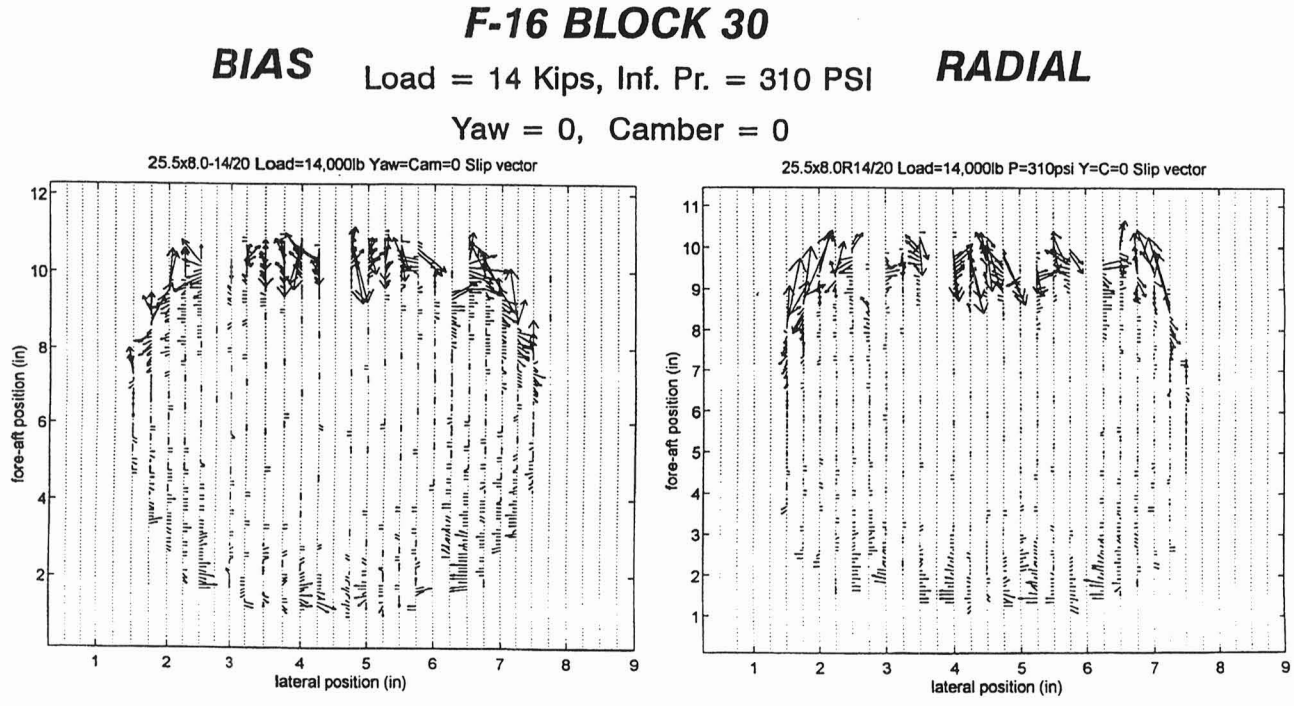

Figure 14.

Z PRESSURE

This is a contour plot of the normal (Z) pressure for the bias tire. When integrated over the contact area, it gives a total value of 15,565 lbs which compares favorably with the applied load of 14,000 lbs.

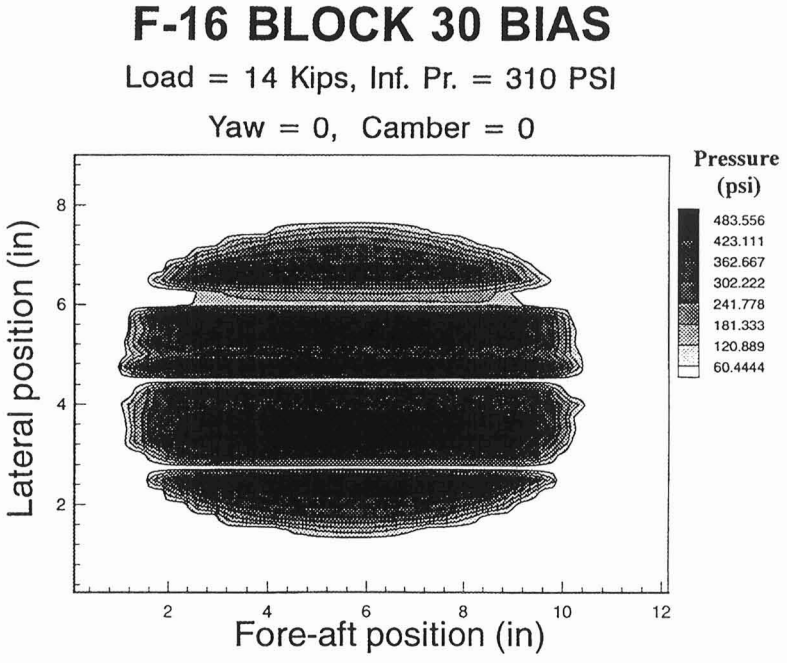

Figure 15.

SLIP VELOCITY MAGNITUDE

This is a contour plot of the slip velocity magnitude for the bias tire. Note that the slip velocity is maximum at the trailing edge of the contact patch. This data was manipulated by zeroing out values which occurred at zero contact pressure.

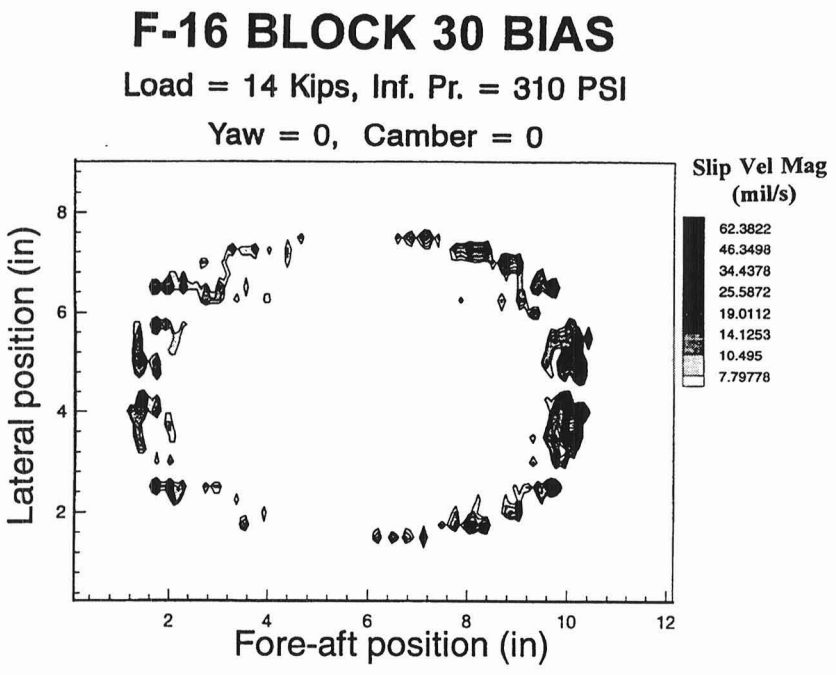

Figure 16.

POWER INTENSITY

This is a contour plot of the power intensity calculated by multiplying an assumed value of coefficient of friction (0.5) and the Z pressure by the slip velocity magnitude. Note that the maximum power intensity occurs at the front and back edges of the tire. The total dissipative power due to friction was determined by integrating this power intensity over the contact area. The resulting value was 22.0 in-lb/s for the bias tire.

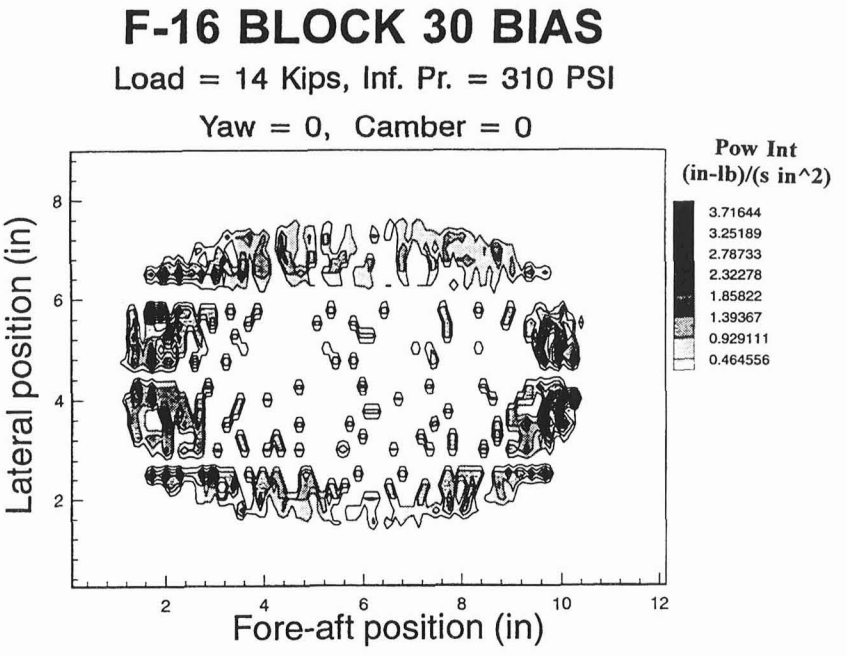

Figure 17.

Z PRESSURE

This is a contour plot of the normal (Z) pressure for the radial tire. When integrated over the contact area it gives a value of 15,095 lbs which compares favorably with the applied load of 14,000 lbs.

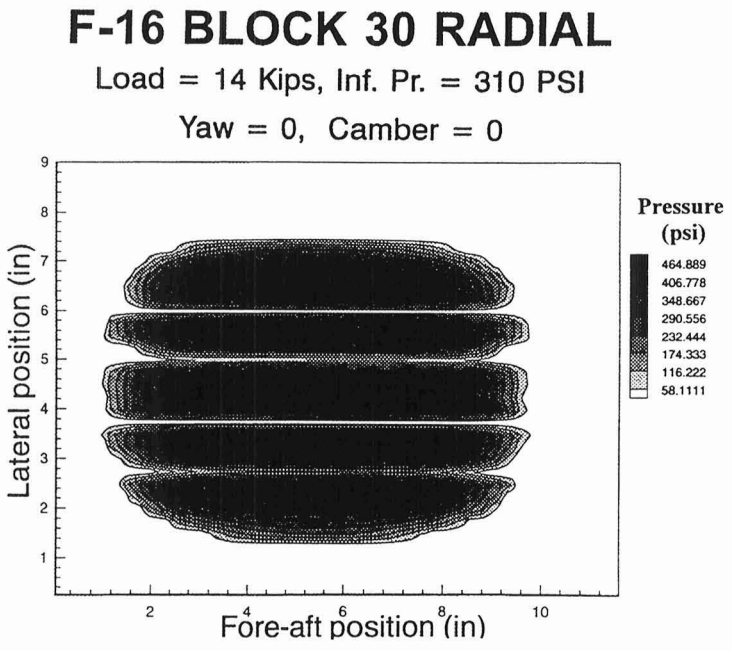

Figure 18.

SLIP VELOCITY MAGNITUDE

This is a contour plot of the slip velocity magnitude for the radial tire. Note that the slip velocity is maximum on the trailing edge of the contact patch. This data was manipulated by zeroing out values which occurred at zero contact pressure.

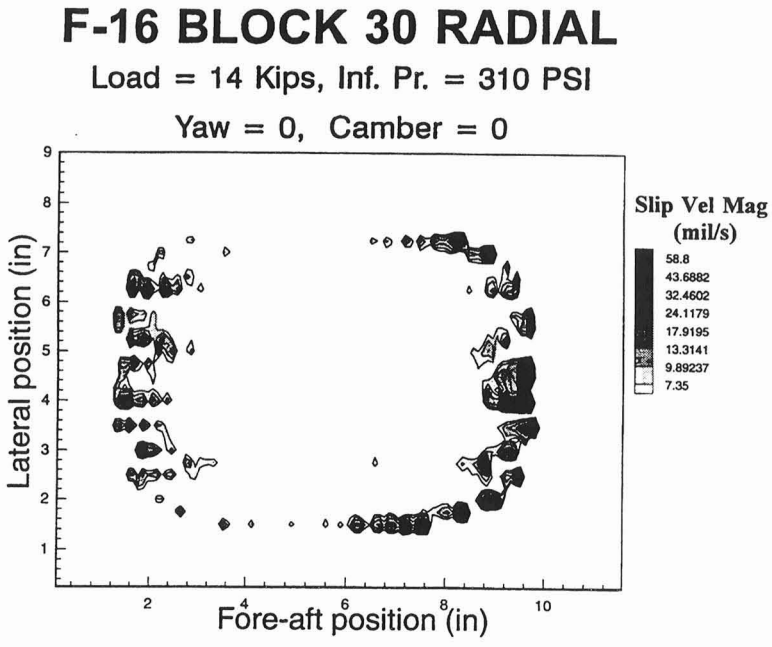

Figure 19.

POWER INTENSITY

This is a contour plot of the power intensity for the radial tire. This was calculated by multiplying an assumed value of coefficient of friction (0.50) by the Z pressure and the slip velocity magnitude. Note that the maximum power intensity occurs at the front and back edges of the tire. The total dissipative power was 23.6 in-lb/s for the radial tire.

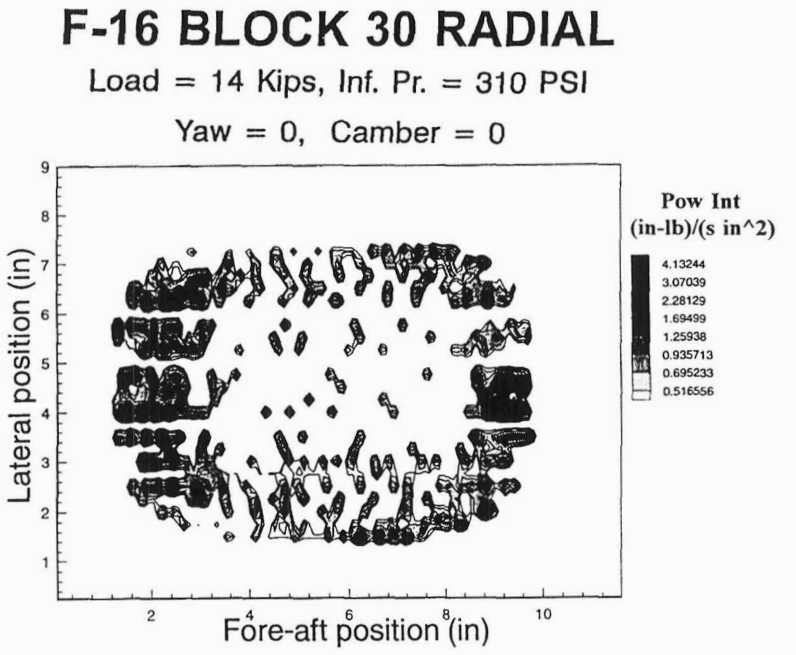

Figure 20.

POWER INTENSITY

This is a mesh plot of the power intensity distributions for the two tires.

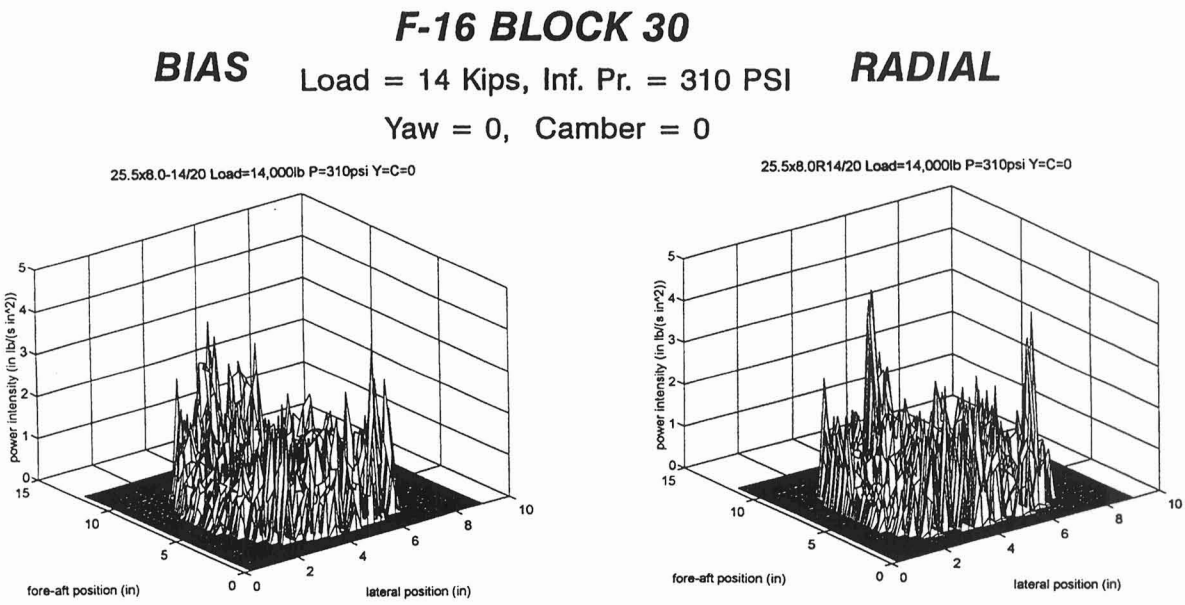

Figure 21.

POWER PER UNIT LENGTH

This is a plot of power per unit width plotted in the lateral direction which was determined by integrating the power intensity along the fore-aft direction.

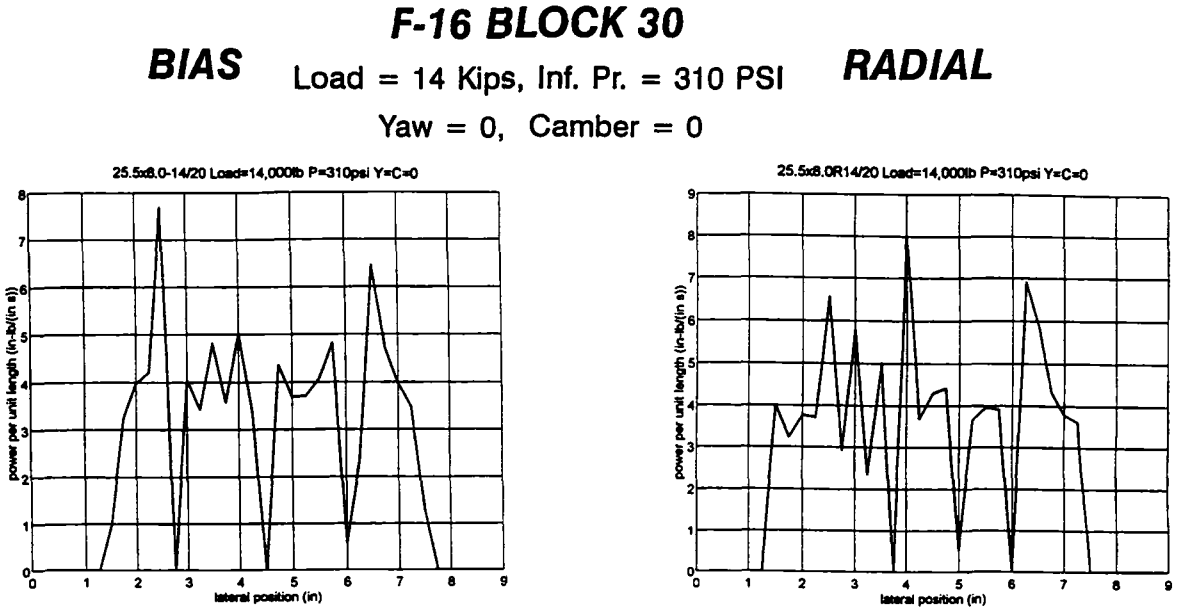

Figure 22.

RESULTS

Tabulated results for both bias and radial tires. All values are very similar.

	BIAS	RADIAL
Table speed (in/s)	*.913*	*.981*
Maximum slip (mil)	*31.3*	*49.1*
X-Pressure range psi	*(-122,94)*	*(-147,106)*
Y-Pressure range psi	*(-113,126)*	*(-132,115)*
Traction Vector psi	*(0,129)*	*(0,148)*
Z-Pressure range psi	*(0,544)*	*(0,523)*
X-Slip Velocity mil/s	*(-70,50)*	*(-63,64)*
Y-Slip Velocity mil/s	*(-25,30)*	*(-35,35)*
Slip Velocity Magnitude mil/s	*(0,70.2)*	*(0,66.1)*
Power Intensity in-lb/(s-in^2)	*(0,4.2)*	*(0,4.6)*

MEASURED (INTEGRATED) TOTAL VALUES

Fx (lb)	*271 (265)*	*140 (141)*
Fy (lb)	*182 (6)*	*157 (199)*
Fz (lb)	*14,000 (15,565)*	*14,000 (15,291)*
Power (in-lb/s)	*(22.0)*	*(23.6)*

Figure 23.

WL DYNAMOMETER TIRE WEAR RESULTS SUMMARY

This is a plot of the actual tire wear on the bias and the radial tires which were run on a modified external drum dynamometer overlaid with an abrasive material glued to the wheel surface. The tire was run with four degrees of yaw at 40 mph. Tread wear was quantified by measuring the maximum groove depth on the tire tread. Note that on the dynamometer for four degrees of yaw, the radial tire wears much faster than the bias tire. However, in the field, the radial tires have longer tread life.

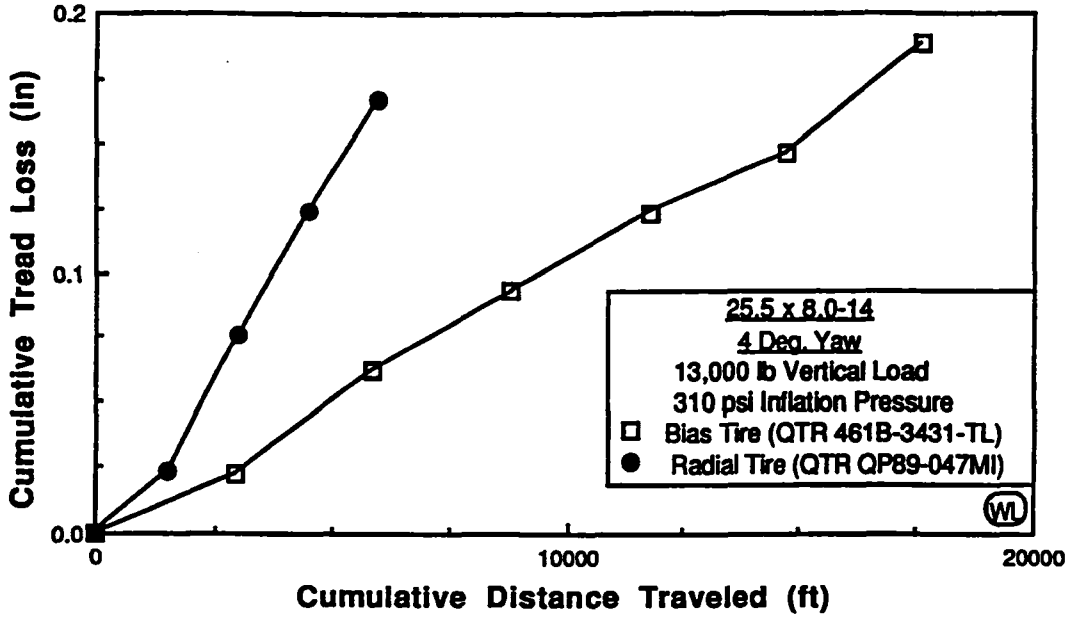

Figure 24.

Determination of Tire Cross-Sectional Geometric Characteristics From a Digitally Scanned Image

Kent T. Danielson
Center for Computational Structures Technology
University of Virginia
Hampton, VA

DETERMINATION OF TIRE CROSS-SECTIONAL GEOMETRIC CHARACTERISTICS FROM A DIGITALLY SCANNED IMAGE

Kent T. Danielson
Center for Computational Structures Technology
University of Virginia
NASA Langley Research Center
Hampton, Virginia 23681

INTRODUCTION

A semi-automated procedure is described for the accurate determination of geometrical characteristics using a scanned image of the tire cross-section. The procedure can be useful for cases when CAD drawings are not available or when a description of the actual cured tire is desired.

The determination of geometric details from digitally scanned images has been used for various applications (e.g., air flow behavior [1]). It is believed, however, that this is the first published application to tires. Curves representing the perimeter of the tire cross-section are determined by an edge tracing scheme, and the plyline and cord-end positions are determined by locations of color intensities. Edge and contour tracing techniques and their resultant chain codes were introduced by Freeman [2]. Since then, numerous variations have been reported. Several survey articles have reviewed and analyzed these techniques [3-5].

The current procedure provides an accurate description of the perimeter of the tire cross-section and the locations of plylines and cord-ends. The position, normals, and curvatures of the cross-sectional surface are included in this description. The locations of the plylines provide the necessary information for determining the ply thicknesses and relative position to a reference surface. Finally, the locations of the cord-ends provide a means to calculate the cord-ends per inch (epi).

Menu driven software has been developed to facilitate the procedure using the commercial code, PV-Wave by Visual Numerics, Inc., to display the images. From a single user interface, separate modules are executed for image enhancement, curve fitting the edge trace of the cross-sectional perimeter, and determining the plyline and cord-end locations. The code can run on SUN or SGI workstations and requires the use of a mouse to specify options or identify items on the scanned image.

OBJECTIVES

The objective is to produce a robust procedure with the following characteristics:

1. An accurate determination of the cross-sectional geometry of an actual tire
   a) Perimeter shape
   b) Ply centerline locations
   c) Ply end counts

2. Simple user-friendly software

3. Produce a simple database that can be used to create finite element models, to merge with CAD systems, or to be manipulated for other purposes.

RAW SCANNED IMAGE

The procedure begins by capturing the tire cross-sectional image in monochrome with a flat bed scanner. A raw scanned image of the space shuttle nose gear tire is shown in Figure 1. The image is a grid of points (pixels), each with its own grayscale value (scaled numerical value specifying amount of black and white). The raw image is digitally enhanced for use with the software. A slight enhancement is used to more easily inspect the accuracy of the calculated geometry with respect to the tire image. In addition, a higher degree of enhancement is used with the algorithms that calculate the geometric quantities.

Figure 1

DIGITALLY ENHANCED IMAGES

A separate module is executed from the user interface to produce enhanced images. The raw image is digitally enhanced by subtracting a smooth area-averaged copy, which has a predominance of low frequency components of the image, from the original. By subtracting out a smoothed or averaged image, the high frequency components, especially the tire cord-end images, are enhanced. A highly enhanced image corresponding to Figure 1 is shown in Figure 2. The highly enhanced image is used for the calculation of the geometric quantities. A slightly enhanced image will also be used to assess accuracy by superimposing the calculated geometry on it. The degree of enhancement is determined by the size of the averaged area. The software allows the user to specify the parameters that determine the degree of enhancement, and the enhanced images are displayed for inspection.

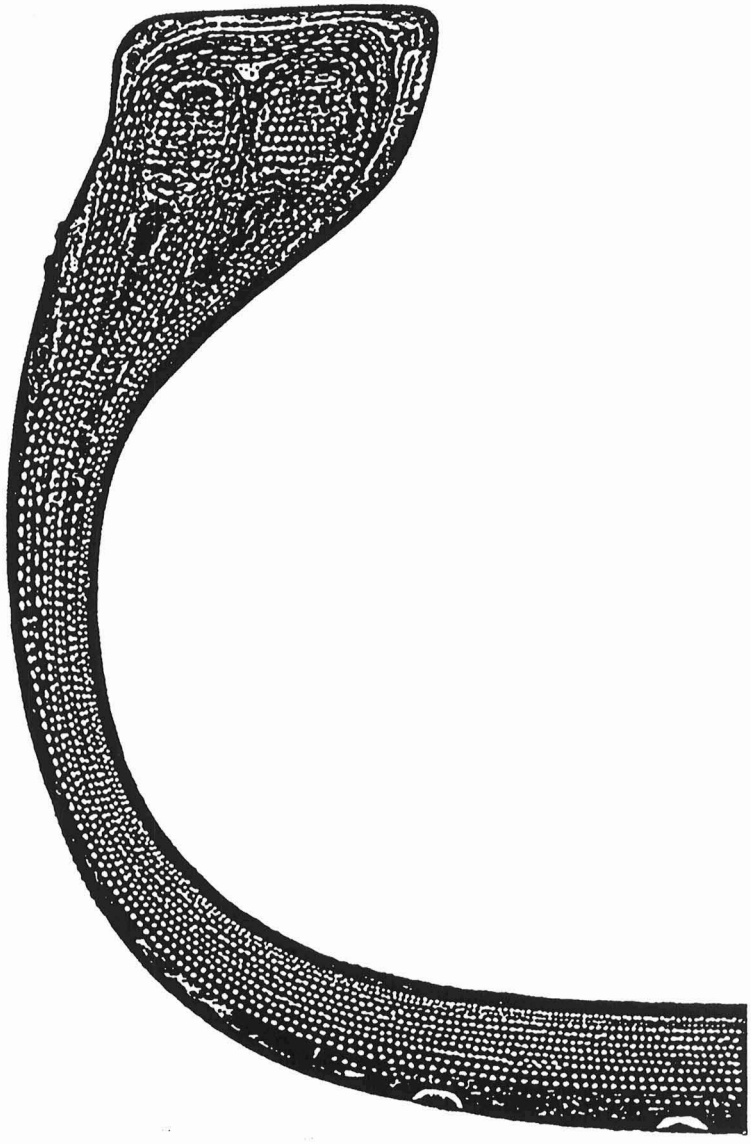

Figure 2

DETERMINATION OF CROSS-SECTIONAL PERIMETER

A separate module is also executed from the user interface to fit splines to the perimeter of the tire cross-section. The grayscale values are used to determine geometrical details, since geometry changes will generally coincide with changes in color. An edge tracing procedure is used to determine the inner and outer surface by determining when pixel grayscale values go from white to black. After the edge trace is completed, B-splines are fit to the inside and outside surfaces. The curves are used to calculate coordinates, normals to the surface, and curvatures. The software allows the user to change the spline order, number of splines, and spacing of splines. For inspection, the splines are then graphically superimposed over a plot of the edge trace points. Figure 3 shows the B-splines fit to the edge trace of the space shuttle nose gear tire.

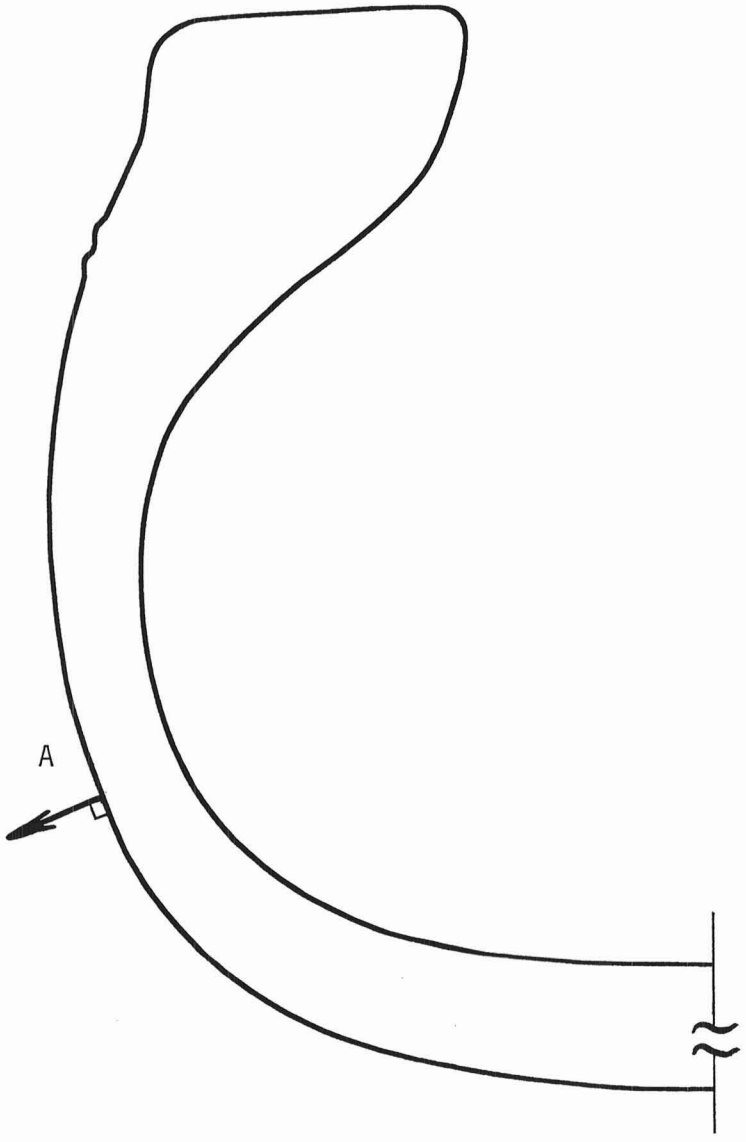

Figure 3

DETERMINATION OF PLY CENTERLINES

A separate module is also executed from the user interface to determine the locations of the ply centerlines and cord-ends. Similar to the edge trace procedure, the tire cord locations within the rubber will be determined by grayscale summations that indicate a cluster of white in the image. The plyline locations for different positions along the tire meridian are determined by a series of points on the perimeter. A mouse click on each desired point on the outside surface is made on the image, and the normal to the outside surface is determined at the point. Figure 4 shows an example for point A, which is also identified in Figure 3. The distance to the inside surface along the normal is calculated, and the distance to each ply centerline is determined by a summation of pixel grayscale values. Since the normal will not generally cross all cord-ends, a sum of pixel values is made for a fixed distance on each side of the normal. For the most accurate sums, the summation direction on each side of the normal would ideally be along the direction of the ply. The code provides a simple, yet effective, way of specifying this direction. The option is given for using the outside surface, the inside surface, or a smooth transition between the two.

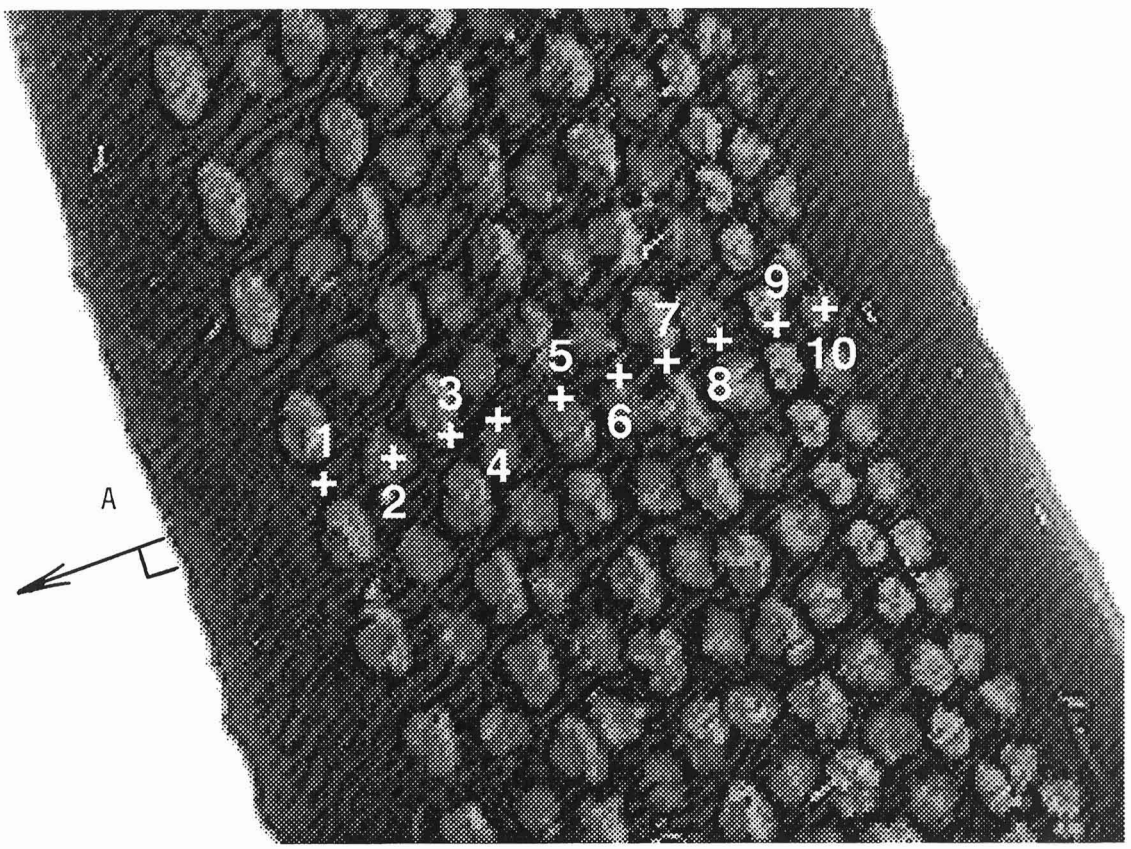

Figure 4

DETERMINATION OF PLY CENTERLINES

Each grayscale sum is assigned to its pixel position along the normal. When plotted along the normal, as shown in Figure 5 for point A, these sums should show peaks of white where the plylines lie. The peaks are chosen to be the ply centerlines and then plotted on the image for inspection. The first two peaks in Figure 5 have smaller amplitudes than the other peaks and are a result of noise in the heavily enhanced image. Inaccurate plylines like these can be deleted or new desired ones added with simple mouse clicks on the image. The other ten peaks represent the ply centerlines. Figure 4 shows the ply centerlines, as determined from the ten major peaks in Figure 5, marked by crosses on a slightly enhanced image. This procedure is repeated for other points along the tire meridian, until an adequate description is obtained.

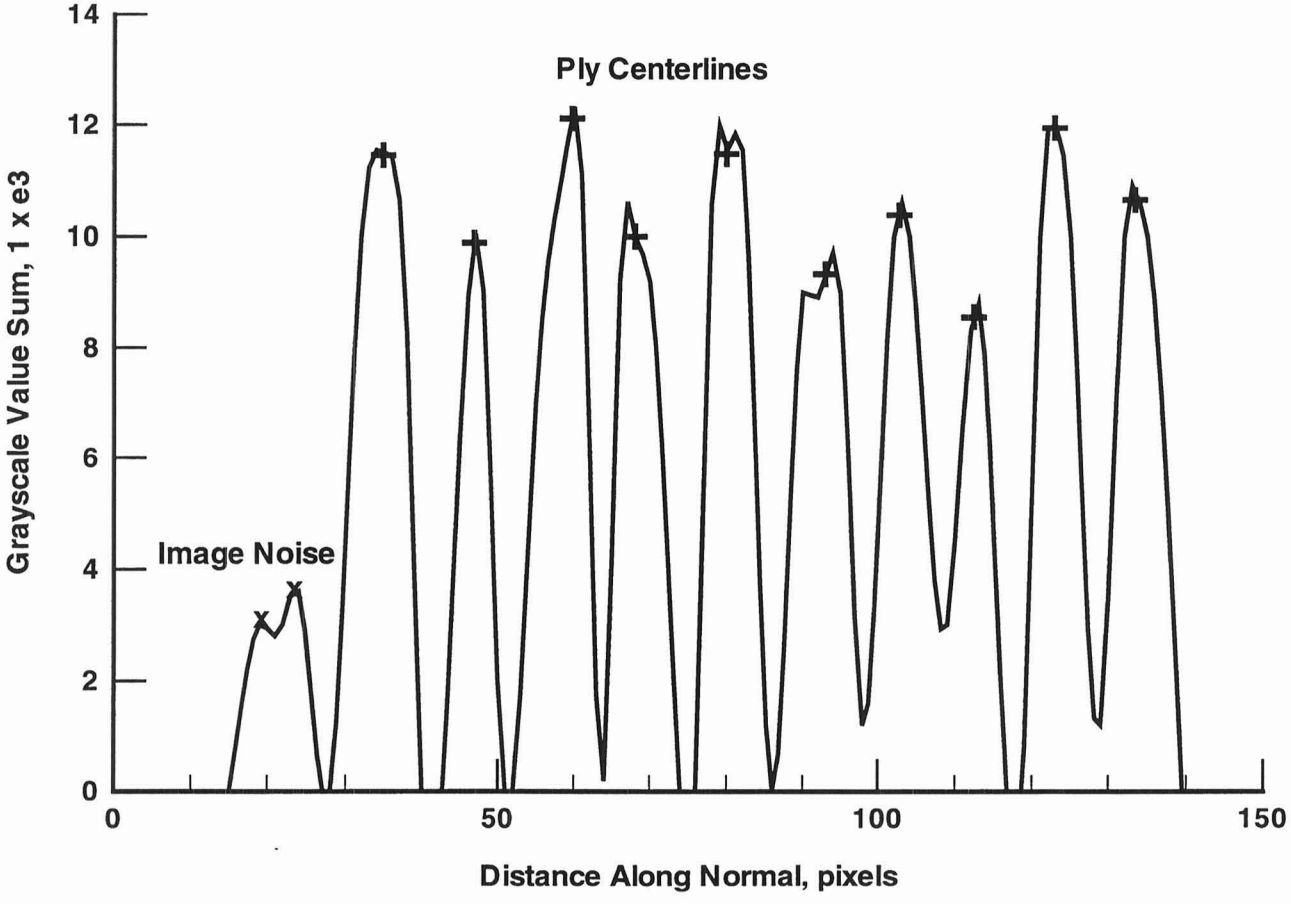

Figure 5

DETERMINATION OF CORD-END SPACINGS

In a similar manner, cord-end spacings can also be obtained for the plies determined at each of the points along the tire meridian. Since the plies are oriented at an angle to the cross-section, projections of the actual spacings are calculated. At each of the ply centerlines, the pixel grayscale values are plotted for the fixed distance on both sides of the normal. The peaks are chosen as the cord-ends and plotted on the image. Inaccurate cord-ends can again be deleted or new ones added with mouse clicks on the image. Since the cord-ends will be calculated to lie on a given line, an option to choose the line is provided. Besides the inner surface, the outer surface, or a smooth transition between the two, a straight line may alternatively be specified as the ply direction by making mouse clicks on each side of the normal shown on the image. The cord-end spacing is determined as an average distance between cord-ends. Figure 6 shows four cord-ends for the second ply of Figure 5, as determined from peaks in the grayscale values, marked by crosses on a slightly enhanced image.

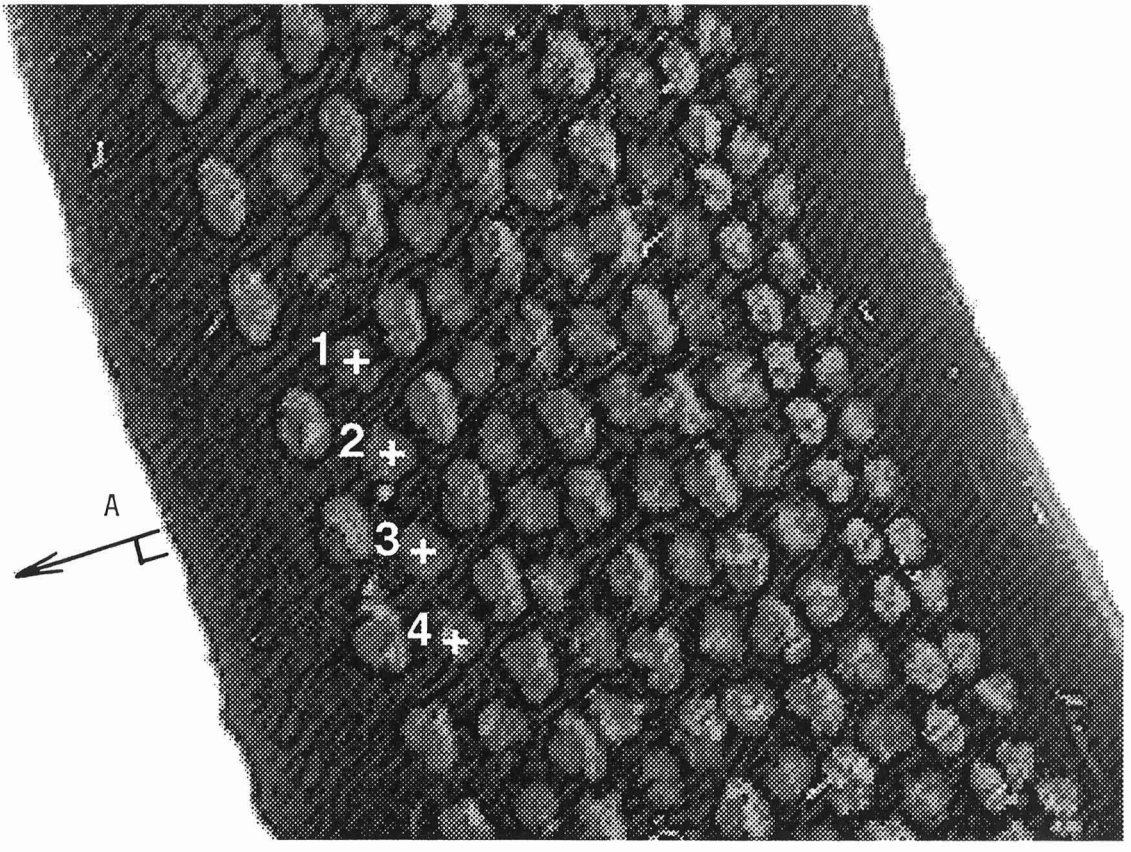

Figure 6

SUMMARY

A semi-automated procedure was described for the accurate determination of geometrical characteristics using a scanned image of the tire cross-section. The procedure is useful for cases when CAD drawings are not available or when a description of the actual cured tire is desired. In general, the automated features are not entirely adequate and the program will therefore require some user intervention. Although accurate cross-sectional details are automatically determined most of the time, the ultimate control of each detail is given to the user. For efficient use of the automation algorithms, the user also has continuous access to the parameters that control them. The calculated geometry is plotted on the image to ensure accuracy. If necessary, details can then be modified with simple options available in the software. The software produces the following:

1. An accurate determination of the cross-sectional geometry of an actual tire
   a) B-splines for the perimeter shape
   b) Ply centerline locations
   c) Ply end counts

2. Simple user-friendly software using PV-Wave to display the images
   a) Menu driven
   b) Single user interface to execute separate modules
   c) Graphical display of calculated details on scanned image

3. A simple database that can be used to create finite element models, to merge with CAD systems, or to be manipulated for other purposes.

ACKNOWLEDGEMENTS

I gratefully acknowledge Susan Bowen of Computer Sciences Corporation, James Green of Moravian College, and Kathryn Stacy of NASA Langley for their significant contributions to the development of this software.

REFERENCES

1. K. Stacy, K. Severance, and B.A. Childers, Computer-aided light sheet flow visualization. *AIAA 24th Fluid Dynamics Conference* (Orlando, Florida), July 6, 1993.

2. H. Freeman, On the encoding of arbitrary geometric configurations. *IRE Trans. Electron Comput.*, EC-10, 260-268, (1961).

3. H. Freeman, Computer processing of line drawings. *Computer Surveys*, **6**, 55-97, (1974).

4. T. Pavlidis, A review of algorithms for shape analysis. *Comput. Graphics & Image Processing*, **7**, 243-258, (1978).

5. T. Pavlidis, Algorithms for shape analysis of contours and waveforms. *IEEE Trans. Pattern Analysis and Machine Intelligence*, PAMI-2, 301-312, (1980).

MSC Products for the Simulation of Tire Behavior

John C. Muskivitch
The MacNeal-Schwendler Corporation
Santa Clara, CA

MSC PRODUCTS FOR THE SIMULATION OF TIRE BEHAVIOR

John C. Muskivitch
The MacNeal-Schwendler Corporation
Santa Clara, CA

INTRODUCTION

The modeling of tires and the simulation of tire behavior are complex problems. The MacNeal-Schwendler Corporation (MSC) has a number of finite element analysis products that can be used to address the complexities of tire modeling and simulation. While there are many similarities between the products, each product has a number of capabilities that uniquely enable it to be used for a specific aspect of tire behavior.

- **MSC/NASTRAN** - General purpose finite element program for linear and nonlinear static and dynamic analysis.
- **MSC/ABAQUS** - Nonlinear statics and dynamics finite element program.
- **MSC/PATRAN AFEA (Advanced Finite Element Analysis)** - General purpose finite element program with a subset of linear and nonlinear static and dynamic analysis capabilities with an integrated version of MSC/PATRAN for pre- and post-processing.
- **MSC/DYTRAN** - Nonlinear explicit transient dynamics finite element program.

TIRE CHARACTERISTICS AND GEOMETRY

Tires are very complex structures that have fairly simple overall geometry, but have complicated cross-sections (Figure 1). In their operating environment tires are subjected to varying types and magnitudes of loads. Some of the important aspects of tire behavior can be summarized as:

- Tire Footprint and Contact Area
- Dynamics (landing, curb impact, etc.)
- Cornering Loads
- Vibration
- Hydroplaning
- Interaction with Road Surface

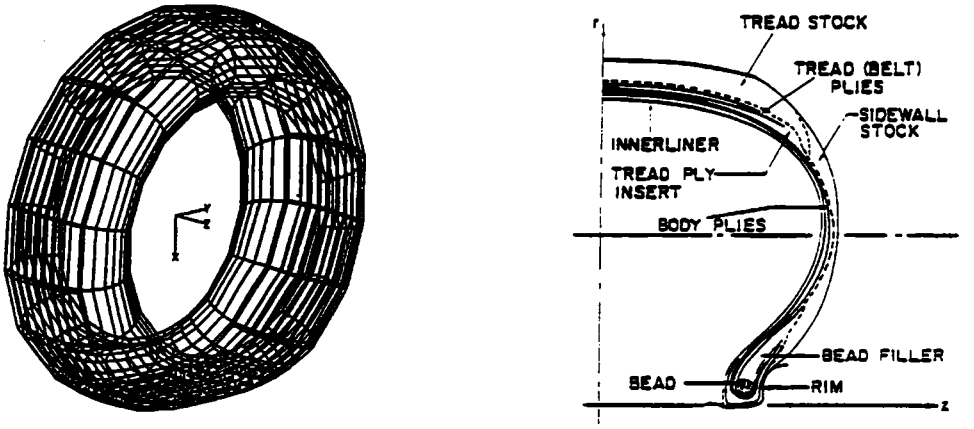

Figure 1. Typical Tire Geometry and Cross Section Detail

IMPORTANT ASPECTS IN SIMULATING TIRE BEHAVIOR

There are many important aspects of tire behavior which must be considered in a tire simualtion:

- Contact and Friction
- Material Constitutive Models (Linear and Nonlinear Behavior)
- Geometric Nonlinear Behavior
- Complex Preloads and Force Distributions
- Fluid-Structure Interaction
- Interaction with System Model

Both the variations in the behavior and the complexity of the tire's environment make it difficult for any one finite element analysis program to analyze all of the situations. The following discussion will outline each of the MSC product's capabilities with emphasis on tire modeling and simulation.

MSC/NASTRAN CAPABILITIES

MSC/NASTRAN Version 68:

- library of finite elements (scalar, 1-D, 2-D, 3-D, rigid, etc.)
- h and p elements
  - can be used in same model
- analysis capabilities:
  - linear static analysis
  - normal modes analysis
  - linear buckling analysis
  - transient and frequency response
  - nonlinear static and transient dynamics
  - complex eigenvalue analysis
  - steady state and transient heat transfer (linear and nonlinear)
  - superelement analysis
  - aeroelastic analysis
  - multidisciplinary design sensitivity and optimization
- linear, nonlinear and hyperelastic materials
- isotropic, orthotropic, and anisotropic materials
- numerous performance enhancements
- open architecture - interfaces to CAD and modeling systems
- available on PCs, workstations, and supercomputers
- fully documented and QA'd
- on-line documentation

EXAMPLES OF TIRE SIMULATION USING MSC/NASTRAN

For tire simulation MSC/NASTRAN's layered composite plate elements are widely used to model the ply lay-up. The slide line contact and gap elements simplify the contact and footprint characterizations (Figure 2).

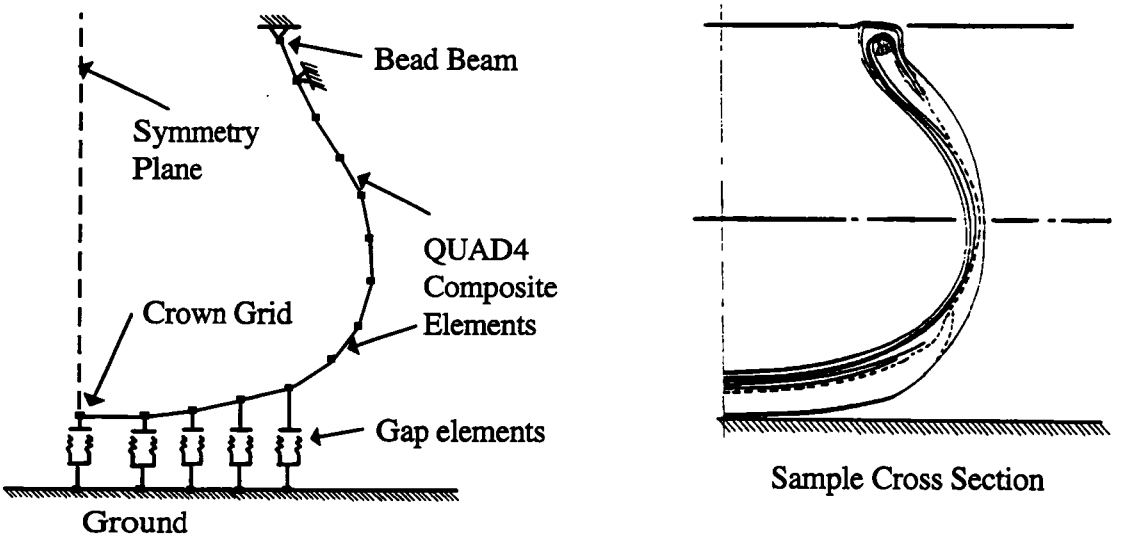

Figure 2. Sample Tire Model

EXAMPLES OF TIRE SIMULATION USING MSC/NASTRAN

Geometric and material nonlinearities are an important part of a tire simulation. The internal pressure preload in a tire affects its dynamic characteristics. The stiffening effects of a spinning tire can also be of importance. MSC/NASTRAN's geometric and material nonlinear capabilities can be used to include initial stress or preload conditions into a modal analysis.

Once the initial internal pressure, wheel rim mounting loads and vertical load have been applied, the effects of applied lateral forces and cornering loads can be characterized. Figure 3 shows a cross section of a tire-wheel assembly subjected to a lateral force.

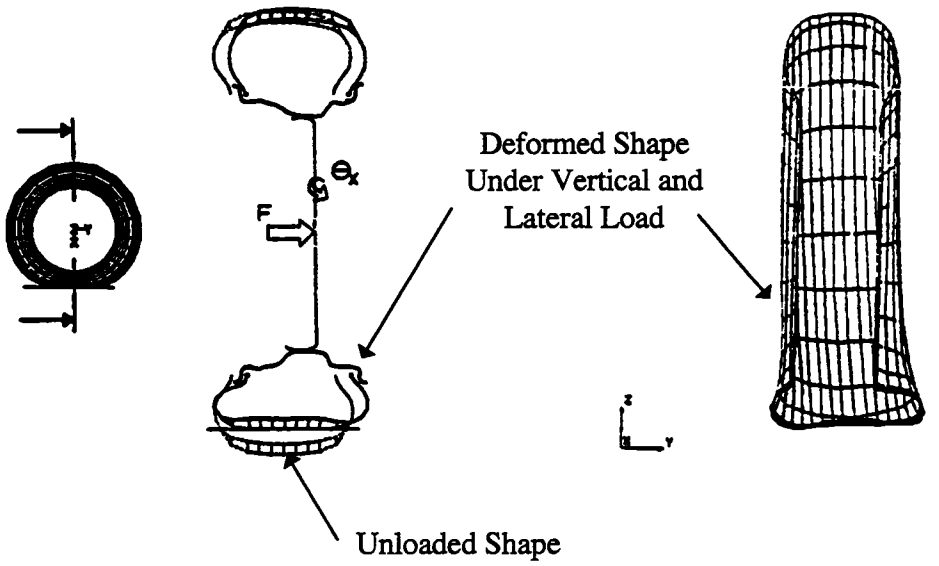

Figure 3. Tire - Wheel Assembly Subjected to Lateral Force

EXAMPLES OF TIRE SIMULATION USING MSC/NASTRAN

Figure 4 shows a close-up of the displaced shape of a tire cross section, first subjected to vertical load, and then subjected to a lateral force. The effects of contact area and friction force can be determined using these types of models.

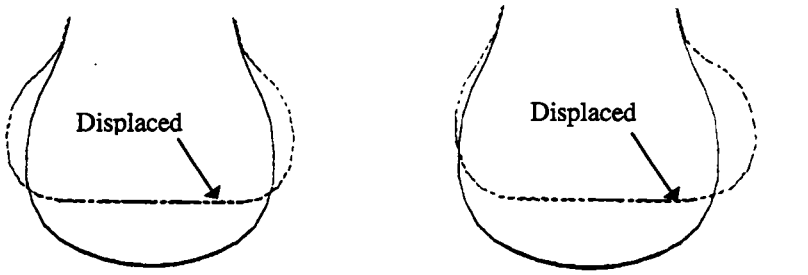

Figure 4. Displaced Shapes of Tire Cross Sections

ADDITIONAL FEATURES OF MSC/NASTRAN

MSC/NASTRAN has the following additional features for tire simulation:

- automatic time stepping in linear and nonlinear transient analyses.
- automatic load stepping in nonlinear statics.
- adaptive gap element
- slide line contact
- multidisciplinary design sensitivity and optimization
  - Simultaneous multiple loadings
    - * static loads
    - * modal results
    - * dynamic results
  - design constraints
    - * stress, displacement, natural frequency, etc.
  - physical properties as Design variables
    - * plate thickness, composites ply thicknesses and orientation angles, etc.
- DMAP (Direct Matrix Abstraction Program) programming language
- superelement analysis
- cyclic-symmetry analysis

TIRE SIMULATION WITH MSC/ABAQUS

MSC/ABAQUS

- powerful nonlinear static and dynamic analysis
- offered by MSC (agreement with Hibbitt, Karlsson, and Sorensen, Inc., HKS)
- specific capabilities to address the nonlinear characteristics of tire problems.
- nonlinear material models
- slide line, gap and special contact elements
- user routines for representing special materials
- special purpose elements for unique applications.

MSC/ABAQUS plate and solid Rebar elements (Figure 5)

- initially developed for modeling reinforced concrete
- easily adapted to tire problems
- ply cords can have multiple levels (plies), each with different properties and orientations.
- material properties can be nonlinear
- can be combined with other nonlinear (i. e., hyperelastic) materials that form the tire tread stock.

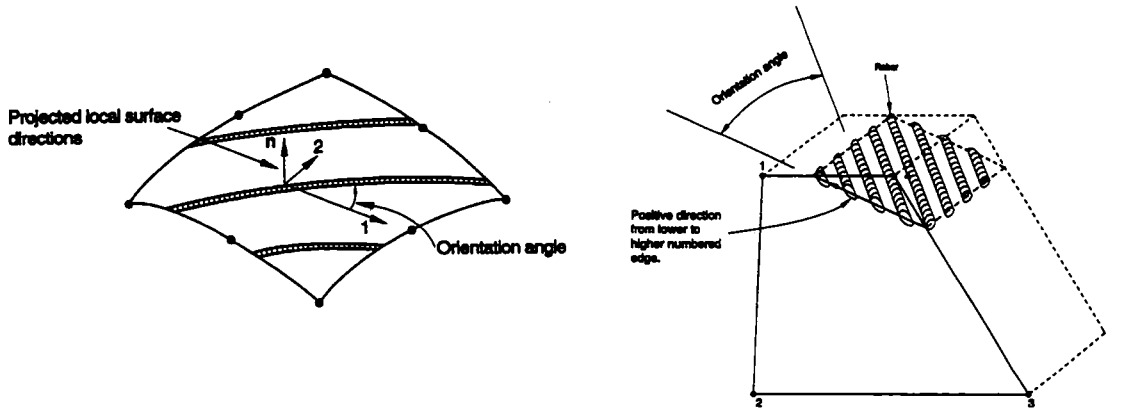

Figure 5. MSC/ABAQUS Rebar Elements

A number of MSC/ABAQUS's nonlinear analysis capabilities are included in **MSC/PATRAN Advanced Finite Element Analysis (AFEA).** AFEA is a powerful tool combining a subset of MSC/ABAQUS capabilities with MSC/PATRAN as the integrated graphical pre- and postprocessor.

MSC/DYTRAN FOR TIRE SIMULATION

MSC/DYTRAN

- highly nonlinear short duration transient dynamic analysis
- library of finite elements
  - scalar
  - 1-D
  - 2-D
  - 3-D
  - rigid
- Lagrange processor for structural applications
- Euler processor for modeling fluids
- special elements for fluid/structure coupling.
- explicit integration
  - short duration events (such as impact)
- complex general contact
- special elements
- nonlinear material models
- Input similar to MSC/NASTRAN
  - can use MSC/PATRAN and SDRC I-DEAS
- User routines for special conditions
- Link to MSC/NASTRAN for static or quasi-static initial conditions

MSC/DYTRAN FOR TIRE HYDROPLANING SIMULATION

Tire hydroplaning simulation (Figure 6):

- rotating tire
- specified velocity
- lowered into a fluid
- displacement condition - added to simulate a turning maneuver.
- different road surfaces were considered.
- coarse mesh used for demonstration purposes
- valuable insight into behavior
- production level analysis requires a finer mesh.

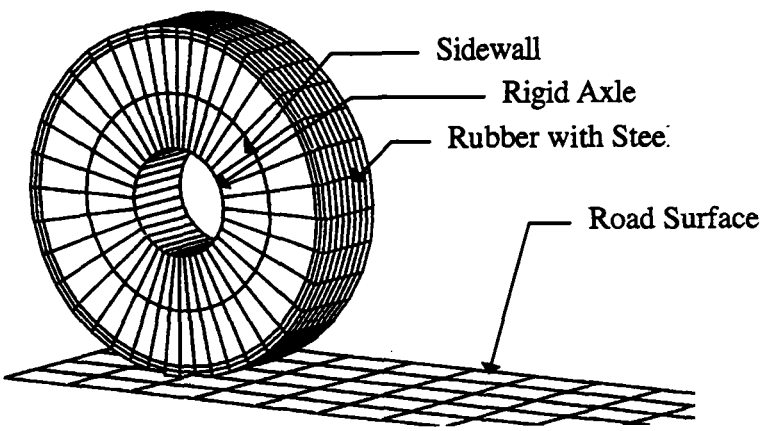

Figure 6. Tire Model

Tire model - Lagrangian elements
- Shell elements for tire sidewalls
- Solid elements for tread

Wheel - assumed rigid
- Set of rigid elements

Water model - Eulerian elements

The fluid region of the tire model is a combination of elements containing water and void elements. A cut-away view of the model is shown in Figure 7. As the tire moves through the water, the water will rise around the tire into the void elements of the Eulerian mesh.

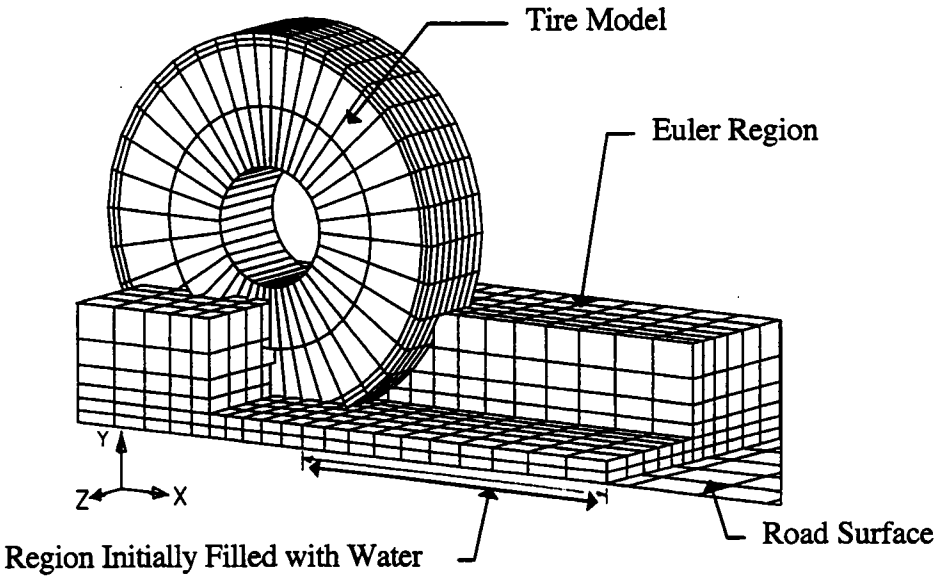

Figure 7. Cutaway View of Tire Fluid - Structure Model

MSC/DYTRAN FOR TIRE HYDROPLANING SIMULATION

As the simulation progresses, the water rises and lifts the tire off the road surface. MSC/DYTRAN's Euler processor enables the engineer to track the motion and pressure distributions of the fluid around the tire. In the simulation, water moves through the Euler mesh into areas of the mesh that were initially a void. Figure 8 shows sample fluid pressure contours superimposed on the fluid displaced shape.

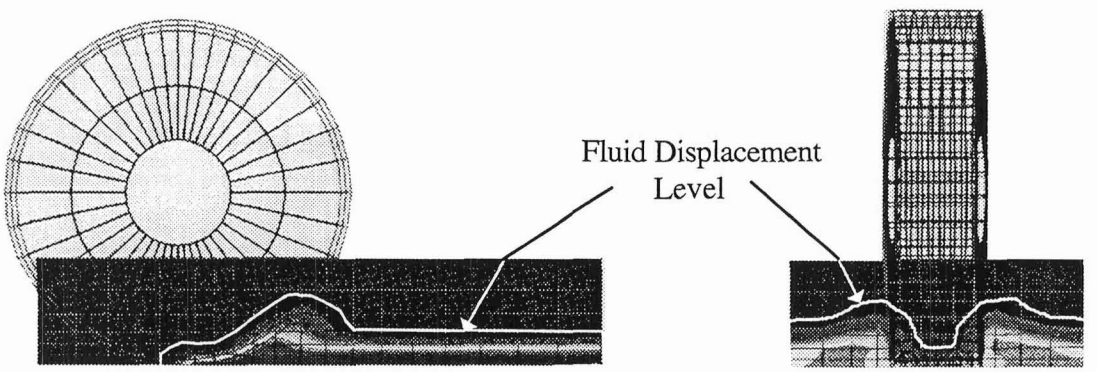

Figure 8. Sample Fluid Displacement and Pressure Contour Plots

The effect of the fluid forces lifting the tire off the road surface can be studied by plotting the time variation in the vertical deflection of a node at the center of the wheel (hub) as shown in Figure 9.

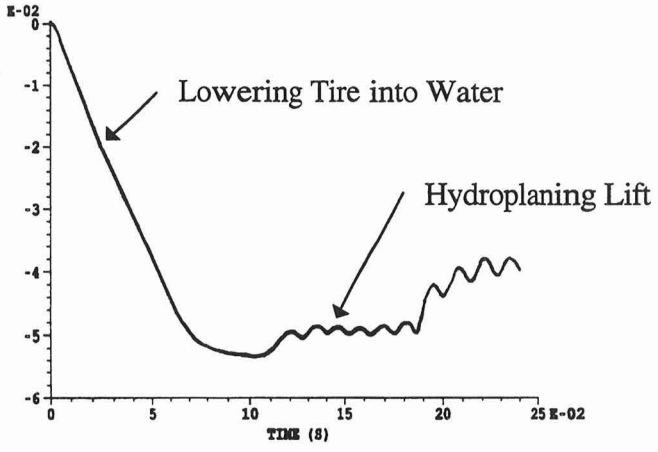

Figure 9. Time History Plot of Wheel Hub Vertical Deflection

SUMMARY

Tires are complex structures that experience a wide range of loadings under varied conditions during their service life. The MacNeal-Schwendler Corporation has many finite element based structural analysis products available (MSC/NASTRAN, MSC/ABAQUS, MSC/PATRAN AFEA, and MSC/DYTRAN) to address the many complex aspects of tire behavior. Many of the capabilities of these products can be uniquely applied to tire simulation. The availability of User routine customization is also possible to address special materials, special loads and special boundary conditions.

ANSYS Tools in Modeling Tires

Ashraf Ali and Michael Lovell
ANSYS, Inc.
Houston, PA

ANSYS TOOLS IN MODELING TIRES

Ashraf Ali
and
Michael Lovell
ANSYS, Inc.
201 Johnson Road
Houston, PA 15342-1300

INTRODUCTION

This presentation will provide a summary of the capabilities in the ANSYS program that relate to the computational modeling of tires. The power and the difficulties associated with modeling nearly incompressible rubber-like materials using hyperelastic constitutive relationships will be highlighted from a developer's point of view. The topics covered in this presentation will include: a hyperelastic material constitutive model for rubber-like materials, a general overview of contact-friction capabilities, and the acoustic fluid-structure interaction problem for noise prediction. Brief theoretical development and example problems will be presented for each topic.

POSSIBLE FACTORS AFFECTING TIRE MODELING

Some of the factors that directly and indirectly affect the design and analysis of tires are listed below. The ANSYS program has extensive capabilities in each of these areas. However, in this presentation, attention will be focussed on the material modeling of rubber and rubber–like materials. Specifically a hyperelastic material model will be studied. The ability of ANSYS to solve contact problems with friction will also be briefly summarized. Finally, since noise control is of particular interest to tire manufacturers, a brief overview of the ANSYS capabilities of solving acoustic fluid–structure interaction problems is given.

- Modeling of rubber or rubber–like materials – hyperelasticity ⇐
- Contact–Friction Capability
- Composite Materials
- Coupled Acoustic Analysis
- Coupled Thermal Analysis
- Other Design Tools, e.g., Design Optimization, APDL, etc.

Figure 2

MOONEY–RIVLIN HYPERELASTIC MATERIAL MODEL

The ANSYS program offers the Mooney–Rivlin hyperelastic material model to characterize rubber and rubber–like materials. This material model is suitable for capturing incompressible and nearly–incompressible behavior of rubber–like materials. Up to nine material constants can be used to define the strain energy density stored in a material. These constants are derived from laboratory tests on rubber specimens. A procedure for automatically determining these constants from experimental data will be discussed later. The Mooney–Rivlin hyperelastic material law is available with the ANSYS elements HYPER56 (4–noded quadrilateral), HYPER58 (8–noded brick) and HYPER74 (8–noded quadrilateral).

- Mooney–Rivlin is a material option applicable to incompressible rubber or rubber–like materials. Two, five, or nine material constants are used to describe the material behavior.

- If the Mooney–Rivlin constants for a material to be analyzed are known, the hyperplastic constants are input into ANSYS with the **TB** and **TBDATA** commands. If the Mooney–Rivlin constants are unknown for a rubber material, they can be derived from laboratory test data and directly sent to ANSYS using the ***MOONEY** command. The procedure for determining the constants from test data will be discussed later.

- The Mooney–Rivlin option is available with the incompressible elements HYPER56, 58, and 74. Up to six temperature–dependent sets of Mooney–Rivlin constants may be implemented.

Figure 3

MOONEY–RIVLIN STRAIN ENERGY DENSITY FUNCTIONS

The strain energy density function of Mooney–Rivlin materials is normally expressed as a function of the invariants, I_i , of the right Cauchy–Green tensor, **C**, and a number of constants. In order to separate the distortional and dilatational parts of deformation, a set of reduced invariants (defined in the next transparency), J_i, are used in place of the original invariants, I_i. The constant $\varkappa$ is the bulk modulus of the material and is specified through the Poisson's ratio ν. The value of $\varkappa$ controls the degree of incompressibility of the materials. At $\nu = 0.5$, $\varkappa$ is infinity and the material is fully incompressible. A value of ν, very close to 0.5, viz., 0.4999, can be used in the program to model nearly incompressible rubber–like materials. Up to nine constants are allowed and up to six temperature–dependent sets of constants may be input. This representation of the strain energy density function can handle up to 400% strains as long as the element distortions are of acceptable limits.

For the elements HYPER56, HYPER58, and HYPER74, the two, five and nine parameter Mooney–Rivlin models are available. The strain energy density function for these elements is given in polynomial form by:

$$W = \sum_{K+L=1}^{N} a_{kL} (J_1 - 3)^k (J_2 - 3)^L + 1/2\kappa (J_3 - 1)^2$$

where a_{kL} = the constants of the nine–parameter cubic Mooney–Rivlin relationship

$$\varkappa = \frac{2(a_{10} + a_{01})}{(1-2\nu)} = \text{bulk modulus}$$

Setting N=3 in the polynomial Mooney–Rivlin strain energy density expression, we obtain the nine parameter Mooney–Rivlin model:

$$W = a_{10} (J_1 - 3) + a_{01} (J_2 - 3) + a_{20} (J_1 - 3)^2 + a_{11} (J_1 - 3)(J_2 - 3)$$
$$+ a_{02} (J_2 - 3)^2 + a_{30} (J_1 - 3)^3 + a_{21} (J_1 - 3)^2 (J_2 - 3)$$
$$+ a_{12} (J_1 - 3)(J_2 - 3)2 + a_{03} (J_2 - 3)3 + 1/2\,\varkappa(J_3 - 1)2$$

Note that analogous two and five parameter models are obtained by respectively setting N=1 and N=2 in the polynomial expression. The last term in the model represents the hydrostatic (volumetric) work.

Figure 4

REDUCED OR VOLUME–FILTERED INVARIANTS

Figure 5 defines the reduced invariants, J_i, in terms of the original invariants, I_i, of the right Cauchy–Green tensor. Note that the invariants are being scaled by the determinant of the deformation gradient, det (**F**) = J_3, which also represents the change of volume of the material. In the hyperelastic formulation, ANSYS uses the total Lagrangian approach in which the original coordinate system is always used as the frame of reference. The energy conjugate in this case is: (**C:S**), where **S** is the second Piola–Kirchhoff stress. The strain **C** and the stress **S** are transformed internally and the results are presented in terms of Hencky strain and true stress.

$$J_1 = I_1 I_3^{-1/3}$$

$$J_2 = I_2 I_3^{-2/3}$$

$$J_3 = \text{Det } (\mathbf{F}) = I_3^{1/2}$$

where: **F** = Deformation Tensor

I_1, I_2, I_3 = Invariants of right Cauchy–Green tensor $\mathbf{C} = \mathbf{F}^T\mathbf{F}$

Figure 5

INCOMPRESSIBILITY

Rubber–like materials undergo large deformations with small changes in volume. The incompressible or nearly incompressible behavior of hyperelastic materials becomes more and more pronounced as Poisson's ratio, ν, approaches 0.5. The incompressibility condition must be accounted for in the element formulation so that the element exhibits proper behavior under loading. Correct treatment of the incompressibility condition in the element formulation not only prevents the element from locking under certain loading and boundary conditions, but also enhances the convergence characteristics of the element.

- Rubber–like materials undergo volume–preserving deformations.

- If Poisson's ratio ν is close to 0.5 for hyperelastic materials, then this incompressibility condition must be accounted for in the element formulation.

Figure 6

INCOMPRESSIBILITY EQUATION

The hyperelastic elements in the ANSYS program use extra pressure degrees of freedom in an attempt to satisfy the incompressibility condition. An augmented strain energy density function with the pressure appearing explicitly is used instead of the original energy function. The constraint condition, which is shown below, is satisfied over an element in an average sense. Since J_3 represents the volume change of an element derived from its displacements, and $\hat{J}_3$ is the volume change derived from its computed pressure, it follows that the integrated volume change over an element would be maintained approximately at zero.

The hyperelastic elements use pressure DOFs by augmenting the potential energy equation with:

$$\int \{N_p\}^T (J_3 - \hat{J}_3)\, dV = 0$$

$\{N_p\}$ are the pressure shape functions

J_3 is the volume change from the displacements

$\hat{J}_3$ is the volume change from the computed pressure

$J_3 = \det(\mathbf{F})$

$$\hat{J}_3 = 1 + \frac{\hat{p}}{\kappa}$$

κ = bulk modulus and $\hat{p}$ = computed pressure

Figure 7

ELEMENT STIFFNESS MATRIX

The element stiffness matrix equation for an element is shown below. The pressure degrees of freedom (dof), which are not assigned to any node, are eliminated at the element level. Therefore, the second equation, which is in terms of the displacements only, is sent out for assembly and solution. The meanings of the symbols in Figure 8 are: K_{uu} = stiffness sub–matrix corresponding to the displacement dof, K_{pp} = stiffness sub–matrix corresponding to the pressure dof, K_{pu} = stiffness sub–matrix corresponding to the coupled displacement and pressure dof, Δu = incremental displacement, Δp = incremental pressure, F^{app} = applied external loads, $F^{nr}{}_u$ = Newton–Raphson restoring force corresponding to the displacement dof, $F^{nr}{}_p$ = Newton–Raphson restoring force corresponding to the pressure dof, $\hat{K}$ = final element stiffness matrix modified by the condensation of Δp, and $\hat{F}^{nr}$ = final Newton–Raphson restoring force corresponding to the displacement dof modified by the condensation of Δp.

This leads to an equation of the form

$$\begin{bmatrix} K_{uu} & K_{pu} \\ K_{pu} & K_{pp} \end{bmatrix} \begin{Bmatrix} \Delta u \\ \Delta p \end{Bmatrix} = \begin{Bmatrix} F^{app} \\ 0 \end{Bmatrix} - \begin{Bmatrix} F_u^{nr} \\ F_p^{nr} \end{Bmatrix}$$

In all cases, the pressures are interpolated as "nodeless" variables, allowing the equation to be condensed to displacement DOF only:

$$[K]\ \{\Delta u\} = \{F^{app}\} - \{\hat{F}^{nr}\}$$

Figure 8

A FAMILY OF ANSYS HYPERELASTIC ELEMENTS

As mentioned earlier, ANSYS offers a family of elements that use the Mooney–Rivlin hyperelastic constitutive model. HYPER56 is a 4–noded quadrilateral element with one pressure dof, HYPER74 is an 8–noded quadrilateral element with three pressure dof, and HYPER58 is an 8–noded brick element with one pressure dof. The users are not concerned with the "nodeless" pressure dof which are eliminated at the element level. Furthermore, the 8–noded quadrilateral is actually a 9–noded Lagrangian element. The mid–side node is eliminated at the element level. Note that the pressure is interpolated using shape functions that are one order lower than the displacement shape functions.

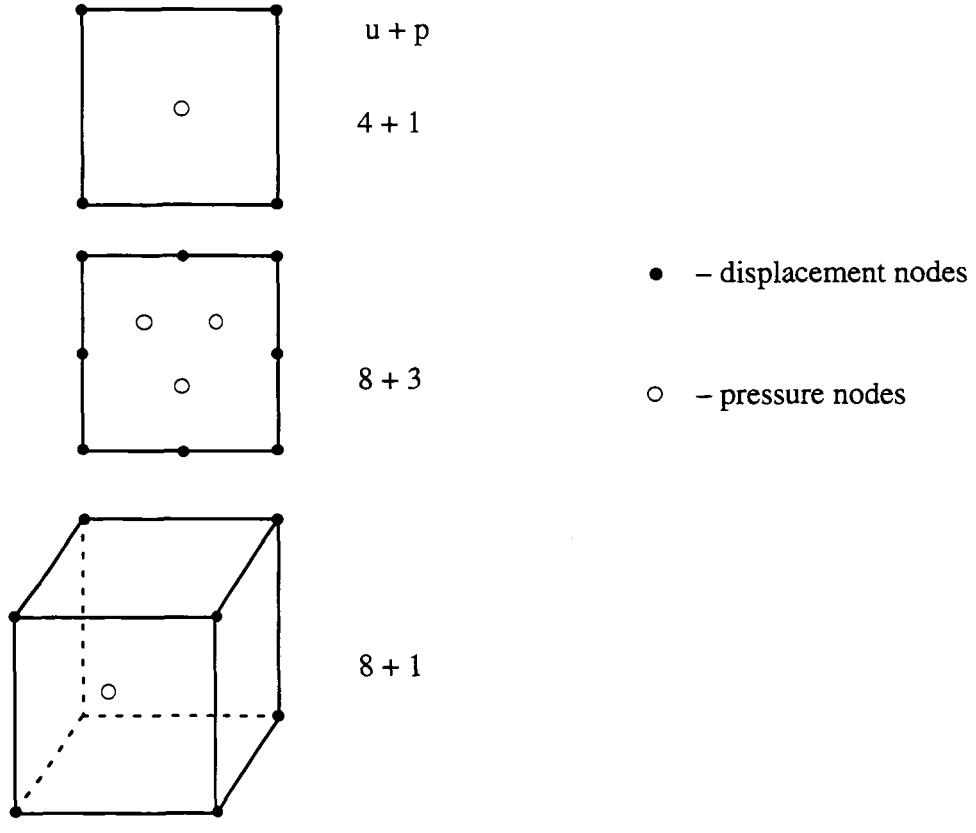

Figure 9

MOONEY–RIVLIN CONSTANT DETERMINATION

The hyperelastic constitutive models are empirical in nature. The Mooney–Rivlin model is given in polynomial form in terms of the strain invariants and a number of unknown material constants. One of the difficulties of using the Mooney–Rivlin model is the uncertainty associated with ascertaining the values of the unknown constants. These material constants cannot be chosen arbitrarily; they should satisfy the constraints listed in Figure 10. If one or more of the constraints are violated, the program issues warning messages. The constraints are usually violated when insufficient experimental data was used to derive the constants. As long as the analysis is within the strain range of the test data and undergoes the same mode(s) of deformation (e.g., uniaxial tension), then the constraints may be violated without affecting the solution accuracy. If the constraints are violated and the model experiences modes of deformation which there is no experimental data for, then convergence difficulties may be encountered. In this case, the results should be carefully validated.

The material constants are not arbitrary, but must satisfy certain constraints in order to produce valid behavior in all modes of deformation. These constraints are imposed in order to maintain:

- Positive definiteness of the strain energy density function
- Stress is always positive (or negative) at the extremes of uniaxial deformation
- Stress is a continuous function of deformation

If any constraint is not satisfied, the program will issue a warning message.

Figure 10

PROCEDURE FOR DETERMINING MOONEY–RIVLIN CONSTANTS

Laboratory tests are performed on the representative rubber test specimens to obtain experimental stress–strain data. Uniaxial tension and compression tests are the most common, but equibiaxial tension, equibiaxial compression, and shear tests are also regularly performed. The ANSYS program takes input engineering stress–strain data and performs a least–square curve–fitting procedure to determine the Mooney–Rivlin constants of the hyperelastic strain energy density function. Experimental data from more than one test may be used to determine the Mooney–Rivlin constants. The user has the option of determining the constants without performing analysis or combining the constant determination with detailed analysis. The program automatically stores the Mooney–Rivlin constants in the ANSYS database, and a user specified data array, and writes them to an output file in typical ANSYS data table format.

- The Mooney–Rivlin constants for hyperelastic materials are not generally available in the open literature. Therefore, most sets of Mooney–Rivlin constants need to be derived from experimental stress–strain data.
- For hyperelastic materials, simple deformation test data can be used to accurately characterize the Mooney–Rivlin constants. The constants are determined by ANSYS using the ***MOONEY** command.
- Test data may come from one or more of the following six tests:
  - Uniaxial Tension – Equibiaxial Tension
  - Uniaxial Compression – Equibiaxial Compression
  - Planar Tension (Shear) – Planar Compression (Shear)

Figure 11

EXPERIMENTAL STRESS–STRAIN DATA

Figure 12 shows two sets of experimental data, one from a uniaxial tension test and the other from a uniaxial compression test. The data was obtained from experimental tests conducted on rubber specimens taken from the same stock. The stress–strain values are expressed in engineering form for practicality. The ANSYS program can determine Mooney–Rivlin hyperelastic material constants from experimental data obtained from any combination of the three independent modes of deformation: uniaxial tension, equibiaxial tension and planar tension (shear). By superimposing hydrostatic pressure to the loaded specimen, uniaxial compression tests can be shown to be equivalent to equibiaxial tension tests. Similarly, uniaxial tension data can be equated to equibiaxial compression data and pure shear (planar tension) data can be equated to planar compression data. It is noteworthy to mention that Mooney–Rivlin constants cannot be independently determined from shear test data alone; equations from another test, viz., uniaxial tension or equibiaxial tension, must also be considered with the shear test equations.

COMPRESSION DATA		TENSION DATA	
strain	stress*	strain	stress*
–.4968	–1345.74	.0024	5.13238
–.4708	–1174.01	.0142	15.39714
–.4430	–1020.92	.0317	28.22864
–.4162	–897.182	.0507	42.34296
...	...	.0685	56.45728
–.0415	–50.0036	.0840	71.85739
–.0356	–41.2488	.1012	83.40508
–.0297	–32.7781	.1184	94.95266
–.0247	–25.4332	.1353	105.21460
–.0197	–18.6461	.1528	115.48130
–.0155	–13.5637		
–.0121	–9.6072		
–.0088	–6.2189		
–.0054	–3.3988		
–.0037	–1.7047		
–.0020	–.2841		
* stress in psi			

Figure 12

PLOTS OF EXPERIMENTAL AND FITTED CURVE

After the constants have been determined, the user should plot the experimental data curve and the computed curve on the same frame in order to view the quality of the fit. Figure 13 shows such a plot. Since the two curves are coincident, it appears that the fit in this case was adequate. As a rule of thumb, the number of data points should be at least twice the number of constants requested in order to obtain a reasonable fit. For the present example, there were 42 data points for the compression test and 10 data points for the tension test. A nine–parameter curve was fitted. The coefficient of determination, which reflects how well the curve fits the input data, is also printed in the output file. The closer the value to unity, the better the fit. However, a value closer to unity does not necessarily imply that the curve is "good", only that it goes through the input points fairly well. The coefficient of determination for the present example was 0.9998. Another measure of the quality of the fit, the root–mean–square error, is also calculated and output. The root–mean–square error, expressed as a percentage, should be "close" to zero. Its value for this example was 8.53%.

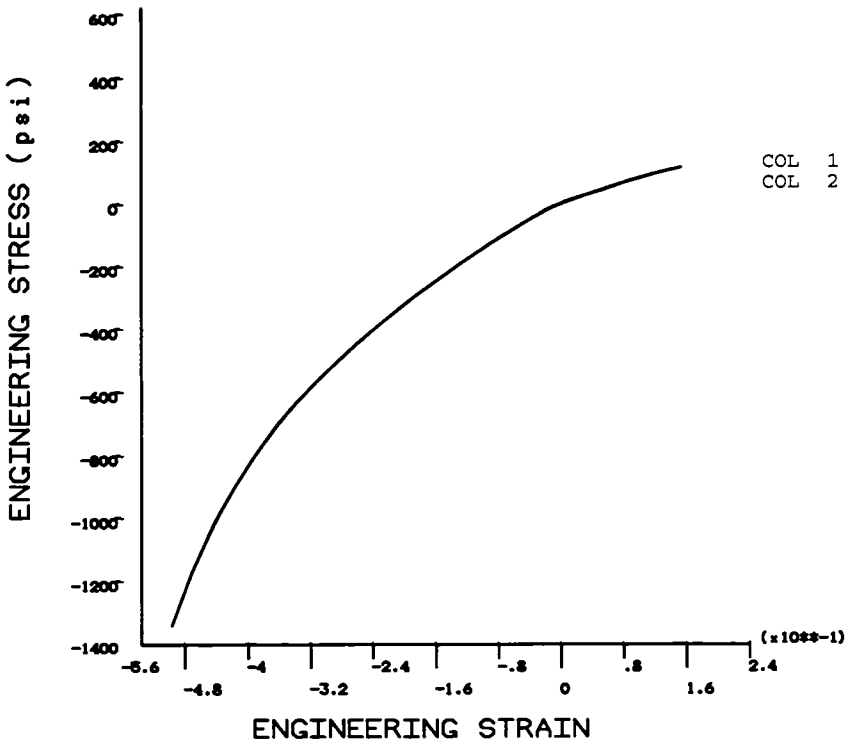

Figure 13

EVALUATING MOONEY–RIVLIN CONSTANTS

In graphing the calculated stress–strain curve in the ANSYS program, it is possible to extend the displayed curve into regions that were not defined by the experimental data. Graphing the curves over such an extended range can help the user qualitatively understand the model's behavior if its response ever happens to exceed the range of the experimental strain. It should be noted that a uniaxial tension curve should be graphed only in regions of positive strain, and a uniaxial compression curve only in regions of compressive strain. A good practice usually requires that the test data represent all modes of deformation and ranges of response experienced by the model.

- In order to evaluate the calculated constants between the data points or to analyze the stress–strain behavior outside the range of test data, the ***Evaluate** command should be used.
- To establish if there are any spurious inflections in the calculated stress–strain curve between data points, the determined Mooney–Rivlin constants should be evaluated in at least 10 times the number of data points.
- When extrapolation from the data points in a hyperelastic model is necessary, the ***Evaluate** command should always be used to verify expected material behavior.

Figure 14

PLOT OF EVALUATED STRESS–STRAIN CURVE

Figure 15 shows a portion of the calculated stress–strain curve that goes beyond the range of input data. The range of input data for this example lies in the middle part of the graph which is extended in the tension region. In the tension region, beyond the range of input data, the material is expected to exhibit a brief plateau followed by a stiff strain–hardening behavior. This knowledge may become important in the interpretation of results of an analysis in which parts of the model experienced tensile strains in this range.

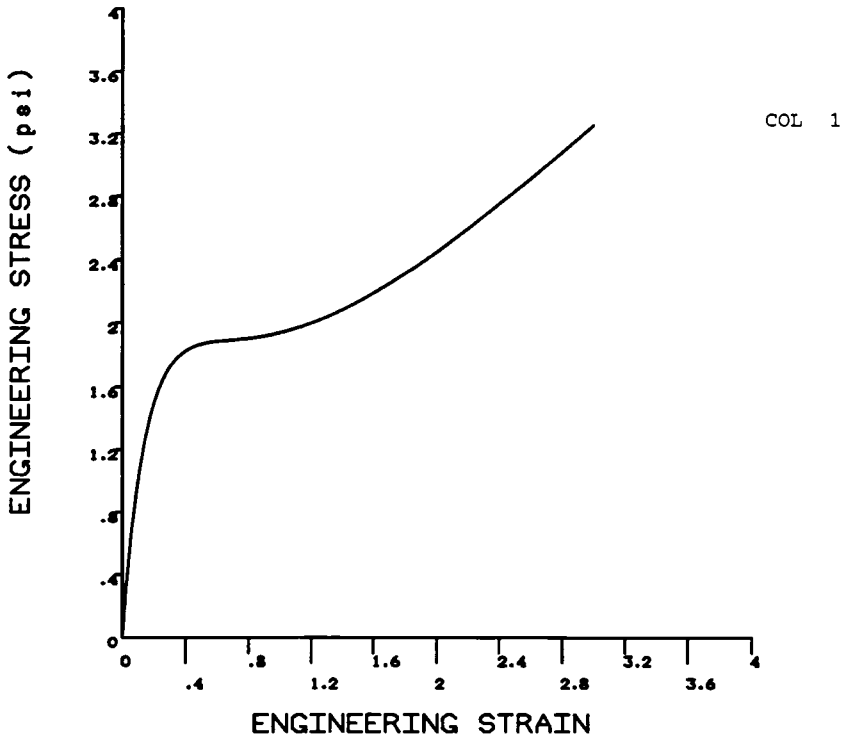

Figure 15

INCOMPRESSIBILITY: LOCAL AND GLOBAL B–B CONDITIONS

For a mixed formulation with displacement and pressure dofs, finite elements can be developed that satisfy the so–called Brezzi–Babuska (B–B) inf–sup condition. The finite elements that satisfy the Brezzi–Babuska condition are not expected to lock at the element level. However, the satisfaction of the B–B condition at the element level does not always guarantee a lock–free behavior at the global level. A problem with a certain set of boundary and loading conditions can always be created under which the problem will exhibit a locking behavior. Figure 16 gives guidelines for a proper mix of displacement and pressure dof in a model. Also, the analyst should watch out for the occurrence of actual buckling in his problem.

Guidelines:

- ☞ two–dimensional Problems – No. of free $u_i \geq 2p_i$
- ☞ three–dimensional Problems – No. of free $u_i \geq 3p_i$

Also,

- ☞ Watch for real buckling

Figure 16

USER–DEFINED MATERIAL LAWS

Tire manufacturers may have their own material laws for describing rubber–type material behavior which are proprietary in nature. ANSYS provides user–programmable features, e.g., a hyperelastic user–routine, which allows direct input of personalized material constitutive laws into the program. The advantage of this procedure is that the extensive pre–processing, solution, and post–processing capabilities of ANSYS can be utilized without revealing a company's proprietary material constitutive model. Because of competition in the tire industry, the user–programmable features of ANSYS could prove very useful to the concerned companies.

If there is a need to simulate a material behavior that is not a program option, then the user may want to consider programming the material law himself.

A number of user–programmable features (UPFs) are offered for characterizing different types of material behavior.

The available user material routines include:

- Plasticity
- Hyperelasticity ⇐
- Creep
- Swelling

Figure 17

USER–PROGRAMMABLE ROUTINE FOR HYPERELASTIC MATERIAL

Figure 18 shows the structure of the hyperelastic user–routine. The routine provides the invariants of the right Cauchy–Green tensor, Poisson's ratio and problem dimensionality as the input. The user is required to compute the strain energy density, the pressure, the first and second derivatives of the strain energy density function and the pressure with respect to the invariants, and the bulk modulus. This structure not only provides the mechanism for writing an invariant–based hyperelasticity material law, but also a principal–stretch–based hyperelasticity material law. To write code for a constitutive law of the latter type: (1) compute the principal stretches using the invariants, (2) compute the first and second derivatives of the strain energy density function (which is now a function of the principal stretches) with respect to the principal stretches, and (3) transform the derivatives with respect to the principal stretches into those with respect to the invariants using a chain rule of differentiation.

Input quantities provided by the program:

1. $[I_1, I_2, I_3]$

2. Poisson's Ratio

3. Problem Dimensionality
[2 = two–dimensional, 3 = three–dimensional]

User responsibility is to compute:

1. W, $\frac{\partial W}{\partial I}$, $\frac{\partial^2 W}{\partial I^2}$

2. P, $\frac{\partial P}{\partial I}$, $\frac{\partial^2 P}{\partial I^2}$

3. κ = Bulk Modulus

Figure 18

SNAP–THROUGH OF A HYPERELASTIC BUTTON

As previously described, the ANSYS program allows hyperelastic materials to undergo realistic, large recoverable deformations. The geometry in Figure 19 depicts the buckling of a soft silicon rubber button that is used in a mouse to activate electrical impulses. The button, which was modelled using axisymmetric HYPER74 elements, actually 'snaps–through' as it moves from its initial to final configurations. The deformed shape demonstrates the hyperelastic element's ability to undergo extremely large strains, as is shown in the deepening folds which physically occur as the button displaces.

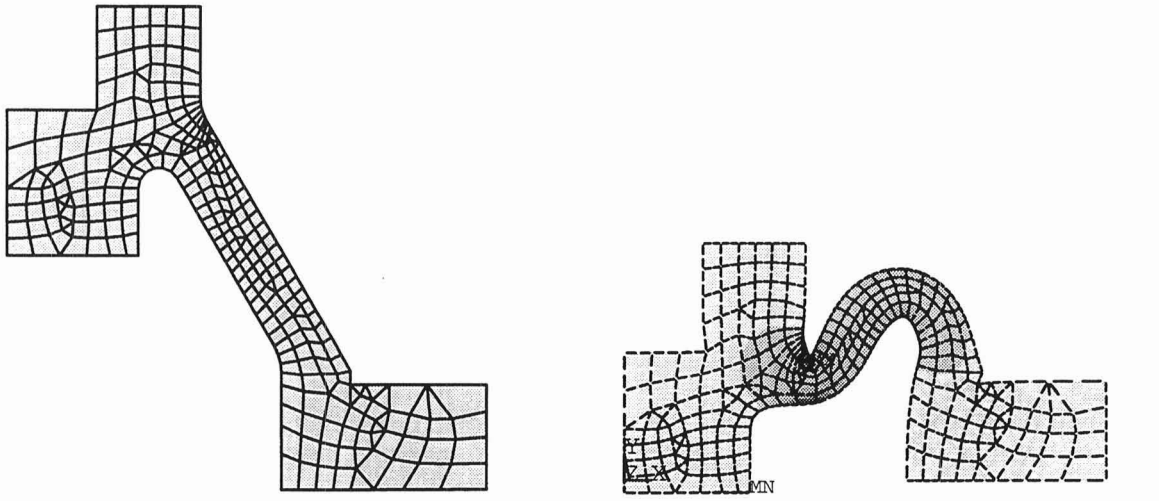

(a) Initial Geometry (b) Deformed shape with stress contour

Figure 19

PRESSURIZED AXISYMMETRIC O–RING

In order to demonstrate how hyperelastic materials can be used in conjunction with contact elements in ANSYS, a hyperelastic O–ring seated in a square groove is analyzed. The O–ring of solid circular cross–section is first forced to conform to the shape of a channel by installing an inner retaining ring against the O–ring. Pressure is then applied to the top surface of the O–ring. In the model, the O–ring is meshed with axisymmetric HYPER56 elements and the rectangular channel and moving retaining ring consist of two–dimensional spar (LINK1) elements. Two–dimensional point–to–surface contact elements (CONTAC48) are used to define contact between the O–ring and the spar elements. As expected, the analysis of the O–ring finds that the maximum stress occurs at the corners of the channels.

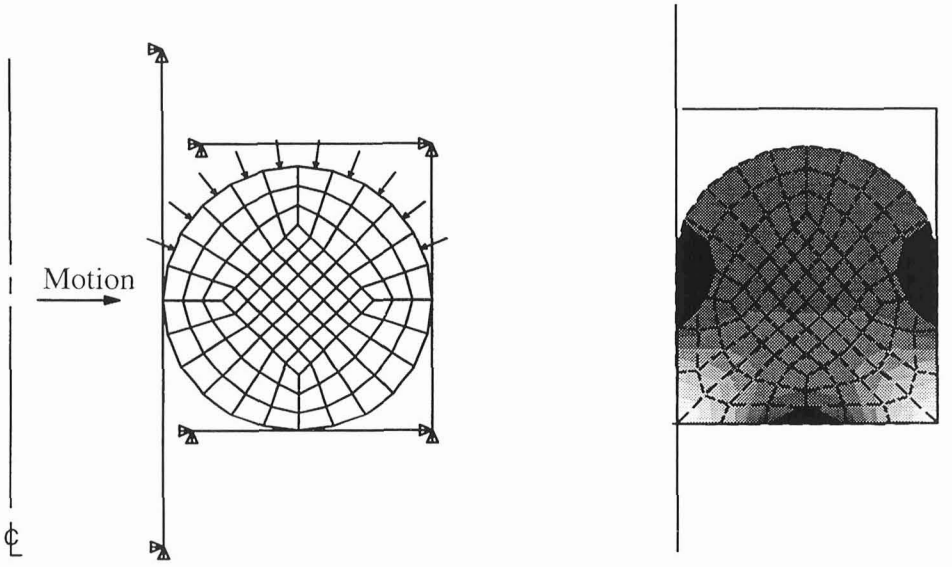

(a) Initial geometry (b) Deformed shape with hydrostatic stresses

Figure 20

GENERAL CONTACT CAPABILITIES

In the ANSYS program, node–to–node (nodal) contact is represented by elements CONTAC12, 52, and COMBINE40 while surface–to–surface (general) contact is represented by elements CONTAC26, 48, and 49. For nodal contact, the final points of contact must be known beforehand. In general surface contact, contact areas do not have to be known a priori and large sliding motions and deformations are permitted. In fact, almost all nonlinear options – plasticity, large strain, hyperelasticity, etc. – can be used in conjunction with general surface contact. Since the surface contact elements are defined using any pre–existing solid element (including shells) mesh, simple and complex planar, axisymmetric, and three dimensional configurations can be modelled with contact. In ANSYS, CONTAC26 and 48 are used to model two–dimensional and axisymmetric surface contact while CONTAC49 is used to define contact between three dimensional elements. Surface contact with midside–node elements is also allowable in ANSYS when additional steps are taken to alleviate non–uniform stiffness along mid–sided surface nodes. All three general surface contact elements can be used in static, dynamic, and thermal–structural analyses.

- In ANSYS, both point–to–point and general surface–to–surface contact elements are available. In all cases, friction may be included at the contact interface.
- The points or surfaces may be either rigid or deformable so that the component may come into contact with a rigid element or itself. Note that point–to–surface contact is a special case of surface–to–surface contact.
- Large deformations, plasticity, and other nonlinear effects can be used in conjunction with frictional contact.
- Planar, axisymmetric, and three–dimensional configurations (including shells) are allowed in contact analyses.
- Contact surface elements are defined using pre–existing element meshes so that complex surfaces can be easily represented.
- Static, dynamic, and coupled thermal–structural contact analysis options are available.

Figure 21

CONTACT SURFACE KINEMATICS

When using general surface contact elements, ANSYS performs a multi–level search for contact to increase program efficiency. Utilizing pinball regions whose radii are defined by the length of each contact plane, four levels of contact status are established. When a contact node is far from the contact plane well outside the pinball region, STAT=4. For such far field status, the contact algorithm is simple and utilizes minimal CPU time. For a node near the contact plane inside the pinball region, but out of contact, STAT=3. In this case, the contact algorithm is more complex and uses a modest amount of CPU. Once contact has been established between the nodes of two surfaces, a STAT value of 1 or 2 is given to the contact element. STAT=1 corresponds to a node being in contact and sliding while STAT=2 signifies a node being in contact and sticking. When contact occurs, the contact algorithm is very complex and uses a large amount of CP time.

The kinematics of contact deal with the position and motion of the contact nodes relative to the contact planes. In surface–to–surface contact analyses:

- A multi–level search procedure is performed in ANSYS to establish if contact has occured. In this procedure, a distinction between near–field and far–field states of contact is made using the pinball concept.

- Contact voids and overlaps are eliminated since ANSYS generates pseudo–contact elements around each contact plane in such a manner that each contact node is uniquely defined with respect to a target surface.

- Both symmetric and asymmetric contact analyses options are available.

Figure 22

SUMMARY OF CONTACT SURFACE ANALYSIS WITH FRICTION

The tangential sliding behavior of two contacting bodies in relative motion may be frictionless or may involve friction. Frictionless behavior allows the two bodies to slide relative to one another without any resistance. Including friction, however, causes shear forces to develop between the contact regions of the two bodies. ANSYS is capable of defining contact with and without friction. Frictionless contact is suitable in models whose components have low friction coefficients and develop minimal tangential forces. Two dry friction models are available in ANSYS for surface–to–surface contact: rigid and elastic Coulomb friction. Rigid Coulomb friction allows only a sliding friction condition where the contact areas do not consider sticking. Elastic Coulomb friction allows both sticking and sliding conditions. The sticking zone is treated as an elastic region in which the components in contact will return to their original geometry when the tangential force is removed. At forces above static friction, the components will slide inelastically relative to each other. Elastic Coulomb friction is valid for most engineering materials in contact. A user defined friction option is also available for modeling friction behavior which is dependent on velocity. This option is most commonly used for cases where fluid–film effects are important. Fluid–film effects are characterized by a change in the tangential friction force with an increase in contact surface velocity.

In ANSYS, four different friction models are available for general surface–to–surface contact:

i) frictionless contact behavior

ii) dry elastic Coulomb friction

iii) dry rigid Coulomb friction

iv) a user–friction capability that allows the influence of tangential velocity on the friction law.

Figure 23

ANALYSIS OF A HEADING PROCESS

To illustrate how contact elements can be used with other nonlinear analysis techniques, the heading process of a rivet was analyzed using ANSYS. In the analysis, an aluminum workpiece of circular cross section was press–fit into a steel grip die using a hemispherical heading tool. The workpiece, grip die, and heading tool were all modelled using axisymmetric PLANE42 elements. CONTAC48 elements, with the rigid Coulomb friction option, were used to simulate the contact between the workpiece, heading tool, and grip die. Since the workpiece undergoes large nonrecoverable deformations, plasticity was included in the model. As demonstrated by the deformed shape, the results of the analysis accurately predict that the maximum stress occurs along the corner of the grip die which the workpiece rolls over.

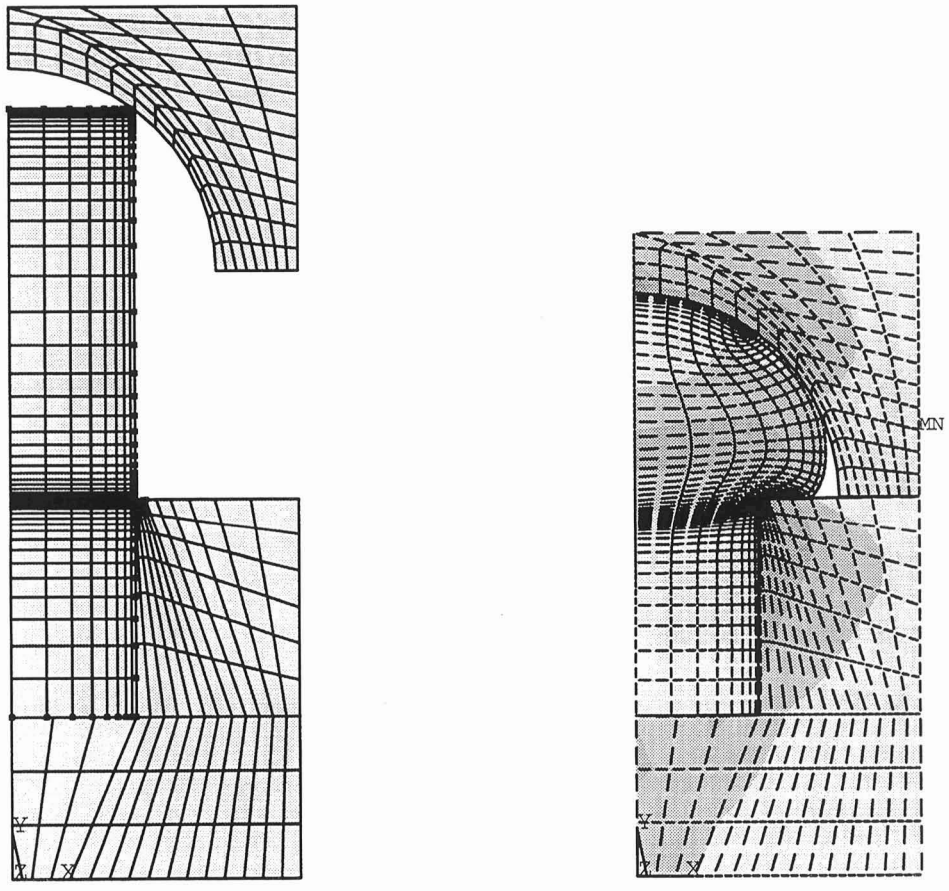

(a) Initial Geometry

(b) Deformed Shape With Stress Contour

Figure 24

TAPER SHAFT HEAT UP CONTENT

To demonstrate the coupled thermal–structural capabilities of ANSYS, the expansion of a heated tapered shaft is analyzed. A coupled thermal–structural analysis uses coupled field solids PLANE13, SOLID5, or SOLID98 elements. These elements have both thermal and structural degrees of freedom. Heat flow occurs in these elements when contact is established and the CONTAC48 or 49 elements have thermal–structural degrees of freedom activated. In the tapered shaft analysis which uses SOLID98 and CONTAC49 elements, both temperature and stress contours are plotted to demonstrate the thermal–structural coupling.

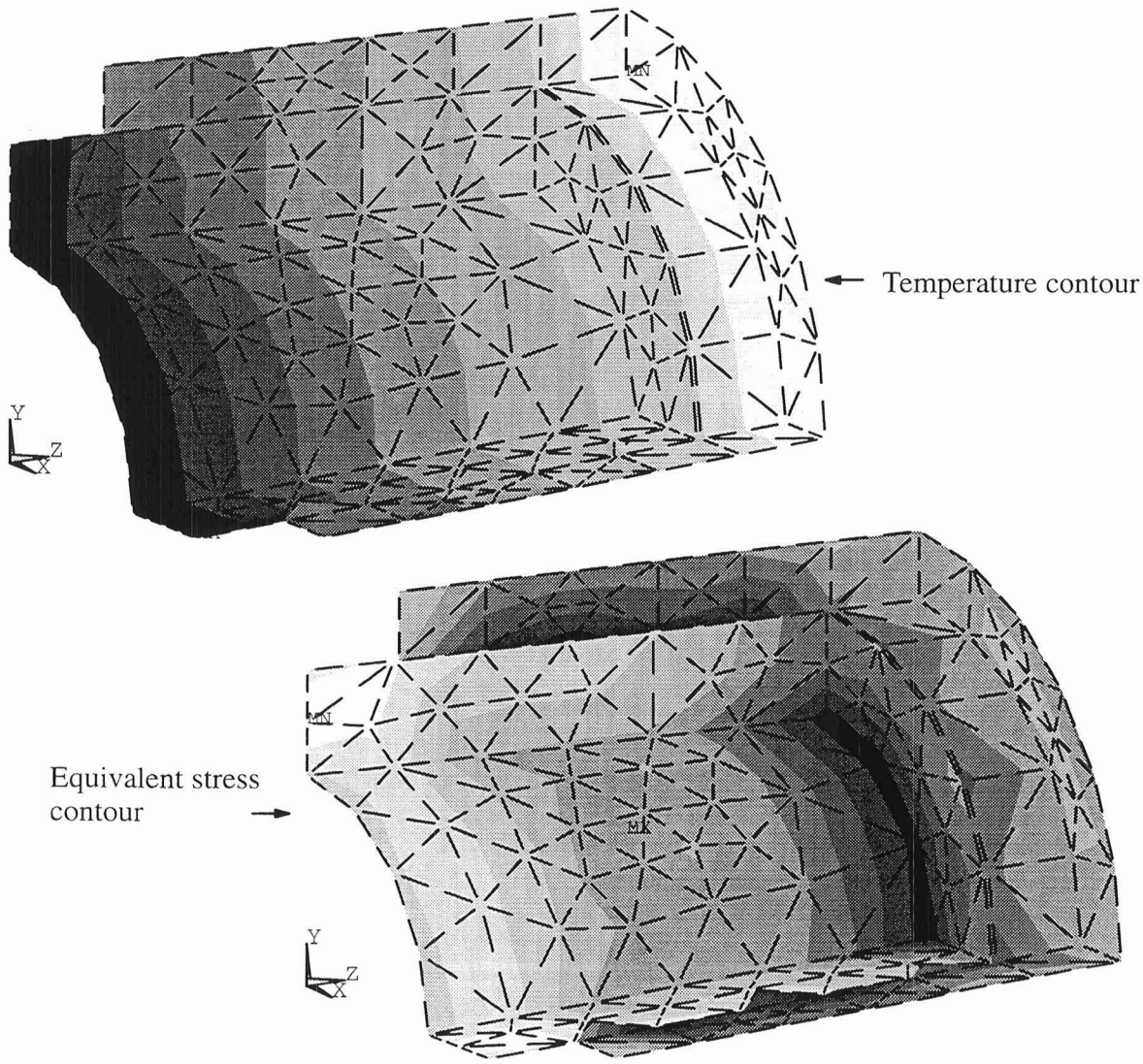

Figure 25

FLUID–STRUCTURE COUPLING

Noise prediction and control are also important considerations for the tire manufacturers. The ANSYS program has extensive capabilities for predicting pressure levels generated by vibrating structures or other sound sources. In order to solve for the pressure distribution generated by vibrating structures, the structural dynamic equations must be coupled to the acoustical fluid flow equations through the use of the momentum balance equation at the fluid–structure interface. Depending upon the nature of the excitation source, the problem can be solved in the time domain or in the frequency domain. The ANSYS program has separate acoustic absorption elements to model acoustic problems whose domain extends to infinity. If acoustic absorption elements are used, the domain is truncated at a finite distance and the absorption elements are placed at the truncated boundary.

- Dynamic Acoustic Fluid Equation

$$[K_f]\{p\} + [M_f]\{\ddot{p}\} = \int_S \frac{\partial p}{\partial n}\, ds$$

- Structural Dynamic Equation

$$[M_s]\{\ddot{u}\} + [C_s]\{\dot{u}\} + [K_s]\{u\} = \int_S N_i\, p\, ds + \{F_s\}$$

- Fluid–Structure Interface Condition

$$\frac{\partial p}{\partial n} = -\varrho_o \frac{\partial^2 u}{\partial t^2}$$

- Combining the Fluid–Structure Equations

$$\begin{bmatrix} M_s & O \\ \varrho_o R^T & M_f \end{bmatrix} \begin{Bmatrix} \ddot{u} \\ \ddot{p} \end{Bmatrix} + \begin{bmatrix} C_s & O \\ O & C_f \end{bmatrix} \begin{Bmatrix} \dot{u} \\ \dot{p} \end{Bmatrix} + \begin{bmatrix} K_s & -R \\ O & K_f \end{bmatrix} \begin{Bmatrix} u \\ p \end{Bmatrix} = \begin{Bmatrix} F_s \\ F_f \end{Bmatrix}$$

where:

R = coupling matrix

C_f = Fluid damping matrix at the boundary surface to account for sound absorption

ϱ_o = fluid density

Figure 26

PASSENGER CAR MODEL

A finite element model of an automobile body with seats is shown. The interior acoustic enclosure is modelled using three–dimensional acoustic fluid elements (FLUID30) and the car body is modelled using shell elements (SHELL63). The acoustic elements in touch with the enclosure walls are coupled with the structural shell element. The velocity of sound travelling through the air in the automobile enclosure is taken to be 13200 inches per second, and the density of air 0.0001958 pounds–second**2 per inch. Two vibrating panels, one on the driver's side and the other on the passenger's side, simulate loudspeakers of the automobile audio–system. A harmonic analysis is performed in which the loudspeakers are excited at a frequency of 40 hertz. The objective is to monitor the pressure levels at the locations of the riders's ears. A contour plot of the absolute pressure on the passenger side of the automobile compartment is shown. The analysis can be carried out at different operating audio frequency levels. The present analysis did not consider damping on the enclosure walls. Empirical damping values could be easily added to make the analysis more realistic.

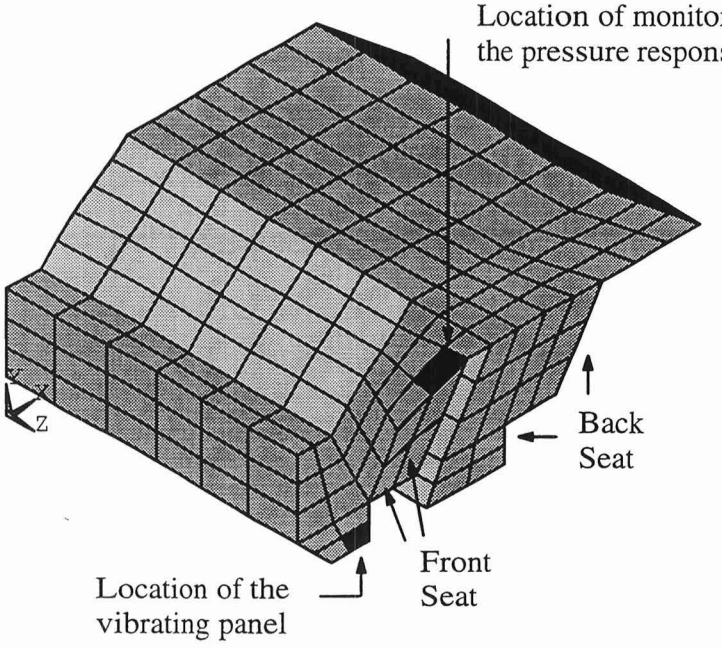

(a) Perspective View

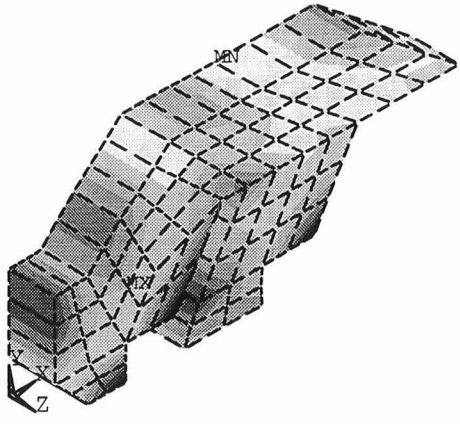

(b) Pressure Plot on
Passenger Side

Figure 27

REPORT DOCUMENTATION PAGE

Form Approved
OMB No. 0704-0188

1. AGENCY USE ONLY *(Leave blank)*	2. REPORT DATE	3. REPORT TYPE AND DATES COVERED
	August 1995	Conference Publication

4. TITLE AND SUBTITLE
Computational Modeling of Tires

5. FUNDING NUMBERS
505-63-50-19

6. AUTHOR(S)
Ahmed K. Noor and John A. Tanner

7. PERFORMING ORGANIZATION NAME(S) AND ADDRESS(ES)
NASA Langley Research Center
Hampton, VA 23681-0001
University of Virginia Center for Computational Structures Technology
Hampton, VA 23681-0001

8. PERFORMING ORGANIZATION REPORT NUMBER
L-17525

9. SPONSORING/MONITORING AGENCY NAME(S) AND ADDRESS(ES)
National Aeronautics and Space Administration
Washington, DC 20546-0001

10. SPONSORING/MONITORING AGENCY REPORT NUMBER
NASA CP-3306

11. SUPPLEMENTARY NOTES
Proceedings of a workshop sponsored by the National Aeronautics and Space Administration and the University of Virginia Center for Computational Structures Technology, Hampton, VA, and held in Hampton, Oct. 26–27, 1994

12a. DISTRIBUTION/AVAILABILITY STATEMENT
Unclassified–Unlimited

Subject Category 39

12b. DISTRIBUTION CODE

13. ABSTRACT *(Maximum 200 words)*
This document contains presentations and discussions from the joint UVA/NASA Workshop on Computational Modeling of Tires held at the Virginia Consortium of Engineering and Science Universities in Hampton, Virginia, October 26–27, 1994. The workshop attendees represented NASA, the Army and Air Force, tire companies, commercial software developers, and academia. The workshop objectives were to assess the state of technology in the computational modeling of tires and to provide guidelines for future research.

14. SUBJECT TERMS
Computational methods; Software systems; Modeling of tire response and failure; Tire mechanics and dynamics; Reduction methods

15. NUMBER OF PAGES
187

16. PRICE CODE
A09

17. SECURITY CLASSIFICATION OF REPORT	18. SECURITY CLASSIFICATION OF THIS PAGE	19. SECURITY CLASSIFICATION OF ABSTRACT	20. LIMITATION OF ABSTRACT
Unclassified	Unclassified		